DISS. ETH NO. 23096

ELECTRICAL IMPEDANCE SPECTROSCOPY OF SUSPENDED CELLS AND MICROTISSUE SPHEROIDS

A thesis submitted to attain the degree of

DOCTOR OF SCIENCES of ETH ZURICH

(Dr. sc. ETH Zurich)

presented by

Sebastian Christopher Bürgel

M.Sc. Biomedical Engineering, ETH Zurich

B.Sc. Information Technology and Electrical Engineering, ETH Zurich

born on 18.09.1984

citizen of

Germany

accepted on the recommendation of

Prof. Dr. Andreas Hierlemann

Prof. Dr. Petra Dittrich

Dr. Olivier Frey

2015

TABLE OF CONTENTS

ABSTRACT

Electrical impedance analysis of cells and tissues yielded invaluable biological insights for over one century. Initially, impedance analysis was enabling discoveries, such as the estimation of the mammalian cell membrane thickness or cytosol conductivity, that were not possible by other means. Nowadays, impedance measurements provide complementary data to optical assessments and impedance readout can be readily integrated in micro- and microfluidic systems.

This thesis describes the development of microfluidic tools with integrated impedance readout. Suspended single cells and multicellular tissue spheroids, which were flowing over a set of electrodes, were characterized by using multi-frequency electrical impedance spectroscopy (EIS).

A microfluidic chip featuring facing electrodes at the top and bottom of a microchannel was used for combined electroporation and EIS analysis. Single mammalian cells were shuttled back-and-forth over the EIS electrodes for multiple-time-point analysis of the same cell. The shuttling was facilitated in a setup featuring precise flow control,

and a bubble-free liquid flow in a microchip. Electroporation was induced via a separate electrode-pair during cell passage. The impedance data obtained from a cell before and after electroporation were fitted to a double-shelled sphere model. Dielectric properties, which were obtained in this way, suggested swelling of the cell as well as exchange of inter- and extracellular liquids. These results were confirmed by bright-field and fluorescence microscopy, which was performed in parallel and on the same cell. The device was fabricated as a glass-SU-8-glass sandwich with microelectrodes patterned onto the top and bottom glass substrate . The same microfabrication approach was also used for EIS studies of mammalian cells, yeast and bacteria.

Since traditional microfluidic electroporation methods require specific hardware and custom electrical interfaces, a simplified electroporation method was studied. A handheld corona discharge device was used to induce an electric field in a microchannel. The field was strong enough to irreversibly porate or lyse the cells. Successful lysis was evidenced by bright-field and fluorescence microscopy and was shown to happen within sub-second timescales. Cells located on top or in the direct vicinity of microelectrodes could be selectively lysed. For high-throughput lysis an even easier poration mechanism was devised: The electric field was coupled from the corona discharge directly into the microfluidic channel via a simple inlet or outlet port. In that case, the setup comprised the handheld corona device and a PDMS channel bonded onto a glass substrate.

Apart from single cells, EIS was also used to assess multicellular tissue spheroids. Spheroids are of increasing interest as a model system, which more closely resembles *in vivo* conditions than traditional 2D cell cultures grown on solid substrates. An automated multiplexed electrical impedance spectroscopy (AMEIS) system was developed for spheroid analysis. It featured 15 separate chambers hosting one spheroid each. Upon tilting the platform back-and-forth,

the spheroids were moving over sets of electrodes for EIS readout. The tilting-induced perfusion enabled device operation without pumps or tubing and allowed for convenient access via conventional pipetting. Cancer spheroids of several hundred micron diameter were injected into the chambers and continuously monitored by EIS over four days. Due to partial evaporation, the conductivity of the medium in the channel was increasing over time. Therefore, a normalization method was developed and characterized, which compensates for differences in medium conductivity and was only sensitive to the impedance of the spheroid. This was possible, since the medium and spheroid impedances could be analyzed separately as the spheroids moved over the electrodes. The results also showed that immobilized spheroids cannot be assessed by a single set of EIS electrodes over extended periods of time.

Spheroids cultured in different concentrations of the drug 5-Fluorouracil (5-FU) revealed a dose-dependent growth curve as well as differences in the onset of drug effects when assessed via impedance. These EIS results were confirmed by size measurements via microscopy at selected time points and end point ATP assay.

Initial results of an impedance-based analysis of cancer microtissue growth suggest that EIS could be a useful tool for assessing anti-cancer drug efficacy. A next step towards an integrated multi-organoid device would include a cardiac spheroid to assess cardiotoxicity in parallel. Therefore, the extraction of cardiac spheroid beating rates was assessed via impedance. It was shown that it is possible to track the cardiac beating rate over several hours in an automated fashion. A scaled-up 96-well-plate-compatible version of the AMEIS platform will increase the number of spheroids, which can be assessed in parallel. It will allow for measuring IC_{50} values and for fluidically interconnecting multi-organoid systems. Moreover, the platform will feature impedance readout for toxicity assays.

ZUSAMMENFASSUNG

Durch elektrische Impedanzanalyse von Zellen und Geweben ist seit über einem Jahrhundert weitreichender biologischer Erkenntnisgewinn ermöglicht worden. Anfänglich erbrachte die Impedanzanalyse Einsichten, die noch mit keiner anderen Technologie möglich waren, wie zum Beispiel die Bestimmung der Dicke von Säugerzellmembranen. Heutzutage werden Impedanzmethoden komplementär zu optischen Methoden genutzt, sie können in Mikro- und mikrofluidische Systeme integriert werden.

Diese Dissertation behandelt die Entwicklung mikrofluidischer Impedanzchips. Suspensionen einzelner Zellen oder multizellulärer Sphäroide, die über Elektroden flossen, wurden durch elektrische Impedanzspektroskopie (EIS) auf mehreren Frequenzen charakterisiert.

In einem Mikrofluidik-Chip mit gegenüberliegenden Elektroden oben und unten im Mikrokanal wurde Elektroporation mit Impedanzspektroskopie kombiniert. Einzelne Säugerzellen wurden für die Messung an mehreren Zeitpunkten über die Elektroden hin und her bewegt. Dies wurde durch präzise Kontrolle eines blasenfreien Flusses in Kapillaren und Mikrochips erreicht. Die Elektroporation wurde mit einem separaten Elektrodenpaar und während eines einzigen Zelldurchgangs erreicht. Die

Impedanzdaten, die vor und nach Elektroporation von einer Zelle aufgenommen wurden, wurden dann an ein sphärisches Doppelhüllenmodell gefittet. Die auf diesem Wege gewonnenen dielektrischen Eigenschaften zeigen ein Anschwellen der Zelle und einen Austausch von zellinternen und -externen Flüssigkeiten. Diese Ergebnisse wurden durch Auflicht- und Fluoreszenzmikroskopie parallel an derselben Zelle bestätigt. Der Mikrochip wurde in Glass-SU-8-Glass Sandwichbauweise mit Mikroelektroden auf den oberen und unteren Glasssubstraten gefertigt. Die gleiche Mikrofabrikationsmethode wurde auch für andere EIS Studien an Säugerzellen, Hefezellen und Bakterien verwendet.

Da gewöhnliche mikrofluidische Zellelektroporation erhebliche Anforderungen an Hardware und spezielle Anschlusstechnik stellt, wurde eine alternative Elektroporationsmethode evaluiert. Ein mobiles Koronaentladungsgerät wurde zur Einkopplung des elektrischen Feldes in den Mikrokanal genutzt. Das Feld war stark genug, um die Zellen irreversibel zu porieren oder zu lysieren. Erfolgreiche Lysis wurde durch Auflicht- und Fluoreszenzmikroskopie bestätigt. Es wurde gezeigt, dass die Lyse innerhalb einer Sekunde erfolgte. Zellen, die sich auf oder in unmittelbarer Umgebung der Elektrode befanden, konnten selektiv lysiert werden. Für Lysis mit hohem Zelldurchsatz wurde ein noch einfacherer Porationsmechanismus entwickelt: Das elektrische Feld wurde über einen Ein- oder Auslass direkt von der Koronaentladung in die Flüssigkeit eingekoppelt. In diesem Fall bestand das Setup aus einem mobilen Koronaentladungsgerät und einem PDMS-Kanal, der auf ein Glassubstrat aufgebracht wurde.

Neben Einzelzellen wurde EIS auch zur Analyse multizellulärer Sphäroide benutzt. Sphäroide sind als Modelsystem von wachsendem Interesse, da sie *in vivo*-Bedingungen realistischer abbilden, als traditionelle 2D Zellkulturen, die auf Oberflächen kultiviert werden. Ein automatisiertes, multiplexendes elektrisches Impedanzspektroskopiesystem (AMEIS) wurde zur Sphäroidanalyse

entworfen. Das System umfasste 15 Kammern, die jeweils ein Sphäroid enthielten. Durch Vor- und Zurückkippen der Plattform bewegten sich die Sphäroide über je ein Elektrodenpaar. Diese Kippvorrichtung ermöglichte Medienperfusion ohne Pumpen und Schläuche und erlaubte einen einfachen Zugang mit gewöhnlichen Pipetten. Krebssphäroide von mehreren hundert Mikrometern Durchmesser wurden so in die Kammern geladen und über einen Zeitraum von vier Tagen kontinuierlich mit EIS überwacht. Aufgrund von Verdunstung nahm die Leitfähigkeit des Mediums innerhalb der Kammern kontinuierlich zu. Daher wurde eine Normalisierungsmethode entwickelt und charakterisiert, welche die Änderung der Medienleitfähigkeit kompensierte und nur die Impedanz des Sphäroids erfasste. Dies war möglich, da die Impedanz des Mediums und der Sphäroide unabhängig voneinander bestimmt werden konnte, während sich das Sphäroid über die Elektroden bewegte. Das Verfahren zeigte auch, dass immobilisierte Sphäroide nicht mit einem einzigen Elektrodenpaar über längere Zeitspannen per EIS analysiert werden können.

Impedanzmessungen von Sphäroiden, die in verschiedenen Konzentrationen des Wirkstoffs 5-Fluorouracil (5-FU) kultiviert wurden, zeigten eine konzentrationsabhängige Wachstumskurve und Wirkungseintritt von 5-FU. Diese EIS Ergebnisse wurden an ausgewählten Zeitpunkten durch Grössenmessungen mit dem Mikroskop und eine finale ATP Messung bestätigt.

Die ersten impedanzbasierten Messungen von Krebswachstum in Mikrogeweben legen nahe, dass EIS eine nützliche Methode für Wirksamkeitsstudien von Antikrebsmitteln sein kann. Ein nächster Schritt in Richtung eines Multi-Organoidsystems würde Herz-Sphäroide zur parallelen Untersuchung von Kardiotoxizität umfassen. Daher wurden die Schlagraten von Herz-Sphäroiden per Impedanz analysiert, und es konnte gezeigt werden, dass die Schlagraten über mehrere Stunden automatisch bestimmt werden können. Eine nächstgrössere AMEIS Plattform im Format einer 96er

Mikrotiterplatte wird den Durchsatz der parallel zu analysierenden Sphäroide erhöhen. Dieses System wird die Messung von IC_{50} Werten und die Realisierung von Multi-Organoidsystemen zur impedanzbasierten Toxizitätsanalyse ermöglichen.

AUTHOR CONTRIBUTIONS

Thomas Braun:

- chapter 3: feedback, advice and planning of the corona lysis experiments

Sebastian C. Bürgel:

- chapter 2: carried out the microfabrication, planned and performed impedance measurements, data analysis and wrote the manuscript
- chapter 3: contributed to microfabrication, corona lysis experiments and manuscript writing, performed the corona lysis experiments without electrodes
- chapter 4: carried out the microfabrication, wrote all AMEIS software, planned and performed impedance measurements, data analysis and wrote the manuscript,
- chapter 5: planned the 96-well EIS platform, carried out the cardiac spheroid experiments and data analysis

Laurin Diener:

- chapter 4: performed cell culturing, spheroid handling and final cancer-spheroid EIS experiments
- chapter 5: designed the 96-well EIS platform,

Carlos Escobedo:

- chapter 2: provided feedback and help outlining the lysis experiments
- chapter 3: planned and performed first set of corona lysis experiments, data analysis and wrote the manuscript

Olivier Frey:

- provided guidance, feedback and ideas throughout this thesis
- chapter 4: helped with planning and revising
- chapter 5: helped with planning and revising

Niels Haandbæk:

- provided help with impedance questions, data analysis and modeling throughout this thesis
- chapter 2: provided feedback

Andreas Hierlemann:

- responsible for planning the overall research activities, funding, ideas and critically reviewed all sections of this thesis and corresponding manuscripts

Simon Kemmerling:

- chapter 2: helped with cell culturing and experiments for the corona lysis experiments

Jin-Young Kim:

- chapter 4: helped with cell culturing and all work involving spheroids

Nora Sauter:

- chapter 2: helped with cell culturing and experiments for the corona lysis experiments

Alexander Stettler:

- troubleshooting and help with all microfabrication issues throughout this thesis, devised the fabrication protocol for embedding the microelectrodes, performed dicing of chips.

1 INTRODUCTION

1.1 Impedance analysis of cells

Electrical and dielectrical properties of cells have been studied for over a century to gain fundamental insights into by then unknown cellular properties.[1] In the 1910s, Höber performed a series of experiments to investigate the internal conductivity of erythrocytes. A modified Wheatstone bridge was used to compare the capacitance of a cell suspension with that of a reference solution. In this way, the lower limit of the intercellular conductivity was found to be comparable to that of a 0.1 M KCl solution (0.12 S/m), possibly a lot higher.[2] A refined method involving an LC resonator circuit was used to more precisely measure the cell internal conductivity as equivalent to that of a 0.1-0.4% NaCl solution (0.2 – 0.75 S/m). This conductivity range agrees well with typical values estimated by modern methods (cf. reference 1 and chapter 2).

In the 1920s, Fricke refined the analytical models and experimental methods to analyze properties of suspended erythrocytes. Fricke's

work aimed at assessing the cell membrane permeability without interfering with the cell by measuring properties of the cell suspension. He introduced a simple circuit model of the cell depicted in Figure 1.1, which accounts for intra- and extracellular conductivities, as well as membrane capacitance. His methods of analyzing the cellular impedance allowed for an extraction of the membrane capacitance. This method provided the first estimate of the thickness of the membrane, about 3.3 nm, which is fairly close to the currently established value of 4 nm.[3]

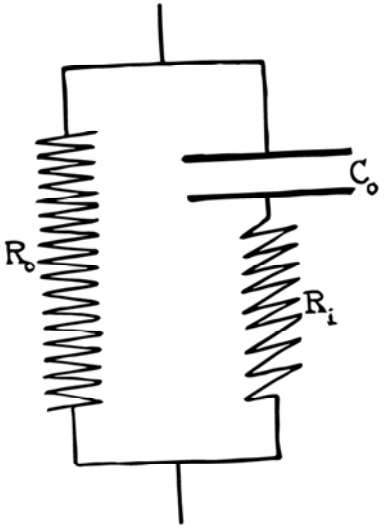

Figure 1.1. Equivalent circuit model of a cell as established by Fricke in reference 3. The extracellular resistance R_o is arranged in parallel to the membrane capacitance C_o and intracellular resistance R_i.

Analytical assessments of the cellular impedance, deduced by modeling the cell as a single-shell sphere were conducted by Cole for the first time in 1928[4] Although the approaches were fundamentally different, Cole's analytical model agreed well with the equivalent circuit models by Fricke over the studied frequency ranges. Cole's analytical model was also the basis for more

generalized models using multi-shell ellipsoids developed by Asami since 1980.[5,6] The multi-shell ellipsoid model shown in Figure 1.2 was originally developed to describe the cell walls found in *E. coli*[6] and yeast[7], but can also be used to model the nucleus of a mammalian cell (cf. chapter 2).

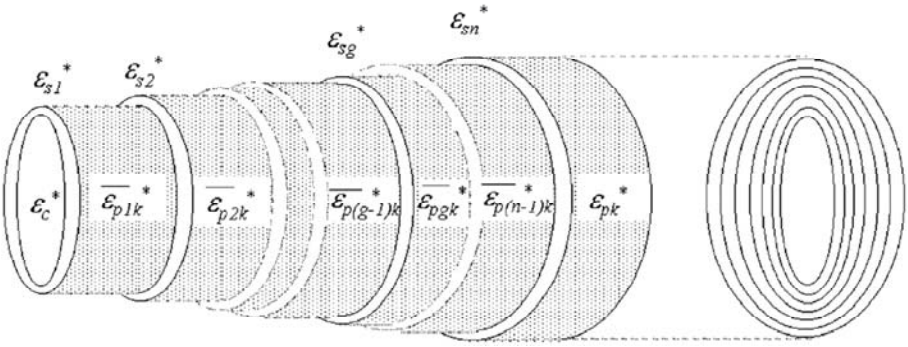

Figure 1.2. Generalized impedance model of a multi-shell ellipsoid (from reference 5).

Coulter used differences in dielectric properties of cells compared to their surrounding medium to devise an impedance-based automated cell counting device.[8] The device, schematically shown in Figure 1.3, was commercialized as the 'Coulter counter' and relied on measuring a DC-impedance across an orifice. Whenever a cell was passing that orifice (marked 'A' in Figure 1.3), the orifice impedance increased. Thus, analyzing the resulting peaks in an impedance-time plot allowed for precise high-throughput counting of single suspended cells. While earlier devices were capable of analyzing dielectric properties of bulk cell suspensions, the Coulter counter was the first single-cell impedance measurement device. Multi-frequency electrical impedance spectroscopy (EIS) of single-cells would, however, only become available decades later after the development of microelectrodes and microfluidics.

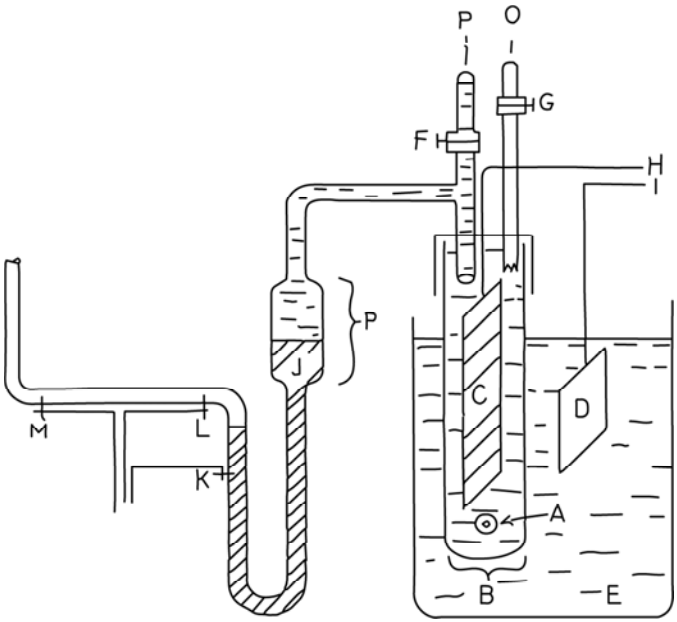

Figure 1.3. Schematic overview of the Coulter counter. A: orifice; B: test tube with orifice; C: electrode in test tube; D: electrode outside test tube; E: cell suspension; F,G: stop cock; H,I: electrode leads to amplifier and power supply; J: mercury column and reservoir R; K,L,M: electrodes to activate and stop counter (from reference 9).

1.2 Microfluidics

The field of handling small amounts of liquids at sub-millimeter length scales is termed 'microfluidics' and has enabled integrated micro total analysis sytems (μTAS) or lab on a chip (LoC) devices.[10] Although integrated micropumps implanted in animals and humans[11], multi-frequency single-cell impedance cytometers[12] and microdevices with integrated valve and sensing unit[13] were published already in the 1970s, it took two more decades until microfluidics became widely used. Initial efforts of miniaturizing chemical analysis systems were fueled by enhancements of their analytical performance: Faster and more efficient separation along

with reduced reagent volume and possibilities for integration and parallelization were motivators for Manz's concept of a μTAS.[14] The first microfluidic LoC was an electrophoresis chip also developed by Manz.[15] Microchannels were etched using conventional silicon micromachining techniques and sealed by bonding the silicon substrate to a glass slide. This packaging allowed for optical readout of, e.g., separated fluorescent dyes.[15]

In the mid 1990s, the device fabrication was significantly simplified so that rapid prototyping of microfluidic devices without complex silicon micromachining methods became possible: The Whitesides group pioneered several polydimethylsiloxane (PDMS) molding techniques, which were collectively termed 'soft lithography' methods.[16] Soft lithography methods rely on casting a flexible PDMS piece from a master mold. The most commonly used technique is replica molding in which liquid PDMS is poured onto a master mold, cured by baking and peeled off as shown in Figure 1.4.[17] The resulting PDMS piece is microstructured on the bottom side with microchannels and chambers and can then, after oxygen plasma activation, be bonded to a glass slide to seal microfluidic cavities. The parallel development of the negative-tone photoresist SU-8[18] allowed for convenient patterning of the soft lithography master substrate at high aspect ratios and tunable thicknesses.[19]

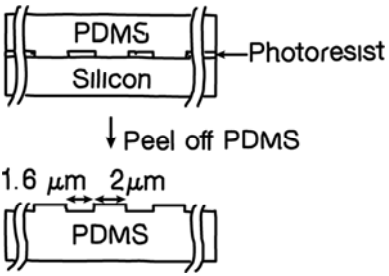

Figure 1.4. Replica molding of a flexible PDMS structure from a rigid silicon master patterned by photoresist (from reference 17).

Microfluidic devices allowed for microscale-specific physical phenomena being used in biomedical applications. These phenomena include non-turbulent laminar flows, leveraging of surface tension for formation of monodisperse droplets, or strong capillary forces driving paper microfluidic devices, which are typically employed in pregnancy tests or portable glucometers.[20] Single-cell analysis was particularly advanced by the advent of microfluidics, as microfluidics enabled culturing, assessment and manipulation of heterogenous cellular populations with single-cell resolution at high throughput.[21,22] Despite the mentioned advances, microfluidics can be considered as a technology past its hype-phase for which a single convincing 'killer application' remains yet to be found and multidisciplinary interest in microfluidics seems to be decreasing.[20,23]

1.3 Microfluidic impedance devices

The advent of microfluidics in the 1990s paved the way for the miniaturization of impedance setups. The first microfluidic Coulter counter relied on silicon micromachining and featured microfluidic channels in a silicon substrate sealed with a glass slide on top.[24] It employed a low-conductivity sheath flow, which prevents clogging of the sensitive orifice without decreasing sensitivity, as the orifice features a physically large diameter.

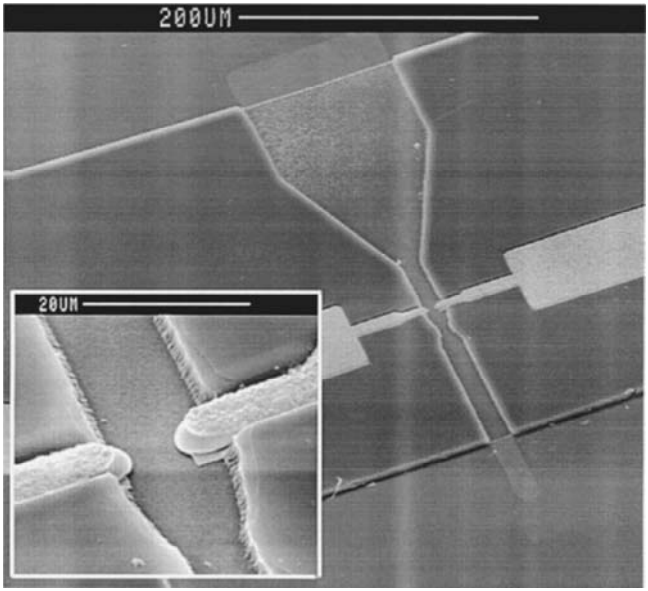

Figure 1.5. The first microfluidic single-cell impedance spectroscope with a central microfluidic channel and gold microelectrodes on the sides of the channel (from reference 25).

Ayliffe recorded multi-frequency impedance spectra of single cells for the first time in 1999.[25] The chip featured a microfluidic channel made from silicon, sealed with a glass slide; gold electrodes interfaced with the channel on both sides as shown in Figure 1.5. This device allowed for differentiation of media as well as for separation of erythrocytes and leukocytes that were flowing between the microelectrodes. A later device developed by Sohn could be used to differentiate more cell types, such as yeast, various erythrocytes, leukocytes, and fibroblasts.[26] This was the first impedance analyzer fabricated by soft-lithography. Later devices, such as the ones developed in the Morgan (cf. Figure 1.6) and Renaud groups increased the accuracy and throughput so that different populations of single cells could be separated. These devices constituted milestones towards the development of an

impedance cytometer.[27] The development of a impedance based cytometer was fueled by the limitations of fluorescence-based cytometry in the number of parameters, which can be assessed in parallel by optical means. Impedance was envisioned to complement the readouts of fluorescent labels by giving access to complementary cellular parameters in a label-free fashion. The EIS cytometer relied on a differential impedance measurement via two facing electrode sets at the top and bottom of the microchannel as shown in Figure 1.6. A facing electrode configuration produced a more uniform electric field than a coplanar arrangement located just at the bottom of the microchannel. Thus, an impedance measurement in a coplanar configuration showed more variations due to the dependence on the height of the particle moving within the channel than a corresponding facing electrode configuration. A differential readout was implemented by subtracting the impedance signal from one electrode set from that of the other set. The more stable measurements of a facing electrode setup came with additional fabrication complexity, because the fabrication of electrodes at the top of the channel was not compatible with using simple PDMS soft lithography methods. Instead, fabrication of facing electrodes typically relies on thin layers of polyimide or SU-8 that define the channel height. Another glass wafer featuring microelectrodes has then to be bonded to seal the device.[27,28] Both, drilling holes through the glass wafer as well as bonding, which requires heat and pressure, is significantly more delicate and labor-intensive than conventional PDMS-glass bonding. An alternative approach included to guide the cell suspension through a wafer-through hole that features electrode structures around the hole. While simplifying chip packaging, this non-planar approach renders optical access to the measurement site via microscopy much more complex.[29]

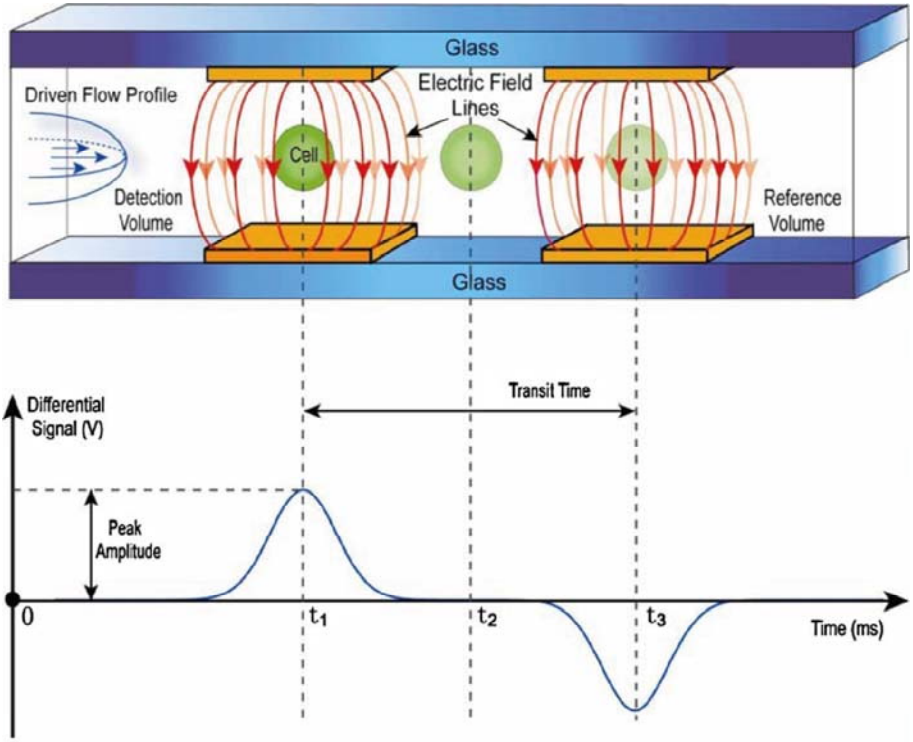

Figure 1.6. Typical setup of a microchannel for single-cell EIS recordings with a set of facing electrodes between which the impedance is measured (top). The resulting differential signal reveals a double bi-phasic peak (bottom) corresponding to the cell passing each electrode set (from reference 30).

1.4 Theory of microfluidic EIS

The early insights, such as the assessment of the cellular membrane thickness or internal conductivity, are examples of findings, which were made possible by comparing measured data to adequate models of cells. Therefore, not only devices to measure impedance of cells but also the models to interpret these data are continuously

advancing. Here, a brief overview of a simple impedance model of a cell in a microfluidic channel is given.

The ratio of the voltage *V* to the current *I* through a given system is known as the impedance *Z*. Impedance can be evaluated at multiple angular frequencies ω to gain an impedance spectrum. More generally, impedance can be treated as a complex quantity with a real part *Re(Z)* (resistance) and an imaginary component *Im(Z)* (reactance).

$$\tilde{Z}(\omega) = \frac{\tilde{V}(\omega)}{\tilde{I}(\omega)}$$

Alternatively, in polar coordinates, impedance can be described by an impedance magnitude and a phase value.

A measurement of the impedance across a microfluidic channel includes a combination of effects due to cells or particles in the channel, the medium in the channel, electrode properties and surrounding (stray) impedances. Upon being able to extract the impedance contribution of a cell between the electrodes, some of the cellular properties, such as membrane and internal specific conductivity and dielectric constant, can be inferred. This parameter extraction requires a suitable model, which can be fitted to the measured impedance spectra.

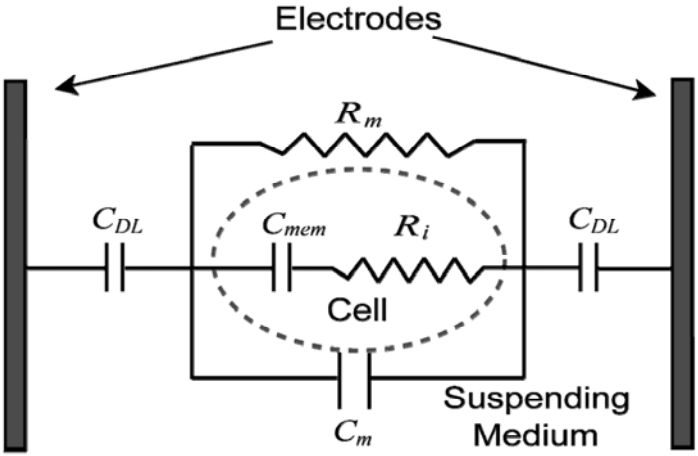

Figure 1.7. A simple equivalent-circuit model (ECM) of a cell, modeled as a single shell with the membrane capacitor C_{mem} and internal resistor R_i. The surrounding medium is accounted for by the resistor R_m and a capacitor C_m. The electric double layer at both electrode-liquid interfaces is modeled by the capacities C_{DL} (from reference 1).

A simple equivalent-circuit model, shown in Figure 1.7, is based on the model established by Fricke (cf. Figure 1.1) with additional circuit elements accounting for the dielectric properties of the surrounding medium. It also accounts for the electric double layer at the electrode-liquid interface in the microfluidic channel by a capacitor. A purely capacitive behavior of the double layer often cannot be considered a realistic scenario: Inhomogeneities and surface roughness lead to deviations, which are best accounted for by a constant-phase element (CPE), which has an impedance of[31]

$$Z_{CPE}(\omega) = \frac{1}{\sigma \cdot (j \cdot \omega)^{\alpha}}$$

with the empirically estimated CPE coefficients σ and α. The parameter α is chosen between 0 (purely resistive behavior of the CPE) and 1 (purely capacitive behavior of the CPE). For microelectrodes in a microfluidic channel, common values for α

range between 0.9 and 1, which reflects the prevailingly capacitive behavior of the double layer. Electric double layer and stray capacitance lead to deviations from the simple circuit model by Fricke shown in Figure 1.1 at low and high frequencies. The electric double layer limits impedance recordings of suspended cells and particles in a microfluidic channel at low-frequencies, because the applied electric field drops almost entirely over the double layer and does not reach the sample. (cf. Figure 1.8). A stray impedance is often primarily capacitive and arranged in parallel to the anticipated impedance across the microchannel.[32] Therefore, at high frequencies, the measured impedance will significantly decrease, as the stray capacitance increasingly assumes resistor characteristics. The limitations of the stray impedance at high frequencies can be partly overcome by closely integrating the microfluidic chip and readout electronics.

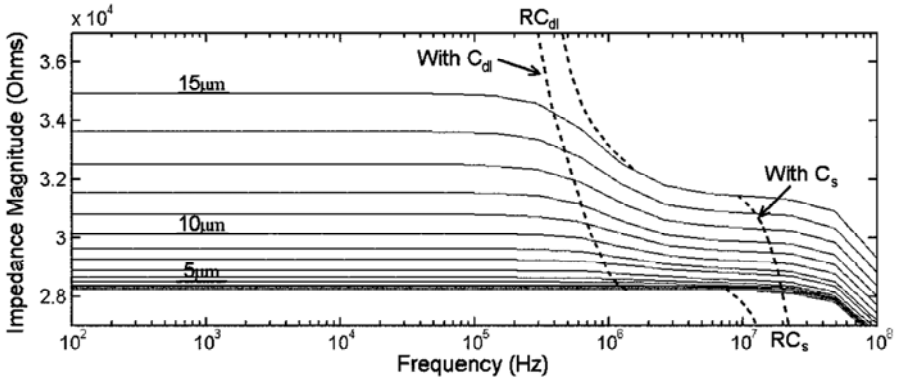

Figure 1.8. Effects of the double layer capacitance C_{dl} and stray capacitance C_s on impedance spectra of a microfluidic channel containing cells of different diameters (5 µm - 15 µm). The impedance has been obtained by a finite-element model (FEM) with facing electrodes of 20 x 20 µm^2 surface area and a channel height of 100 µm (from reference 32).

The simple circuit model of a cell comprising a serial membrane capacitor and internal resistor highlighted in Figure 1.7 can be

replaced by a more complex multi-shell model shown in Figure 1.2 to increase accuracy. An alternative approach is to estimate the impedance numerically by a finite-element model.[32] Such a model can yield impedance spectra, such as the one shown in Figure 1.8, for different cell sizes.

In an analytical assessment, the total impedance of a suspended cell between microelectrodes is typically treated as a mixture of cell and medium. This mixture has the complex impedance:[1]

$$\tilde{Z}_{mix}(\omega) = \frac{1}{j \cdot \omega \cdot \tilde{\varepsilon}_{mix}(\omega) \cdot G_f}$$

and depends on the geometric factor G_f and the complex permittivity of the mixture

$$\tilde{\varepsilon}_{mix}(\omega) = \tilde{\varepsilon}_m(\omega) \frac{1 + 2 \cdot \Phi \cdot \tilde{\mathrm{f}}_{CM}(\omega)}{1 - \Phi \cdot \tilde{\mathrm{f}}_{CM}(\omega)}$$

which, in turn, depends on the volume fraction Φ of the particle (cell) and the Clausius-Mossotti factor:

$$\tilde{\mathrm{f}}_{CM}(\omega) = \frac{\tilde{\varepsilon}_p(\omega) - \tilde{\varepsilon}_m(\omega)}{\tilde{\varepsilon}_p(\omega) + 2 \cdot \tilde{\varepsilon}_m(\omega)}$$

The complex permittivity

$$\tilde{\varepsilon}(\omega) = \varepsilon - \frac{j \cdot \sigma}{\omega}$$

depends on the resistivity and the dielectric constant, the index *m* denotes the properties of the surrounding medium and *p* denotes the particle (cell) properties. In the simplest case of a cell modeled as a single shell sphere, the complex permittivity of the particle is:

$$\tilde{\varepsilon}_p(\omega) = \tilde{\varepsilon}_{mem}(\omega) \frac{\gamma^3 + 2 \cdot \left(\frac{\tilde{\varepsilon}_i(\omega) - \tilde{\varepsilon}_{mem}(\omega)}{\tilde{\varepsilon}_i(\omega) + 2 \cdot \tilde{\varepsilon}_{mem}(\omega)} \right)}{\gamma^3 - \left(\frac{\tilde{\varepsilon}_i(\omega) - \tilde{\varepsilon}_{mem}(\omega)}{\tilde{\varepsilon}_i(\omega) + 2 \cdot \tilde{\varepsilon}_{mem}(\omega)} \right)}$$

with

$$\gamma = \frac{R + d}{R}$$

for a cell of radius *R* and membrane thickness *d*, the indices *i* are referring to the cell's internal properties and *mem* to the membrane properties.[1] This derivation of the impedance allows for extraction of circuit elements, pictured in Figure 1.7, as well as for fitting of the modeled impedance spectrum to measured impedance data in order to extract characteristic properties of a cell. The impedance model also gives an overview of which elements contribute to the impedance spectrum at the frequency ranges shown in Figure 1.9: The double layer limits the magnitude below 400 kHz, the cell size dominates at frequencies around 1 MHz while cell membrane and cytoplasm start influencing the spectra around 3 MHz and 20 MHz, respectively.

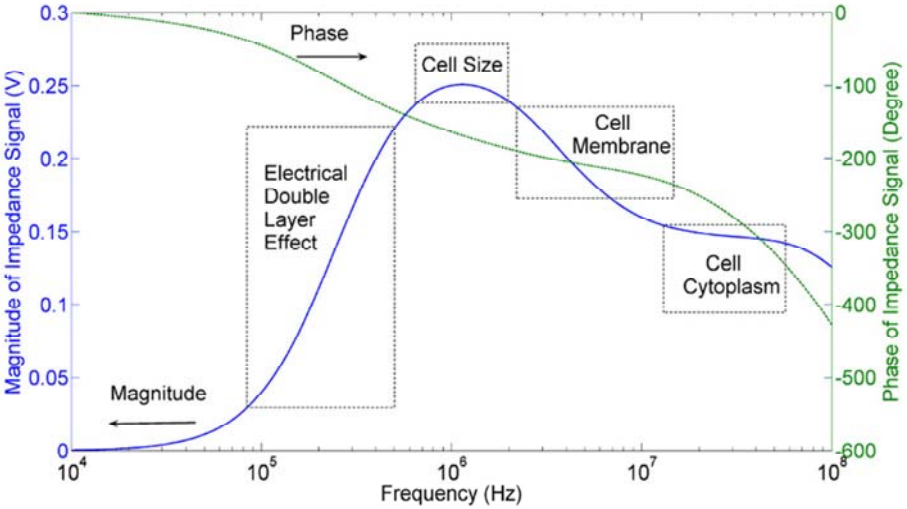

Figure 1.9. A simulated differential impedance magnitude and phase spectrum for a 6-µm-diameter cell showing the frequency ranges influenced primarily by the electrical double layer, cell size, membrane or cytoplasm (from reference 1).

1.5 Microtissue spheroids

Three-dimensional (3D) cell cultures are emerging as an alternative to traditional two-dimensional (2D) cultures. This change in cell culture paradigm is motivated by the limitations of 2D cell cultures grown on plastic substrates; flat cell cultures cannot sufficiently mimic the cell-cell or cell-extracellular matrix interactions present in *in vivo* systems, and the cells often lose fundamental properties when taken out of their natural environment.[33,34] Moving towards 3D cell cultures led to a range of insights that would not have been possible in traditional 2D cultures. These findings included the reversion of malignant cancer cells to healthy tissue[35] and drug-induced transition of metastatic cancer cells to very mobile amoeba-like shapes.[36] Moreover, hepatocytes were found to feature significantly enhanced viability and functionality in 3D compared to standard 2D cell cultures.[37] The combination of 3D organotypic micro-tissues and microfluidic devices is giving rise to novel *in vitro* methods for drug screening and toxicology assays. These methods constitute an alternative to animal experiments and feature a closer resemblance to *in vivo* conditions as compared to traditional 2D cell cultures. Recent developments of organotypic microsystems include functional organ models on a chip mimicking lung[38], renal tubuli of the kidney[39], liver[40], and heart.[41]

A variety of 3D tissue constructs has been evaluated for biomedical applications in the past. Tissues have been formed by utilizing pre-formed or soluble matrices or by stacking of individually grown monolayers.[42] All of these methods require introduction of non-native material into the cellular environment or interference with the tissue, which is particularly detrimental to delicate primary or stem cells. In contrast, scaffold-free microtissue spheroids can be formed in a variety of ways:[42] (i) Suspended cells in roller or shaker bottles aggregate, but spheroid growth is sometimes affected by physical forces.[43] (ii) The use of culture ware with non-adherent surfaces

leads to irregular cell aggregates, and chemicals used for surface coatings may influence the spheroid formation.[44] (iii) The hanging-drop method limits interference of cells with external factors, which allows for culturing of even delicate cell types, such as stem cells:[45] A small drop of a cell suspension is hanging from a rigid surface, and cells aggregate at the bottom of the drop as shown in Figure 1.10.[44] The liquid-air interface provides no anchoring points for the cells to adhere to and allows for an ideal gas-exchange between medium and environment.

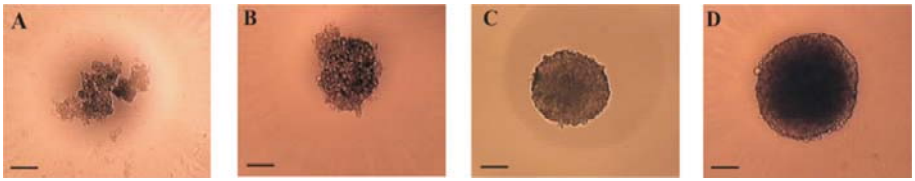

Figure 1.10. Formation and growth of a HepG2 cancer spheroid inside a hanging drop at day 1, 3, 4, 7 and 10 leads to regular round spheroids, the scale bar is 100 µm (from reference 44*).*

In parallel to the single-cell EIS chips, microdevices to assess the impedance spectra of multicellular tissue spheroids were developed.[46] Due to their large size, the diameter is on the order of hundreds of microns, spheroids are difficult to analyze optically. Especially the core of the tissue is difficult to assess, as the cellular arrangement is optically almost opaque. EIS, however, is well suited for assessments on any length scale deu to the availability of multiple frequencies and can be readily integrated and parallelized. The setup in Figure 1.11, developed in Robitzki's group, featured a capillary microdevice with a tapered center in which the spheroid is placed. Similar to the Coulter counter, the electric field is concentrated at the constriction and thus sensitively measures the properties of the tissue located at that constriction.

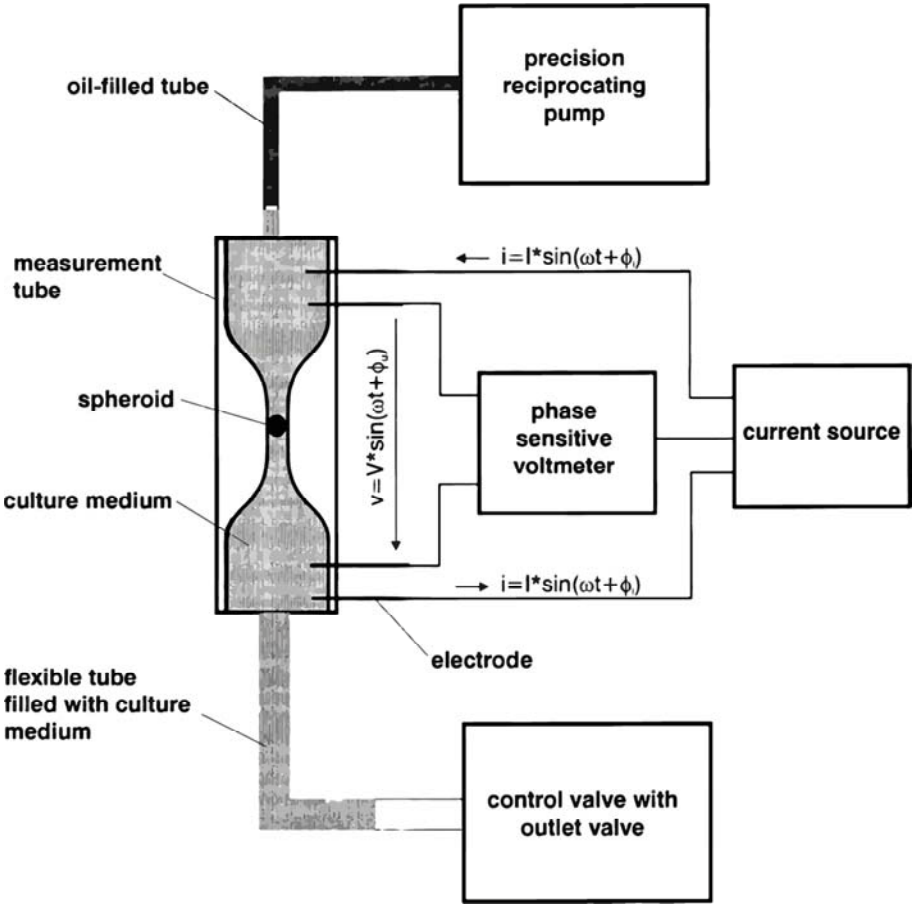

Figure 1.11. Capillary EIS device for analyzing impedance of multi-cellular spheroids (from reference 46*).*

1.6 Summary of major results

1.6.1 Microfluidic chip with facing electrodes

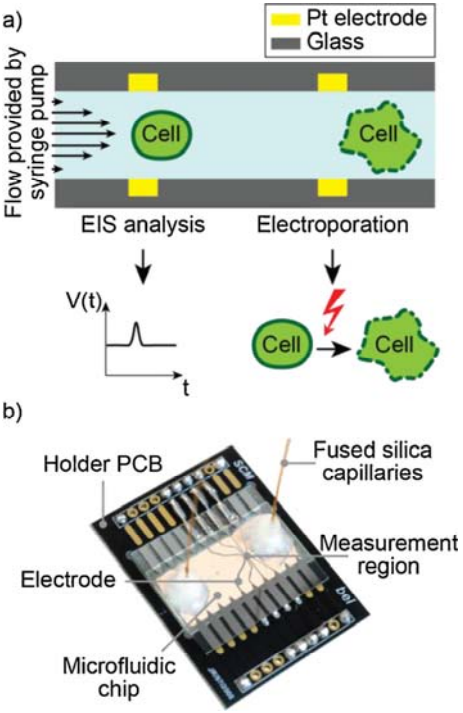

The first development towards impedance recordings and electroporation of suspended cells was the establishment of a reliable device fabrication protocol for an impedance device with facing electrodes. The microfluidic chip was a glass-SU-8-glass sandwich with integrated platinum electrodes at the top and bottom of the channel. Electrode fabrication relied on established lift-off processing with an additional first etching step to yield planar electrodes embedded in the glass substrate. 400 µm-diameter inlet holes were drilled via diamond-tip drill bits after metallization. The channel geometry was defined by varying SU-8 thicknesses between 10 µm for measurements of yeast and bacteria and 500 µm for first measurements of spheroids. Key steps included wafer-level alignment of top and bottom substrates using a standard mask-aligner without bond-aligner insert, followed by adhesive bonding and dicing.

1.6.2 EIS for *in situ* characterization of single-cell electroporation

An integrated microfluidic chip was used to characterize single cells before and after electroporation. This was achieved by shuttling the cell repeatedly back-and-forth by precise control of a syringe pump in a bubble-free microfluidic setup. The impedance spectra recorded from the very same cell both before and after electroporation were used to fit a double-shell cell model. Parameters, which were extracted from this model, suggest the swelling of the cell, as well as the exchange of intra- and extracellular liquids. The results were confirmed by fluorescence microscopy.

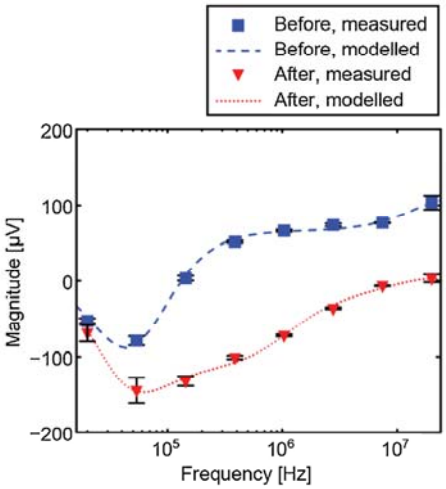

1.6.3 Cell electroporation through corona discharge

Conventional electroporation in microfluidic devices requires microstructured electrodes as well as interfacing hardware. An alternative method for porating cells via a handheld corona discharge device was characterized. The electric field was coupled into the microchannel via a corona arc, which irreversibly porated cells in a microchannel. The coupling of the electric field happened either via microelectrodes, or, in the most simple scenario, via an inlet hole filled with conductive cell culturing medium. Cells were shown to have compromised membrane integrity and were enzymatically inactive after sub-second exposure.

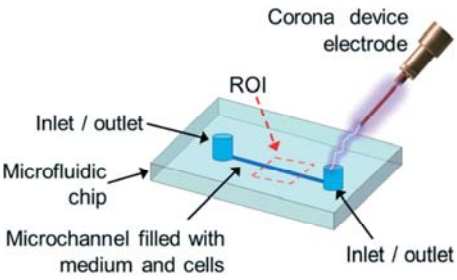

1.6.4 EIS device for monitoring microtissue spheroids

A microfluidic device for parallel EIS measurements of up to 15 cancer spheroids was devised. The EIS recordings of the separate spheroids were performed automatically and were shown to be possible over multiple days. The resulting impedance data were sensitive to the spheroid size and indicated drug-induced changes of the growth rate. The drug-dose correlations obtained by EIS measurements correlated with parallel optical assessments at selected time points, as well as with end-point ATP assays.

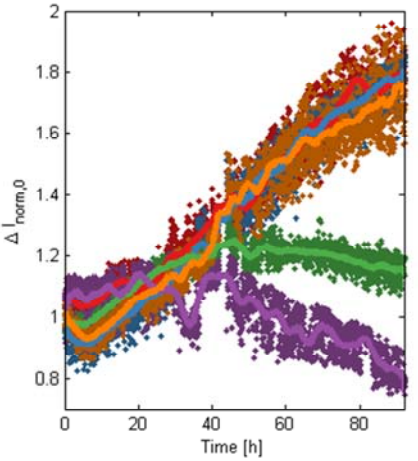

Bibliography

1 T. Sun and H. Morgan, in *Microfluidics Based Microsystems*, eds. S. Kakaç, B. Kosoy, D. Li and A. Pramuanjaroenkij, Springer Netherlands, 2010, pp. 507–527.

2 R. Höber, *Pflüger's Arch. für die gesamte Physiol. des Menschen und der Tiere*, 1910, **133**, 237–253.

3 H. Fricke and S. Morse, *J. Gen. Physiol.*, 1925, **9**, 153–67.

4 K. S. Cole, *J. Gen. Physiol.*, 1928, **12**, 29–36.

5 K. Asami, *Prog. Polym. Sci.*, 2002, **27**, 1617–1659.

6 K. Asami, T. Hanai and N. Koizumi, *Biophys. J.*, 1980, **31**, 215–28.

7 K. Asami and T. Yonezawa, *Biophys. J.*, 1996, **71**, 2192–2200.

8 W. H. Coulter, *Proc. Natl. Electron. Conf.*, 1956, **12**, 1034–

1042.

9 C. F. Mattern, F. S. Brackett and B. J. Olson, *J. Appl. Physiol.*, 1957, **10**, 56–70.

10 G. M. Whitesides, *Nature*, 2006, **442**, 368–73.

11 L. J. Thomas and S. P. Bessman, *Trans. Am. Soc. Artif. Intern. Organs*, 1975, **21**, 516–22.

12 R. A. Hoffman and W. B. Britt, *J. Histochem. Cytochem. Off. J. Histochem. Soc.*, 1979, **27**, 234–40.

13 S. C. Terry, J. H. Jerman and J. B. Angell, *IEEE Trans. Electron Devices*, 1979, **26**, 1880–1886.

14 A. Manz, N. Graber and H. M. Widmer, *Sensors Actuators B Chem.*, 1990, **1**, 244–248.

15 A. Manz, D. J. Harrison, E. M. J. Verpoorte, J. C. Fettinger, A. Paulus, H. Lüdi and H. M. Widmer, *J. Chromatogr. A*, 1992, **593**, 253–258.

16 X.-M. Zhao, Y. Xia and G. M. Whitesides, *J. Mater. Chem.*, 1997, **7**, 1069–1074.

17 Y. Xia, E. Kim, X.-M. Zhao, J. A. Rogers, M. Prentiss and G. M. Whitesides, *Science (80-.).*, 1996, **273**, 347–349.

18 K. Y. Lee, N. LaBianca, S. A. Rishton, S. Zolgharnain, J. D. Gelorme, J. Shaw and T. H.-P. Chang, *J. Vac. Sci. Technol. B Microelectron. Nanom. Struct.*, 1995, **13**, 3012.

19 D. C. Duffy, J. C. McDonald, O. J. A. Schueller and G. M. Whitesides, *Anal. Chem.*, 1998, **70**, 4974–4984.

20 E. K. Sackmann, A. L. Fulton and D. J. Beebe, *Nature*, 2014, **507**, 181–189.

21 D. Di Carlo and L. P. Lee, *Anal. Chem.*, 2006, **78**, 7918–7925.

22 M. Leslie, *Science (80-.).*, 2011, **331**, 24–6.

23 H. Becker, *Lab Chip*, 2009, **9**, 2119.

24 U. D. Larsen, G. Blankenstein and J. Branebjerg, in *Proceedings of International Solid State Sensors and*

Actuators Conference (Transducers '97), IEEE, 1997, vol. 2, pp. 1319–1322.

25 H. E. Ayliffe, A. B. Frazier and R. D. Rabbitt, *J. Microelectromechanical Syst.*, 1999, **8**, 50–57.

26 L. L. Sohn, O. A. Saleh, G. R. Facer, A. J. Beavis, R. S. Allan and D. A. Notterman, *Proc. Natl. Acad. Sci. U. S. A.*, 2000, **97**, 10687–90.

27 S. Gawad, L. Schild and P. H. Renaud, *Lab Chip*, 2001, **1**, 76–82.

28 D. Holmes, J. K. She, P. L. Roach and H. Morgan, *Lab Chip*, 2007, **7**, 1048–56.

29 H. Tang and Y. Gao, *IEEE Sens. J.*, 2005, **5**, 1346–1352.

30 T. Sun, C. Berkel, N. G. Green and H. Morgan, *Microfluid. Nanofluidics*, 2008, **6**, 179–187.

31 T. Pajkossy, *J. Electroanal. Chem.*, 1994, **364**, 111–125.

32 S. Gawad, K. Cheung, U. Seger, A. Bertsch and P. Renaud, *Lab Chip*, 2004, **4**, 241–51.

33 F. Pampaloni, E. G. Reynaud and E. H. K. Stelzer, *Nat. Rev. Mol. Cell Biol.*, 2007, **8**, 839–845.

34 A. Abbott, *Nature*, 2003, **424**, 870–2.

35 V. M. Weaver, *J. Cell Biol.*, 1997, **137**, 231–245.

36 K. Wolf, I. Mazo, H. Leung, K. Engelke, U. H. Von Andrian, E. I. Deryugina, A. Y. Strongin, E. B. Bröcker and P. Friedl, *J. Cell Biol.*, 2003, **160**, 267–277.

37 M. J. Gómez-Lechón, R. Jover, T. Donato, X. Ponsoda, C. Rodriguez, K. G. Stenzel, R. Klocke, D. Paul, I. Guillén, R. Bort and J. V. Castell, *J. Cell. Physiol.*, 1998, **177**, 553–562.

38 D. Huh, B. D. Matthews, A. Mammoto, M. Montoya-Zavala, H. Y. Hsin and D. E. Ingber, *Science (80-.).*, 2010, **328**, 1662–1668.

39 S.-S. Yun, S. Y. Yoon, M.-K. Song, S.-H. Im, S. Kim, J.-H.

Lee and S. Yang, *Lab Chip*, 2010, **10**, 1442–1446.

40 Y. Nakao, H. Kimura, Y. Sakai and T. Fujii, *Biomicrofluidics*, 2011, **5**, 022212.

41 A. Grosberg, P. W. Alford, M. L. McCain and K. K. Parker, *Lab Chip*, 2011, **11**, 4165.

42 J. M. Kelm and M. Fussenegger, *Trends Biotechnol.*, 2004, **22**, 195–202.

43 M. T. Santini, G. Rainaldi and P. L. Indo, *Int. J. Radiat. Biol.*, 1999, **75**, 787–799.

44 J. M. Kelm, N. E. Timmins, C. J. Brown, M. Fussenegger and L. K. Nielsen, *Biotechnol. Bioeng.*, 2003, **83**, 173–80.

45 G. M. Keller, *Curr. Opin. Cell Biol.*, 1995, **7**, 862–869.

46 H. Thielecke, A. Mack and A. Robitzki, *Biosens. Bioelectron.*, 2001, **16**, 261–269.

2 On-chip electroporation and impedance spectroscopy of single cells

Sebastian C. Bürgel, Carlos Escobedo, Niels Haandbæk and Andreas Hierlemann

Published in Sensors and Actuators B: Chemical

doi:10.1016/j.snb.2014.12.016

2.1 Abstract

We present an integrated microplatform for handling, electroporation and label free analysis of single mammalian cells in suspension. Accurate axial positioning of a cell flowing through a channel is accomplished through microfluidic control and flow direction reversal; electroporation is achieved by applying 2 $kVcm^{-1}$ at 50 kHz through on-chip microelectrodes; label-free detection of changes in the cell undergoing electroporation is performed by means of electric impedance spectroscopy (EIS). Shuttling the cell back and forth allows either (a) assessment of a single cell at multiple points of time to evaluate dynamic processes or (b) increased quality of EIS results by averaging subsequent passages of the same cell through the measurement region. Electrical parameters are extracted from the measurement by fitting the impedance magnitude spectrum to an equivalent-circuit model of the microchannel and by using a three-shell model for the cell. The fitting procedure is shown to be robust and suggests cell swelling, exchange of intra- and extracellular liquids, and change of the cell membrane and nuclear envelope capacitance. Cell swelling was in agreement with bright-field micrographs, while the exchange of intra- and extracellular liquids has also been observed via established fluorescent markers. The quantification of cellular changes as well as of the changes in cellular dielectric properties induced by electroporation enables a better understanding and control of the cell electroporation process.

2.2 Introduction

Many biomedical applications require introduction of external material into the cell or extraction of cellular contents across the cellular membrane. Access to intracellular contents has enabled single-cell transfection[1], cell engineering[2], particle delivery including quantum dots[3], electrofusion of cells[4], inactivation of bacteria[5], gene amplification and analysis[6] and extraction of cellular contents for

further analysis steps.[7] Opening of the cell membrane has been realized by chemical[8,9], mechanical[10,11], optical[12] and electrical means.[13] The last method, commonly referred to as electroporation or irreversible electroporation, is realized by exposing the cell to an electric field. Electroporation has several advantages, such as no contamination with chemical agents that possibly denature proteins or complicate the downstream analysis[14], high efficiency[15], applicability to a broad range of cells[16] and the ability to rapidly open the membrane to measure fast, sub-second cellular processes.[17] Electroporation by means of microdevices offers additional benefits including a reduced quantity of reagents required, further on-chip integration, *in situ* visualization and real-time monitoring of single-cell or sub-cellular-scale processes.[18]

Cell electroporation is based on exposing a cell to electric fields, which induce a trans-membrane potential (TMP) on the order of hundreds of mV to 1 V. This TMP results in the generation of membrane pores with typical diameters of ~50 nm.[19] Early single-cell electroporation microdevices utilized trapping cavities[20], while later designs featured free-flowing cells in microchannels.[21,22] More recently, carbon nanotubes have been shown to increase cell electroporation efficiency.[23] In all cases, an electrical field was demonstrated to be a suitable tool to access the intracellular contents. Characterizing cell damage upon exposure to electric fields is challenging, since dynamic nanoscale processes are happening on timescales ranging from nanoseconds to several seconds.[24] Evaluation of the efficacy of this method has relied on conventional microscopy with established fluorescent markers, such as calcein AM (cAM) and propidium iodide (PI). Calcein AM is a life-stain that is taken up and selectively marks living cells, whose active enzymes cleave the molecule into a fluorescent product. PI, on the other hand, is a dead-stain that does not permeate the membranes of living cells and only becomes fluorescent when bound to cellular RNA or DNA. Hence, it only marks cells with permanently or transiently compromised membrane integrity.[25]

Electrical impedance spectroscopy (EIS) is a label-free analysis method that has been used to probe the type, size, and dielectric properties of cells.[26,27] More recently, EIS has been demonstrated to be a suitable tool for label-free and high-throughput analysis of single-cells [28,29]. In EIS, an AC voltage is applied to a pair of electrodes, which causes a current to flow between them. The current change upon passage of a cell or particle between the electrodes is measured and then analyzed to determine the particle/cell dielectric properties. The electrodes may be arranged in either a coplanar configuration on one side of the channel or in a configuration of two facing electrodes across the channel. The latter configuration yields more homogeneous electric fields and thus is less sensitive to variations in the vertical cell position. The frequency of the applied AC voltage is typically in the range of kHz to MHz. Multiple frequencies may be applied in parallel, which allows for recording an impedance spectrum. It has been shown that the cell size contributes to the impedance response at all frequencies, that the membrane capacitance contributes predominantly at around 1 MHz, and that the cytoplasm conductivity becomes prevalent at frequencies approaching 10 MHz.[30] Impedance is inherently a complex parameter including a real and imaginary part, and therefore, impedance spectra are typically displayed as magnitude and phase signals.

In the past, measurements of electrical properties of single cells undergoing electroporation have been carried out by using different approaches. Current-voltage and current-time relationships, as well as plasmonic EIS have been used for immobilized or attached cells,[31–33] whereas flow-through EIS assessment of intact and electroporated cell populations has been used for suspended cells.[34] The benefits of using flow-through EIS for assessment of cell damage following electroporation include a straightforward fabrication and integration of the impedance-measurement function, as the microsystem inherently features electrical interfacing for carrying out the electroporation. Moreover, the method is label-free

and can be used for quantification of cellular processes. EIS can interrogate properties of the cellular membrane, as well as of internal contents of the cell. It is therefore well suited for a detailed evaluation of the cell electroporation process, which is expected to alter both the cellular membrane and the composition of the cell cytosol through an exchange of intra- and extracellular medium. To the best of our knowledge, no system has been reported yet that is capable of recording electric impedance spectra both before and after electroporation of the same single cells without the need for cell immobilization.

Here we report on a microsystem that combines single-cell electroporation and EIS for label-free single-cell analysis. The system allows for time-resolved single-cell monitoring and precise cell position control before and after electroporation under flow-through conditions. With this integrated microsystem, the conditions of intact and porated cells, as well as the dynamics of the electroporation process can be assessed. Cellular damage and alterations upon electroporation are quantified by fitting the EIS spectra with equivalent-circuit models. The system allows for simultaneous optical inspection of the cells through bright-field and fluorescence microscopy, which provide additional information on the single-cell electroporation process. In the presented platform, handling, poration and label-free analysis of single cells has been achieved within the same chip.

2.3 Materials and methods

2.3.1 Electroporation

The electric field used for electroporation of the cells in the microchip was generated by a set of facing electrodes. For poration, this set of facing electrodes was temporarily switched on during a single passage of the cell. The presence of the

porating electric field led to a minor shift of the EIS signal baselines, therefore, the evaluation of the impedance signal was done only after switching off the poration field after the first passage of the cell. The applied AC voltage of 8 V amplitude at 50 kHz was applied by using a 8116A Function Generator (Hewlett Packard, USA). In the 40-µm-high channel this voltage induces a transmembrane potential of 1.1 V (see calculations in the supplementary information) and did not lead to formation of gas bubbles around the electrodes. The typical potential that initiates formation of pores in mammalian cell membranes has been reported to be in the range of 0.1 - 1 V.[35,36] The parameters chosen here fall within this range.

2.3.2 EIS measurements

A superposition of AC signals of 1 V amplitude in the range of 20 kHz to 20 MHz was applied to an electrode at the bottom of the microchannel. The exact frequencies are listed in Supplementary Table 2.1. A matching recording electrode was patterned at the top of the channel and received current from the stimulation electrode. The recorded signal was filtered with a 100 Hz bandwidth filter in the impedance spectroscope. During EIS measurements, a passing cell altered the dielectric properties of the volume between the electrodes and, therefore, produced distinct current readings. The current was then transformed into voltages using a trans-impedance amplifier (HF2TA, Zurich Instruments AG, Switzerland) and measured by using an impedance spectroscope (HF2, Zurich Instruments AG, Switzerland). The impedance spectroscope measured magnitude and phase of the readout voltage. Signals at eight different frequencies were superimposed to measure an impedance spectrum at multiple frequencies at the same time. The polarity (minima or maxima) of the signal peaks corresponding to the passage of the cell between the

electrodes at each frequency depended on the electric properties of cell and surrounding medium. EIS signals were stored on a PC for later analysis. The recorded EIS signals were analyzed using MATLAB (The MathWorks Inc., USA). The raw data recorded at each frequency were first low-pass filtered (cut-off frequency 25 Hz), then the peaks and corresponding baseline levels were detected; the peak-to-baseline values were calculated for signal magnitude and phase. When averaging was required, mean values and standard deviations of peak-to-baseline values of five succeeding peaks were calculated.

2.3.3 Analysis of EIS signals and modeling

Extraction of electrical parameters of the microchannel and a cell between the EIS measurement electrodes was performed by fitting the measured signal magnitude values to response of the models. Two separate models were established (cf. Figure 2.4): (1) The microelectrodes with only medium in between them, and (2) the same situation with an additional cell model between the microelectrodes. Both scenarios were calculated for conditions before and after electroporation individually for each cell.

The model of the channel is depicted in Figure 2.4a. It comprises of a constant-phase element for the electric double layer at the electrode-liquid interfaces and a resistor between the electrodes accounting for the Ohmic resistance of the medium in parallel to the capacitive coupling between the electrodes. A parallel parasitic capacitance is included to account for external coupling via cables and other elements outside of the microchannel. The transfer function of the model is used to fit the theoretically calculated signal magnitude spectrum to the measured spectrum by using MATLAB.

After extracting values for the double layer capacitance, medium conductivity, and parasitic capacitance of the microchannel, parameters for the cell were obtained from the second model. The frequencies of up to 20 MHz used for EIS analysis allow for measurements sensitive to intracellular compartments such as the nucleus. Therefore, an established three-shell model of a spherical cell[37–39] depicted in Figure 2.4b was introduced into the model of the microchannel. The cell model comprises cell membrane, cytoplasm, nuclear envelope and nucleoplasm. Each of these components is characterized by its conductivity (σ), relative permittivity (ε), and thickness or radius. The collective impedance of the suspension containing the three-shelled sphere was calculated and fitted to the measured peak-to-baseline signal magnitude. All fits were carried out 100 times with randomly chosen initial guesses of parameters to evaluate the robustness of the fit. The range of the parameters for initial guesses and fitting bounds are indicated in Table 2.1. Fixed parameters are listed in Supplementary Table 2.2. The fit was discarded, if it did not converge to a solution within 10000 iterations, or if the residual was more than 10% higher than the minimal residual of all other fits.

2.3.4 Microfluidic chip fabrication

The fabrication of the microfluidic glass-SU-8-glass sandwich chip relied on adhesive bonding of SU-8 to the top glass. Platinum electrodes of 200 nm thickness were slightly recessed in the glass substrate (brief ion-beam etching step prior to metal deposition) for optimal SU-8 bonding performance. These electrodes were used in the channels for electroporation and EIS measurements. The electrode width was 18 µm with a spacing of 18 µm between the EIS electrodes and a spacing of 100 µm between EIS electrode set and neighboring poration electrode set. The channel cross-section at the

measurement site was 40x40 µm². The chips were mounted on a PCB holder enabling the chip to be affixed onto a microscope stage. Fused silica capillaries provided the fluidic interface to a 100 µl glass syringe (ILS Innovative Labor Systeme GmbH, Germany) actuated via a Nemesys syringe pump (Cetoni AG, Germany).

2.3.5 Cell preparation

HeLa cells (catalog number CCL-2) and CHO-K1 (catalog number CCL-61, both purchased from ATCC, USA) were grown in cell culture flasks until confluency in Dulbecco's Modified Eagle's Medium (DMEM) with 10% fetal bovine serum and 1% Penicillin/Streptomycin. After trypsination the cells were centrifuged, the medium discarded, and the cell pellet was re-suspended in isotonic sucrose buffer, ISB (sucrose (250 mM), HEPES (10 mM), EDTA (5 mM) adjusted to pH 7.4) with PI (40 µM) and cAM (4 µM). Other solutions, like PBS or cell medium, lead to bubble formation during electroporation. Furthermore, sugar buffers are also used for electron microscopy, which is a possible downstream analysis method for this platform. However, from theoretical considerations in the supplementary information it is evident, that higher-conductivity solutions would entail higher induced trans-membrane potentials and, thus, more efficient electroporation.

2.3.6 Imaging

The chip was mounted on the stage of an inverted fluorescence microscope (DMI-4000B, Leica Microsystems AG, Switzerland). This setup allowed for optical inspection of the cell in parallel to EIS. Images or videos were recorded with a camera (DFC 340 FX, Leica Microsystems AG, Switzerland) by means of the Leica Application Suite software (Leica Microsystems AG, Switzerland) and later analyzed by using FIJI.[40] The same imaging parameters (lamp intensity, aperture,

magnification, exposure time, gain) were used throughout the experiments.

2.3.7 Microfluidic operation

After flushing the chip with ethanol until all bubbles were removed, the chip was rinsed with de-ionized water, followed by ISB before injecting the cell suspension. The flow speed was then reduced to 0.05 µl/min, so that imaging of the cells could be carried out without motion artifacts. A custom C# program was used to trigger the flow inversion, whenever an EIS signal of a passing cell was detected. Inversion of the flow happened in intervals of a few seconds as shown in Figure 2.3a. The inversion took less than one second (see also Supplementary Video 2.1). This back-and-forth shuttling of the cell allowed for multiple EIS measurements and, thus, enabled a time-resolved assessment of the electroporation process.

2.4 Results and discussion

2.4.1 Integrated micro-platform

For electroporation, a set of facing electrodes, as schematically shown Figure 2.1a, was used to apply an 8 V amplitude electrical signal at 50 kHz during a single transit of a cell through the electroporation region. For the EIS measurements, a superposition of eight 1 V amplitude signals with frequencies ranging from 20 kHz to 20 MHz was applied via the two bottom electrodes. The current changes obtained upon passage of cells between the facing electrodes were converted into voltages in an off-chip trans-impedance amplifier and were stored for analysis. Simultaneously to the EIS measurements, conventional microscopy was carried out in order to verify the EIS results. The cells were moved through the microchannel by

means of a syringe pump with the possibility to reverse the flow direction.

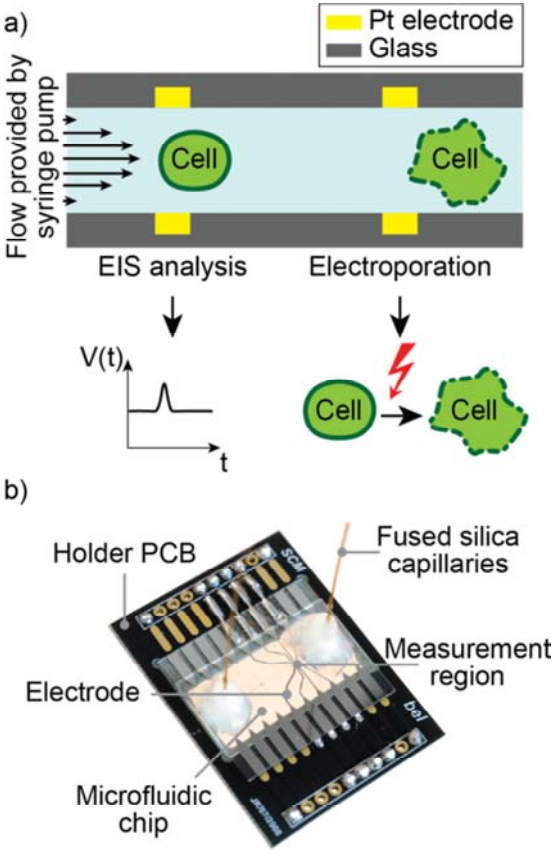

Figure 2.1. Overview of the microplatform a) Cross-sectional schematic of the measurement region in the integrated chip. A pair of electrodes was used for electroporation upon passage of a cell, and a separate set of two facing electrodes was used for EIS measurements. Upon passage of a cell, the impedance at high frequencies between the first electrode pair was decreased and the resulting output voltage was increased as displayed. The electroporation field at the other electrode set was temporarily switched on for the duration of one cell passage b) Photograph of the microfluidic chip.

In contrast to existing EIS platforms, which are based on a unidirectional flow to measure cells, the flow was reversed several times to shuttle a single cell back-and-forth through the measurement region.[41,42] The quality of the EIS signal of individual cells could thereby be improved by averaging results recorded during several reversals of the flow. Furthermore, the use of flow reversal allowed for multiple EIS measurements of the same cell before and after electroporation without any need for additional electrodes or immobilization structures.

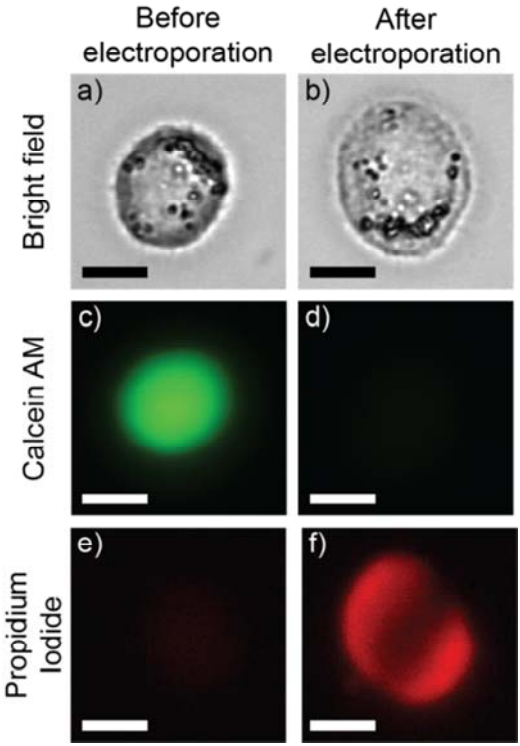

Figure 2.2. Microscope images of a HeLa cell before (left column, a), c), e)) and after (right column, b), d), f)) electroporation. Bright-field images (a) and b)) reveal an increase in size and a less-defined outer boundary of the cell. Fluorescence images of the life stain cAM show a bright viable cell before electroporation (c) and almost no fluorescence after electroporation (d). The fluorescent stain PI shows almost no fluorescence before electroporation, while the cell appears brightly red after electroporation (f), scale bar is 10 µm.

2.4.2 Single cell electroporation

Successful electroporation of single cells in the microchip was confirmed by conventional fluorescence microscopy of a single cell before and after a single exposure to the porating field. The cervical cancer cell line HeLa was one of the cell models used

in this study. This cell line was the first human cell line established in vitro[43] and has been widely characterized and studied.[44] After detachment from the culture flask and re-suspension in ISB, cells were introduced into the microchannel. Figure 2.2a shows a bright field microscopy image of a single intact HeLa cell before electroporation.

Initially, the viable HeLa cell has a round and clearly defined shape. Upon electroporation, the bright field image in Figure 2.2b showed morphological changes and a diameter increase of 23%. The increase of cellular diameter observed in the bright field images in Figure 2.2a and b suggests opening of the cellular membrane, leading to an uptake of liquid and swelling of the cell.[45]

Figure 2.2c and e show fluorescence microscopy images of the same HeLa cell as in Figure 2.2a before electroporation after applying the life stain cAM and PI. Electroporation was then achieved by exposing the cell to an electric field of 2 $kVcm^{-1}$ at 50 kHz in a single passage. After electroporation, the averaged fluorescence intensity of cAM decreased 10-fold, while the PI fluorescence intensity increased 5-fold, as shown in Figure 2.2d and f. The decrease of the fluorescence of the cellular life stain cAM shown in Figure 2.2c and d indicates the outflow of fluorescent molecules from the cell, a decrease of enzymatic activity and cell death upon electroporation. Uptake of PI into the cell is only possible if the membrane integrity is compromised, as it is the case for a dead, irreversibly or transiently porated cell. Since PI does not permeate the cell membrane, the increase of PI fluorescence in Figure 2.2e and f suggests PI uptake into the cell through openings of the cellular membrane, which have been formed upon exposure to the porating electric field. All results displayed in Figure 2.2 have been obtained from the same individual cell and confirm successful electroporation.

Once the successful electroporation of single cells was confirmed in several repetitions, the shuttling method was used to monitor the release of intracellular contents. Fluorescence microscopy image sequencing was used to study the dynamics of the intracellular-content release. Viable cells were labeled with cAM and exposed to the porating field, as shown in the image sequence of Supplementary Figure 2.1a. Initially (t = 0.0 s) the fluorescence image shows the round outline of the cell, which represents the fluorescence signal of the cAM-dyed intracellular content. After exposure to the electric field (t = 0.2 to 0.3 s) at the first pair of electrodes, the release of the intracellular content was evidenced by the formation of a fluorescent cloud around the cell. In order to visualize the fluorescent intracellular content leaking out of the cell, the camera gain was increased so that the optical signal of the cell itself was saturated at all times. The fluorescent cloud and tail behind the cell, which resulted from the parabolic flow profile, rapidly spread in the microchannel. It is noteworthy that release of the dye was observed immediately after the cell passed the electroporation region. The poration process occurred fast (< 0.1 s), which was beyond the resolution capabilities of the imaging hardware employed during the experiment. The cAM trace in the image sequence of Supplementary Figure 2.1a confirms the intracellular content release during 0.8 s after the application of the electric field. The platform and methodology used for electroporation of cells reported in this study demonstrated the immediate release of intracellular contents upon electroporation within less than 100 ms. Label-free EIS analysis was then used to further quantify cellular properties before and after electroporation.

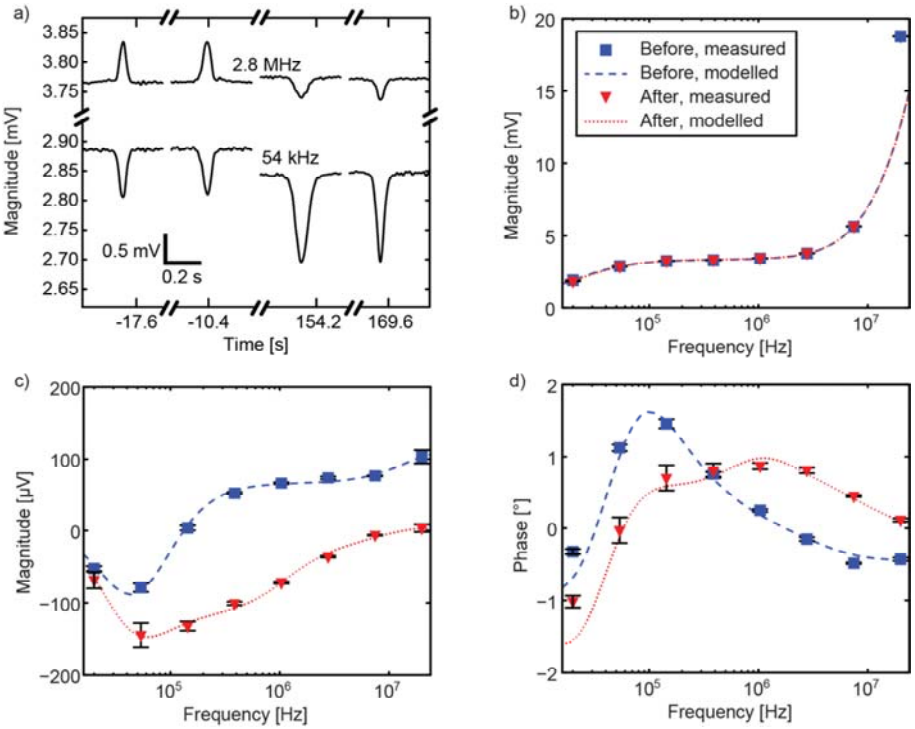

Figure 2.3. Impedance data of a one single HeLa cell before and after electroporation. (a) Time-domain signals at 53 kHz and 2.8 MHz show two successive passages of the cell before and after electroporation (occurring at t = 0 s). (b) The measured baseline signal evaluated at 8 frequencies (blue squares and red triangles) display the impedance of the microchannel. The ECM fit is represented with dashed lines. (c) Magnitude and (d) phase spectra of one single HeLa cell before and after electroporation: measured values are represented as squares (before electroporation) and triangles (after electroporation); the model fits are represented by blue dashed and red dotted lines, see legend in (b). The spectra in (c) and (d) are presented after baseline subtraction. All EIS results are from the same HeLa cell and have been acquired in parallel to the images shown in Figure 2.2. Error bars indicate the standard deviation for 5 measurements of the same single cell by shuttling the cell back and forth. Data of further cells can be found in Supplementary Figure 2.2.

2.4.3 Single cell EIS analysis

The additional pair of electrodes in the integrated platform, shown schematically in Figure 2.1, was used for the label-free EIS analysis of the cells both before and after electroporation. The previously described fluorescent cloud trailing behind the cell right after electroporation coincided with a similar observation in the electrical signal: The signal magnitude shown in Supplementary Figure 2.1b had a typical minimum in the 54 kHz signal magnitude component at 0.25 s. The signal amplitude was decreasing due to the at least partially intact cell membrane that prevented the low-frequency electric field from penetrating the cell volume. The following maxima at 0.4 s in the 54 kHz as well as in the 1 MHz component were due to the cloud of conductive cell contents following the cell – an analogous situation to the fluorescent cloud observed in Supplementary Figure 2.1a. The fluorescent and highly conductive cloud diffused throughout the volume of the channel and reduced the volume electrical resistance. Already a few seconds later no increase in fluorescence or impedance magnitude could be observed around the cell during the next passage between the electrodes. All impedance investigations that we conducted after cell electroporation were performed at least 30 s later than the time point of electroporation. This delay was necessary, since the cloud of larger conductivity material in the liquid due to released cellular contents around the cell had to diffuse away, so that the signal baseline level was no more affected.

Figure 2.3 presents EIS results for the electroporation of the same single HeLa cell that was optically monitored in Figure 2.2. Figure 2.3a shows the time domain signal magnitude, recorded at 54 kHz and 2.8 MHz. The signal is shown for the same cell passing twice through the measurement region before and after electroporation. The low-frequency signal magnitude showed a negative peak whenever the intact or electroporated cell was passing between the measuring electrodes. The cell membrane is

shielding the intracellular space at such frequencies from the electric field (large membrane capacitance) so that the current passing the microchannel is reduced whenever a cell is in the electric field between the electrodes. The 2.8 MHz signal showed a positive peak whenever the intact cell was passing the electrodes. At higher frequencies above the characteristic β-dispersion, the impedance of the cell membrane capacitance is decreasing.[30] Thus, the electric field which is now penetrating the membrane is passing the highly conductive intracellular liquid. The high conductivity of these intracellular liquids compared to the low conductivity extracellular medium leads to positive peaks as can be seen in Figure 2.3a when the intact cell passes between the EIS electrodes. In case of the electroporated cell, the 2.8 MHz signal shows the same negative peak as the 54 kHz signal, as the highly conductive cytosol has interdiffused with the surrounding solution upon electroporation. The cell membrane volume is less conductive than the surrounding liquid phase so that a small negative signal results.

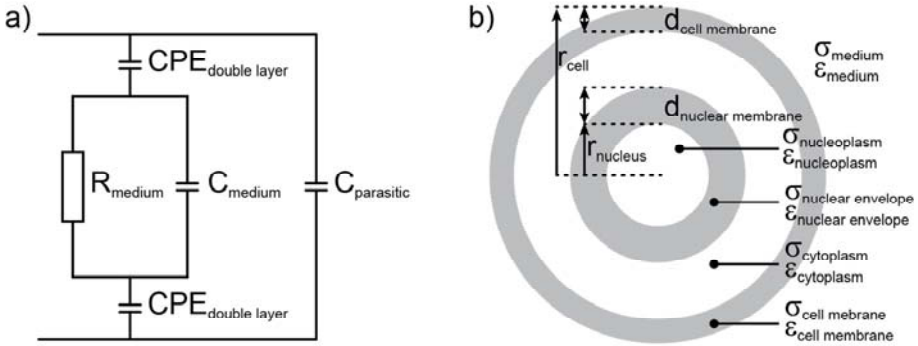

Figure 2.4. Electric equivalent-circuit models: a) equivalent-circuit model of the empty channel featuring constant-phase elements (CPEs) at the electrode-liquid interfaces, a resistor and capacitor for the medium in the channel and a parallel parasitic capacitance; b) three-shell model of the cell, consisting of the outer cell membrane, cytoplasm, nuclear envelope and nucleoplasm.

A total of eight frequencies were analyzed in parallel. The baseline level, i.e., the magnitude-versus-frequency measurements of the channel containing the liquid phase but no particle or cell are shown in Figure 2.3b. The spectrum shows a typical resistive plateau for frequencies between 100 kHz and 1 MHz. For lower frequencies the magnitude decreases due to the voltage drop over the electric double layer at the interface of the stimulus electrode and the medium. At higher frequencies the magnitude increases due to the increasingly conductive parasitic capacitance in parallel to the microchannel as well as due to capacitive coupling between the electrodes. An equivalent circuit model (ECM) is depicted in Figure 2.4a with fixed parameters given in Supplementary Table 2.2. Parameters obtained by fitting this model to the measured magnitude spectrum in Figure 2.3b have been used to extract characteristic parameters of the cell in a second step. The model of the channel was fitted to the first seven measured frequencies, as indicated by the dashed lines in Figure 2.3b. The baseline level at the highest frequency of 20 MHz is influenced by the overshoot of the bandwidth filter in the impedance spectroscope. Therefore this value is higher than expected from the simplified model that was used here and is omitted from the fit. Robustness of the fitting method is characterized by running the same procedure 100 times with different initial guesses. These initial guesses were chosen randomly within the limits specified in Table 2.1. Out of 100 fits, 98 cases were converging to a solution. Mean values and standard deviations are extracted in this way for three parameters summarized in Table 2.1: parasitic capacitance, extracellular medium conductivity (σ_{medium}) and double layer capacitance per surface area. Two separate fits were carried out for the conditions before and after electroporation of the same single cell. The extracted parameters before and after electroporation did not vary significantly, which along with small standard deviations of the measurements indicates the robustness of the fitting procedure even while varying initial guesses over several orders of magnitude. The

extracted medium conductivity of 148 mS/m is in good agreement with the value obtained by a conductivity meter (152 mS/m).

		Before		**After**		**Limits**	
Parameter	Unit	Mean	Std	Mean	Std	Min	Max
parasitic capacitance	fF	80.9	0.1	80.7	0.2	10^{-15}	1000
σ_{medium}	mS m^{-1}	148	0.4	149	0.04	1	10^4
double layer surface capacitance	mF m^{-2}	39.4	0.12	37.2	0.08	0.1	1000
r_{cell}	μm	6.6	0.2	7.6	0.03	3	9
$\log_{10}(\sigma_{cell\ membrane})$	$\log_{10}$(S m^{-1})	-9.1	1.4	-9.8	0.7	-10	-4
$\varepsilon_{cell\ membrane}$	-	22.5	0.3	7.6	0.2	1	30
$\sigma_{cytoplasm}$	mS m^{-1}	745	26	186	1.1	1	10^4
$\varepsilon_{nuclear\ envelope}$	-	4	0.26	7.3	0.04	1	100

Table 2.1. Parameters extracted from 100 fitting runs of an equivalent-circuit model of the microchannel and the three-shell model of the cell. The mean and standard deviation of the parameters over the 100 fitting runs with randomly chosen initial values is shown. The minimum ('min') and maximum ('max') limits of the different parameters for the fitting runs are also shown.

Electrical parameters of a single cell were extracted by fitting an established model of a three-shell sphere to the measured impedance signal magnitudes of the cell. The model, depicted in Figure 2.4b, was fitted to measured values of the cell before and after electroporation in two separate scenarios. By shuttling the cell back-and-forth, five succeeding peaks, similar to the ones depicted in Figure 2.3a, were averaged for each of the two scenarios. The baseline magnitude was subtracted from each peak magnitude to get a differential readout, which is independent of minor baseline drift. These averaged peak-to-baseline values were evaluated at each frequency to gain the magnitude spectrum of the cell shown in

Figure 2.3c. The same differential magnitude is calculated theoretically using the three-shell model and the equivalent circuit model of the microchannel discussed above. The calculated spectrum is fitted to the measured spectrum 100 times with different initial guesses randomly chosen within the range for each parameter indicated in Table 2.1. The fits for each of the two scenarios were converging to a solution in 98 cases (before electroporation) and in 81 cases (after electroporation) respectively. The mean values and standard deviation of the six parameters extracted from these fits are given in Table 2.1. The spectrum using the mean values of these parameters for the cell before and after electroporation are shown as dashed and dotted lines in Figure 2.3c. Since the signal magnitude at 20 MHz was subject to filter bandwidth overshoot, the fitting was carried out by using the first seven frequencies only. Since magnitude and phase component of the signal are not independent quantities, the fit was carried out by using only the signal magnitude. However, the phase component of the calculated spectra is still matching measured data shown in Figure 2.3d.

The extracted parameters in Table 2.1 indicate a swelling of the cell (15% increased radius) – in agreement with optical assessment – but also intactness of the membrane both before and after electroporation. The membrane conductivity was found to be less than 10^{-9} S/m. Such low Ohmic resistances are insignificant compared to the impedance of the membrane capacitance: Membrane conductivities up to 10^{-7} S/m do not lead to changes of the spectra depicted here. From these low conductivity values, we conclude that there are no larger pores of 10s of nm diameter in the cellular membrane. This is in agreement with sub-second resealing time constants for membrane pores.[33] The permittivity of the cellular membrane decreased upon electroporation. The corresponding decrease of the area-specific membrane capacitance $\left(C_m = \frac{\varepsilon_{cell\,membrane} \cdot \varepsilon_0}{d_{cell\,membrane}}\right)$ from 49.7 mF/m^2 to 16.9 mF/m^2 suggests an unfolding of membrane microstructures, such as microvilli and folds,

due to the swelling of the cell upon electroporation.[46,47] The cytoplasm conductivity decreased from 745 mS/m to 186 mS/m upon electroporation. We attribute this change to the exchange of highly conductive intracellular fluids with low-conductivity extracellular medium, which is supported by the fluorescence imaging in Supplementary Figure 2.1. The outflow of highly conductive cytosol and inflow of low-conductivity extracellular medium also decreased the conductivity in the nucleoplasm. The permittivity of the nuclear envelope was increased after electroporation, which also could be explained by membrane unfolding due to swelling of the nucleus. The values of all fixed or constant parameters are listed in Supplementary Table 2.2.

To confirm our results with another cell type, we used the cell line CHO-K1. The EIS experiment results for this cell line are shown in Supplementary Figure 2.2. The EIS signals from 5 individual CHO-K1 cells before and after electroporation show the same trend as measured and calculated the spectra obtained from the HeLa cell in Figure 2.3. The generally smaller magnitude and phase values are due to the smaller size of CHO-K1 cells as compared to HeLa cells.

2.4.4 Comparison of fluorescence and EIS analyses

The integrated platform was then used to investigate the effects and damages caused by electroporation on cells over time. The potential of the label-free EIS technique to detect changes in a single cell upon electroporation was evaluated by using established optical fluorescence techniques in parallel and for the same cells. Time-lapse fluorescence image acquisition and image postprocessing of the electroporation procedure of a single HeLa cell in medium containing the fluorescent stain PI are shown in Figure 2.5.

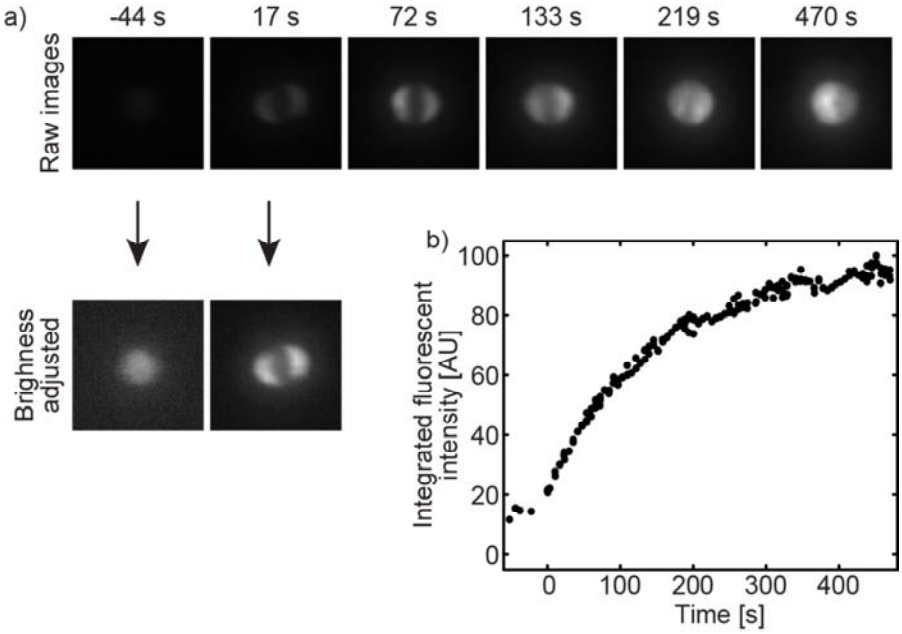

Figure 2.5. Time-lapse fluorescence images of a HeLa cell electroporation. The dye used in this experiment was PI. (a) Image sequence of the cell before and after electroporation shows the occurrence of highly fluorescent regions or lobes and subsequent interdiffusion within the cell volume. (b) Fluorescence intensity, integrated over a fixed-size square area around the cell, shows a characteristic increase of the fluorescence intensity upon electroporation (happening at t = 0 s).

Figure 2.5a shows a fluorescence image sequence of a HeLa cell over a time period of 470 s after the application of the electroporation field (t = 0 s) during a single cell passage. The insets show the cell in two separate brightness-adjusted images 44 s before and 17 s after electroporation. The image sequence revealed two fluorescent lobes at the cell soon after the electric field had been applied, suggesting inhomogeneous pore formation over the cellular membrane as has been theoretically described before and observed experimentally.[48–50] The regions of the cellular membrane closest to the facing electrodes were exposed to almost perpendicular electric

field lines. Therefore these top/bottom regions of the cell membrane experienced a larger electric field gradient across the membrane than regions along the side of the cell, where the electrical field lines are running in parallel to the membrane. This led to more intense membrane damage at the top and bottom regions of the cell and, thus, a more pronounced uptake of fluorescent dye in those regions. The dye then gradually diffused throughout the cell, and the overall cell fluorescence intensity increased during several minutes as displayed in Figure 2.5b, which is in agreement with PI incubation characteristics. [21,51,52]

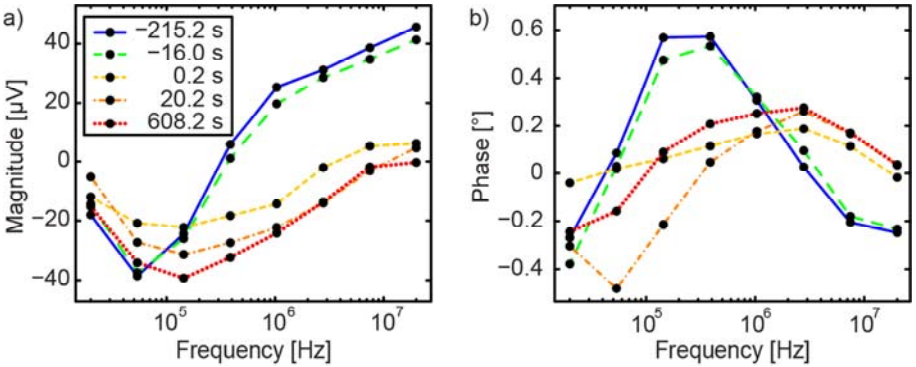

Figure 2.6. Temporal development of EIS signals (after baseline subtraction) of the same cell that has been optically analyzed in Figure 2.5 after electroporation: Signal magnitudes in a) and phase signal in b).

Figure 2.6 shows the EIS spectra at five selected time points of the same cell that was optically assessed in Figure 2.5 to assess the dynamics of the spectral changes. The spectra show trends comparable to those observed in Figure 2.3 and Supplementary Figure 2.2: Upon electroporation, the signal magnitude above 200 kHz decreased as indicated in Figure 2.6a, while the maximum in the phase spectrum decreased and shifted to higher frequencies as shown in Figure 2.6b. Electroporation of the cell (t = 0 s) induced spectral changes in both the magnitude and phase spectrum within the first 200 ms after the application of the electric field and did not

change significantly thereafter. This suggests that the exchange of intracellular contents and extracellular medium occurred within these first 200 ms.

To highlight these different dynamics – gradual diffusion of the fluorescent dye versus nearly instantaneous changes in the EIS data – different time points have been selected for the fluorescence and EIS data in Figure 2.5 and Figure 2.6.

2.5 Conclusion

We demonstrated a chip-based platform for the manipulation, electroporation and subsequent label-free analysis of single HeLa and CHO-K1 cells. With this system, we achieved (1) inversion of the flow direction allowing multiple EIS measurements of the same cell within few seconds allowing a) to assess the same cell at multiple time points or b) to average the results of multiple passages of the same cell, (2) successful electroporation of the cells upon application of an electrical stimulus of 8 V at 50 kHz and (3) monitoring and quantification of the electroporation process and its results through EIS. The platform also allowed for optical imaging of the cells prior to and after electroporation by means of established bright-field and fluorescence microscopy, so that the experiments and methods could be independently verified. Notably, the platform allowed for detailed investigations of a specific single cell before and after electroporation, without requiring cell immobilization. EIS analysis of both cell models that were used here (HeLa and CHO-K1) indicated cell swelling and exchange of intra- and extracellular medium upon electroporation.

Establishing a model of the microchannel and the cells allowed for extraction of electrical parameters in a label-free fashion. The platform presented here features robustness during operation and is straightforward to manufacture and to interface

to external equipment. Moreover, it can be combined with further downstream analysis steps, such as electron microscopy or mass spectroscopy for intracellular compound analysis. Additionally, the platform can be further developed in order to meet requirements of reversible single-cell electroporation for transfection or cell fusion.

2.6 Acknowledgements

Financial support was provided through Swiss Systems Biology Program “SystemsX.ch” within the RTD-project “CINA” and through the Commission for Technology and Innovation CTI, Switzerland, under project no. 11174.2 PFLS-LS. The authors acknowledge Hui Wang (Biotechnology and Bioengineering group, ETH Zürich, Basel) for initially providing the cells that were cultured and used in this work.

2.7 Supplementary information

Supplementary Video 2.1. Inversion of the flow speed showing the back-and-forth shuttling of a single cell.

Supplementary Video 2.2. Flow-through lysis of single cells.

20.000 kHz

53.654 kHz

143.916 kHz

386.140 kHz

1.036 MHz

2.779 MHz

7.455 MHz

20.000 MHz

Supplementary Table 2.1. Frequencies used for the EIS measurements

parameter	unit	value
channel height	µm	40
channel width	µm	50
electrode width	µm	18
double layer constant phase element exponent	-	0.95
ε_{medium}	-	80
$d_{cell\ membrane}$	nm	4.0
$\varepsilon_{cytoplasm}$	-	70
$r_{nucleus}$	µm	$(0.6\ r_{cell}^{3})^{1/3}$
$d_{nuclear\ envelope}$	nm	60
$\sigma_{nuclear\ envelope}$	mS/m	0.4
$\varepsilon_{nucleoplasm}$	-	70.0

Supplementary Table 2.2. Fixed parameters used to model the microchannel and the cell

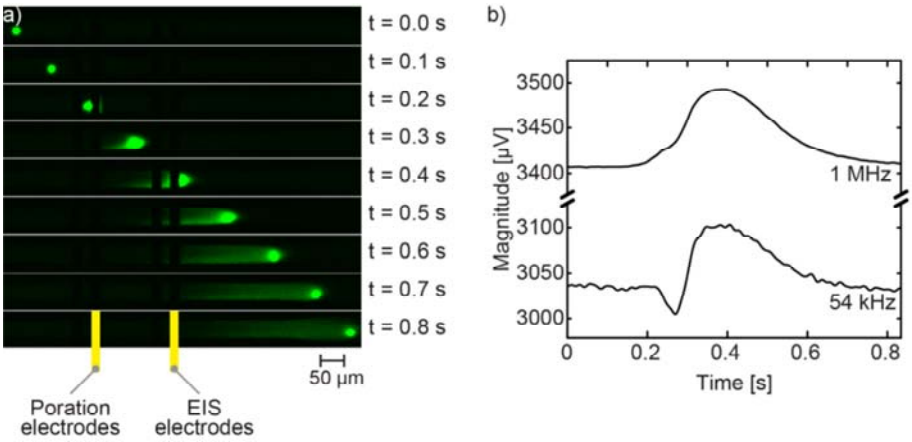

Supplementary Figure 2.1. Release of intracellular contents. a) Image sequence showing the release of fluorescent cell content (cAM) upon electroporation. The brightness settings have been increased to be able to visualize the cloud of fluorescent cell content that was released upon electroporation. Consequently, the brightness of the cell itself is now in saturation. Supplementary Video 2.2 displays this and other cells while undergoing electroporation. b) EIS measurement of a cell during the first electrode passage right after electroporation. The cell is passing the EIS electrodes at t = 0.3 s (minimum in the 54 kHz signal) followed by a cloud of conductive cellular contents (maximum at 0.4 s), and, then, the magnitude signals decay, as the conductive material diffuses away (after 0.7 s).

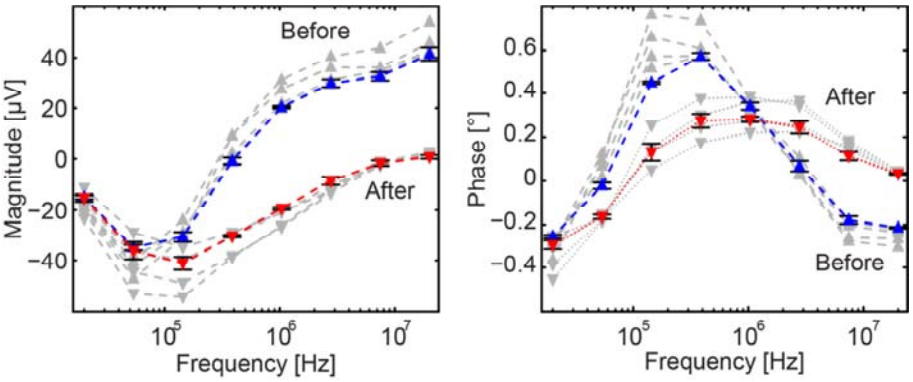

Supplementary Figure 2.2. Impedance spectra of 5 different CHO-K1 cells before (blue upward pointing triangles) and after lysis (red downward pointing triangles). One cell spectrum before and after lysis is highlighted in color for comparison, error bars indicate standard deviation of measurements from 5 passages of the cell before and after lysis.

2.7.1 Calculation of the induced trans-membrane voltage

We follow the methods by Sulhorukov et. al.[53] to obtain the transmembrane potential that is induced across the cell membrane of a cell, which is exposed to an AC voltage. The induced potential $V_{cell\ membrane}$ is:[49]

$$V_{cell\ membrane} = \frac{1.5 \cdot r \cdot E}{\sqrt{1 + (\omega \cdot \tau_{cell\ membrane})^2}}$$

We use the following values as parameters:

radius of the cell (extracted by fitting data to the ECM) $r = 6.6 \cdot 10^{-6}$ m

electric field strength $E = 2 \cdot 10^5$ V/m

angular frequency of the porating field $w = 2 \cdot p \cdot 50$ kHz

The relaxation time constant of the cell membrane $\tau_{cell\ membrane}$ is [48]:

$$\tau_{cell\ membrane} = r \cdot C_{cell\ membrane}\left(\frac{1}{\sigma_{cytoplasm}} + \frac{1}{2\sigma_{medium}}\right)$$

Here we use the following new parameters:

cell membrane capacitance per area $C_{cell\ membrane}$ = 0.15 F/m^2

cytoplasm conductivity (extracted by fitting data to the ECM) $\sigma_{cytoplasm}$ = 0.745 S/m

extracellular medium conductivity (extracted by fitting data to the ECM) σ_{medium} = 0.148 S/m

With the given parameters we get $\boldsymbol{V_{cell\ membrane}}$ **= 1.11 V**. It can also be concluded that a higher conductivity medium leads to more efficient electroporation: Higher values for σ_{medium} lead to lower time constants $\tau_{cell\ membrane}$ which in turn induces higher $V_{cell\ membrane}$ and thus more efficient pore formation.

Bibliography

1 Y.-C. Lin, C.-M. Jen, M.-Y. Huang, C.-Y. Wu and X.-Z. Lin, *Sensors Actuators B Chem.*, 2001, **79**, 137–143.

2 M. A. Aberg, F. Ryttsén, G. Hellgren, K. Lindell, L. E. Rosengren, A. J. MacLennan, B. Carlsson, O. Orwar and P. S. Eriksson, *Mol. Cell. Neurosci.*, 2001, **17**, 426–43.

3 J. S. Yoo, N. Won, H. B. Kim, J. Bang, S. Kim, S. Ahn and K.-S. Soh, *J. Appl. Phys.*, 2010, **107**, 124702.

4 A. M. Skelley, O. Kirak, H. Suh, R. Jaenisch and J. Voldman, *Nat. Methods*, 2009, **6**, 147–52.

5 M. B. Fox, D. C. Esveld, H. Mastwijk and R. M. Boom, *Innov. Food Sci. Emerg. Technol.*, 2008, **9**, 101–108.

6 H. C. Fan, J. Wang, A. Potanina and S. R. Quake, *Nat. Biotechnol.*, 2011, **29**, 51–7.

7 H. Sedgwick, F. Caron, P. B. Monaghan, W. Kolch and J. M. Cooper, *J. R. Soc. Interface*, 2008, **5**, S123–S130.

8 M. V Berezovski, T. W. Mak and S. N. Krylov, *Anal. Bioanal. Chem.*, 2007, **387**, 91–6.

9 D. Di Carlo, C. Ionescu-Zanetti, Y. Zhang, P. Hung and L. P. Lee, *Lab Chip*, 2005, **5**, 171–8.

10 H. Zhang and W. Jin, *Electrophoresis*, 2004, **25**, 1090–5.

11 D. Di Carlo, K.-H. Jeong and L. P. Lee, *Lab Chip*, 2003, **3**, 287–91.

12 K. R. Rau, A. Guerra, A. Vogel and V. Venugopalan, *Appl. Phys. Lett.*, 2004, **84**, 2940.

13 S. Wang and L. J. Lee, *Biomicrofluidics*, 2013, **7**, 011301.

14 H.-Y. Wang, A. K. Bhunia and C. Lu, *Biosens. Bioelectron.*, 2006, **22**, 582–8.

15 W. J. Dower, J. F. Miller and C. W. Ragsdale, *Nucleic Acids Res.*, 1988, **16**, 6127–6145.

16 H. Potter, *Proc. Natl. Acad. Sci. U. S. A.*, 1984, **81**, 7161–7165.

17 F. Han, Y. Wang, C. E. Sims, M. Bachman, R. Chang, G. P. Li and N. L. Allbritton, *Anal. Chem.*, 2003, **75**, 3688–3696.

18 S. Movahed and D. Li, *Microfluid. Nanofluidics*, 2010, **10**, 703–734.

19 D. C. Chang and T. S. Reese, *Biophys. J.*, 1990, **58**, 1–12.

20 Y. Huang and B. Rubinsky, *Biomed. Microdevices*, 1999, **2**, 145–150.

21 Y. S. Shin, K. Cho, J. K. Kim, S. H. Lim, C. H. Park, K. B. Lee, Y. Park, C. Chung, D.-C. Han and J. K. Chang, *Anal. Chem.*, 2004, **76**, 7045–52.

22 H.-Y. Wang and C. Lu, *Anal. Chem.*, 2006, **78**, 5158–64.

23 M. Shahini and J. T. W. Yeow, *Lab Chip*, 2013, **13**, 2585–90.

24 Z. Vasilkoski, A. Esser, T. Gowrishankar and J. Weaver, *Phys. Rev. E*, 2006, **74**.

25 V. L. Sukhorukov, R. Reuss, D. Zimmermann, C. Held, K. J. Müller, M. Kiesel, P. Gessner, A. Steinbach, W. A. Schenk, E. Bamberg and U. Zimmermann, *J. Membr. Biol.*, 2005, **206**, 187–201.

26 H. E. Ayliffe, A. B. Frazier and R. D. Rabbitt, *J. Microelectromechanical Syst.*, 1999, **8**, 50–57.

27 S. Gawad, L. Schild and P. H. Renaud, *Lab Chip*, 2001, **1**, 76–82.

28 D. Holmes, D. Pettigrew, C. H. Reccius, J. D. Gwyer, C. van Berkel, J. Holloway, D. E. Davies and H. Morgan, *Lab Chip*, 2009, **9**, 2881–9.

29 T. Sun and H. Morgan, in *Microfluidics Based Microsystems*, eds. S. Kakaç, B. Kosoy, D. Li and A. Pramuanjaroenkij, Springer Netherlands, 2010, pp. 507–527.

30 S. Gawad, K. Cheung, U. Seger, A. Bertsch and P. Renaud, *Lab Chip*, 2004, **4**, 241–51.

31 W. Wang, K. Foley, X. Shan, S. Wang, S. Eaton, V. J. Nagaraj, P. Wiktor, U. Patel and N. Tao, *Nat. Chem.*, 2011, **3**, 249–55.

32 M. Khine, C. Ionescu-Zanetti, A. Blatz, L.-P. Wang and L. P. Lee, *Lab Chip*, 2007, **7**, 457–62.

33 H. He, D. C. Chang and Y.-K. Lee, *Bioelectrochemistry*, 2008, **72**, 161–8.

34 G. Mernier, W. Hasenkamp, N. Piacentini and P. Renaud, *Procedia Eng.*, 2010, **5**, 37–40.

35 J. Teissié and M. P. Rols, *Biophys. J.*, 1993, **65**, 409–13.

36 K. Kinosita and T. Y. Tsong, *Nature*, 1977, **268**, 438–441.

37 A. Irimajiri, T. Hanai and A. Inouye, *J. Theor. Biol.*, 1979, **78**, 251–269.

38 Y. Polevaya, I. Ermolina, M. Schlesinger, B.-Z. Ginzburg and Y. Feldman, *Biochim. Biophys. Acta - Biomembr.*, 1999, **1419**, 257–271.

39 K. Asami, *Prog. Polym. Sci.*, 2002, **27**, 1617–1659.

40 J. Schindelin, I. Arganda-Carreras, E. Frise, V. Kaynig, M. Longair, T. Pietzsch, S. Preibisch, C. Rueden, S. Saalfeld, B. Schmid, J.-Y. Tinevez, D. J. White, V. Hartenstein, K. Eliceiri, P. Tomancak and A. Cardona, *Nat. Methods*, 2012, **9**, 676–82.

41 D. Holmes and H. Morgan, *Anal. Chem.*, 2010, **82**, 1455–61.

42 K. Cheung, S. Gawad and P. Renaud, *Cytom. Part A J. Int. Soc. Anal. Cytol.*, 2005, **65**, 124–32.

43 G. O. Gey, W. D. Coffman and M. T. Kubicek, *Cancer Res.*, 1952, **12**, 264–265.

44 J. J. M. Landry, P. T. Pyl, T. Rausch, T. Zichner, M. M. Tekkedil, A. M. Stütz, A. Jauch, R. S. Aiyar, G. Pau, N. Delhomme, J. Gagneur, J. O. Korbel, W. Huber and L. M. Steinmetz, *G3 (Bethesda).*, 2013.

45 Maša Kandušer and Damijan Miklavčič, in *Electrotechnologies for Extraction from Food Plants and*

Biomaterials, eds. E. Vorobiev and N. Lebovk, Springer New York, New York, NY, 2009, pp. 1–37.

46 S. Memmel, V. L. Sukhorukov, M. Höring, K. Westerling, V. Fiedler, A. Katzer, G. Krohne, M. Flentje and C. S. Djuzenova, *PLoS One*, 2014, **9**, e87052.

47 P. R. C. Gascoyne, S. Shim, J. Noshari, F. F. Becker and K. Stemke-Hale, *Electrophoresis*, 2013, **34**, 1042–50.

48 E. Jeltsch and U. Zimmermann, *Bioelectrochemistry Bioenerg.*, 1979, **6**, 349–384.

49 C. Holzapfel, J. Vienken and U. Zimmermann, *J. Membr. Biol.*, 1982, **67**, 13–26.

50 M. Golzio, J. Teissie and M.-P. Rols, *Proc. Natl. Acad. Sci. U. S. A.*, 2002, **99**, 1292–7.

51 R. Meissner, B. Eker, H. Kasi, A. Bertsch and P. Renaud, *Lab Chip*, 2011, **11**, 2352–61.

52 J. K. Valley, S. Neale, H.-Y. Hsu, A. T. Ohta, A. Jamshidi and M. C. Wu, *Lab Chip*, 2009, **9**, 1714.

53 V. L. Sukhorukov, H. Mussauer and U. Zimmermann, *J. Membr. Biol.*, 1998, **163**, 235–45.

3 ON-CHIP LYSIS OF MAMMALIAN CELLS THROUGH A HANDHELD CORONA DEVICE

C. Escobedo*, S. C. Bürgel*, S. Kemmerling, N. Sauter, T. Braun and A. Hierlemann

Published in *Lab on a Chip*

doi: 10.1039/C5LC00552C

* Both authors contributed equally.

3.1 Abstract

On-chip lysis is required in many lab-on-chip applications involving cell studies. In these applications, the complete disruption of the cellular membrane and a high lysis yield is essential. Here, we present a novel approach to lyse cells on-chip through the application of electric discharges from a corona handheld device. The method only requires a microfluidic chip and a low-cost corona device. We demonstrate the effective lysis of BHK and eGFP HCT 116 cells in the sub-second time range using an embedded microelectrode. We also show cell lysis of non-adherent K562 leukemia cells without the use of an electrode in the chip. Cell lysis has been assessed through the use of bright-field microscopy, high-speed imaging and cell-viability fluorescence probes. The experimental results show effective cell lysis without any bubble formation or significant heating. Due to the simplicity of both the components involved and the lysis procedure, this technique offers an inexpensive lysis option with the potential for integration into lab-on-a-chip devices.

3.2 Introduction

After a few decades of development, lab-on-a-chip (LOC) platforms offer a wide variety of applications in chemistry, physics and life sciences.[1] Among the numerous applications in the portfolio of LOC devices, the interrogation of individual cells in microfluidic environments has played a key role in “omics” sciences.[2,3] The extraction of intracellular components is a key process in many of these applications, including metabolomics, genomics and proteomics, and is usually achieved through a lytic procedure.

Different cell lysis techniques have been demonstrated to be suitable for lab-on-chip integration, relying on established approaches using mechanical, chemical, electrical and optical means.[4–6] New approaches have also been reported in recent years,

such as the use of titanium oxide particles,[7] which evidence ongoing research and efforts in developing on-chip cell lysis methods. In all cases, the effective disruption of the cell membrane is required in order to access the intracellular contents for further analysis, whereat the potential side effects have to be considered. Mechanical lysis involves the use of pressure, shear forces or vibration, which may generate strong forces and heat, leading to the potential denaturalization of intracellular components such as proteins.[8,9] Enzymatic and chemical lysis is probably the most widespread methodologies used to date. This can be achieved through straightforward procedures, but they may involve reagents that can interfere with the subsequent analyses methods. Furthermore, they may entail long incubation times, which are associated with protein degradation and elevated costs for both the lysis itself and the removal of the lytic enzyme from the product.[10,11] Optical lysis, using laser beams for instance,[12] can be highly efficient but requires bulky equipment and is, in general, costly.[13]

Electrical lysis (EL) relies on the creation of pores in the cellular membrane leading to its non-reversible disruption upon exposure of the cell to strong electric fields. The pores in the cellular membrane are formed when the transmembrane potential (TMP) exceeds a threshold of ~1 V.[14,15] Both direct current[16–18] (DC) and alternating current (AC) electric fields have been used for electroporation and cell lysis not only in conventional microfluidic platforms but also in droplet-based formats that allow for enclosure of preselected cells and spatial confinement of the intracellular contents after lysis.[19] DC electric fields were originally preferred, as they provide a larger TMP without affecting intracellular components.[11] However, for electric field strengths in the kV/cm range, this approach may lead to water electrolysis resulting in gas bubble formation.[20] For this reason, AC electric fields have been used in many on-chip lysis applications at frequencies as low as 1 Hz.[21] Depending on the intensity and duration of the applied electric field, both DC and AC electric field lysis techniques lead to Joule heating, and their efficacy depends on

the spatial distribution of the electric field. In all previously reported cases, the lysis efficiency was always a concern and the fraction of lysed cells of many of the abovementioned methods is well below 100%.[11]

Corona discharges in liquids[22–24] are commonly used for tissue ablation, microorganism annihilation in water treatment and chemical analysis.[25] Corona discharges can be applied by compact, handheld systems, which have been used in the past for the surface treatment of polymeric microchannels,[26] and for microfluidic actuation through microelectrodes integrated into the respective microfluidic chips. These devices provide electric pulses that may be accompanied by corona glow, and irrespective of the medium, deliver electric fields on the order of kV at minimal electric currents.[23,27] Commonly, a corona glow is observed with non-thermal corona discharges devices that are used in the gas phase, where the mean free path is large enough to enable electron multiplication.[28] Corona electric discharges have been used in different microfluidic applications including liquid actuation in microchannels[26,29] and particle trapping and concentration.[30] Non-thermal corona discharges have also been reported in liquid media, including water-based solutions.[23] In liquids, streamers and corona glow may exist as a consequence of a breakdown mechanism that facilitates the corona discharge initiation, as demonstrated in the past.[31–33] However, the theories behind these phenomena are diverse without a unified or fully descriptive theory.[34,35] Water breakdown through corona discharges, and related undesirable effects, such as heating and bubble formation, require applied electric fields of more than MV/cm. Nonetheless, electric fields on the order of kV/cm, which can be efficiently delivered by simple handheld corona devices, may be sufficient to achieve cell lysis.

Here we present a new technique for on-chip cell lysis using electric discharges from a handheld corona device. The electric discharges are applied through a microelectrode integrated into a microfluidic

chip. This approach delivers a confined and intense electric field, with low electric current. This enables an efficient lysis of baby hamster kidney (BHK-21) and GFP-expressing human colon carcinoma line 116 (HCT 116) cells in proximity of the microelectrodes. Experimental results demonstrate effective lysis of the cells in the vicinity of the microelectrode without heating or bubble formation. Additionally, we demonstrate that the corona discharge can be applied directly to the liquid, without the use of any metallic electrode to enable bulk cell lysis of non-adherent K562 leukemia cells. Confirmation that no heating effects occurred as a consequence of the applied electric fields was provided by fluorescence microscopy using temperature sensitive Rhodamine B. The corona-device-based method enables effective and fast cell lysis while using inexpensive instrumentation and comparably simple microstructures, and is suitable for integration with microfluidics into lab-on-chip formats.

3.3 Materials and methods

3.3.1 Chip fabrication and integration

The microfluidic chip was fabricated in poly(dimethylsiloxane) (PDMS) by using standard replica molding techniques reported elsewhere.[36] Two openings were punched through the entire thickness of the PDMS layer to facilitate the access and removal of fluid containing cells. A 400-nm-thick Pt microelectrode was fabricated on a glass wafer on a 20-nm-thick TiW adhesion layer using standard metal deposition and selective etching by means of photoresists on a glass wafer. The microfluidic PDMS layer was bonded to the glass layer containing the patterned microelectrode via oxygen plasma exposure and a post-baking step at 60°C for 10 minutes, which aligned the central observation chamber of the microfluidic chip to the tip of the electrode. A schematic representation of the integrated chip assembly is shown in

Figure 3.1. The chip was connected to a BD-20ACV corona handheld device (Electro-Technic Products Inc., Chicago, IL) by connecting the distal end of the microelectrode to the corona wire electrode provided by the manufacturer.

3.3.2 Cell preparation

Baby hamster kidney fibroblasts (BHK-21, ECACC 85011433) were cultured in polystyrene T75-flasks containing DHI-5 medium at 37 °C and 5% carbon dioxide. The cells were detached using trypsin-EDTA solution (0.05% Trypsin, 0.53 mM EDTA; 25300-054, Invitrogen, Switzerland), followed by incubation at 37 °C for 5 min and subsequent dilution at 37 °C with DHI-5 medium. Before the experiments, the medium and the cells were washed with 37 °C warm PBS (Dulbecco's Phosphate Buffered Saline; D8662, Sigma, Switzerland), ISB (isotonic sucrose buffer: 0.25 M sucrose, Bio-Rad, 161-0720; 5 mM HEPES pH 7.4, AppliChem A3724; conductivity 87 mS/cm) or HEPES buffer (0.15 M NaCl; 20 mM HEPES pH 7.4; 5.5 mM KCl; 2 mM CaCl2; 1 mM MgCl2; conductivity 60 mS/cm). A second batch of BHK cells was prepared following the same protocol but kept in suspension through trypsinization to prevent cell adhesion to the surface of the chip or microelectrodes. GFP-expressing human colon carcinoma (GFP HCT-116) cells were obtained from Sirion Biotech (Sirion Biotech GmbH, Germany) and grown to confluence in RMPI 1640 medium, supplemented with penicillin/streptomycin (100 U/100 µg/ml) and 10% Fetal Calf Serum (FCS). For the fluorescence-based experiments, the cells were re-suspended in isotonic sucrose buffer (sucrose, 250 mM), HEPES (10 mM), EDTA (5 mM) adjusted to pH 7.4 and seeded with PI (25 µg/ml) and FDA (4 µg/ml). Nonadherent human chronic myelogenous leukemia K562 cells (ATCC CCL-243, LGC Standards GmbH) were cultured in cellstar flasks containing RPMI 1640 medium with 2.05 mM L-Glutamine (HYCL SH30027.02, GE

Healthcare) supplemented with 10% HyClone Fetal Bovine Serum (HYCL SH300710, GE Healthcare).

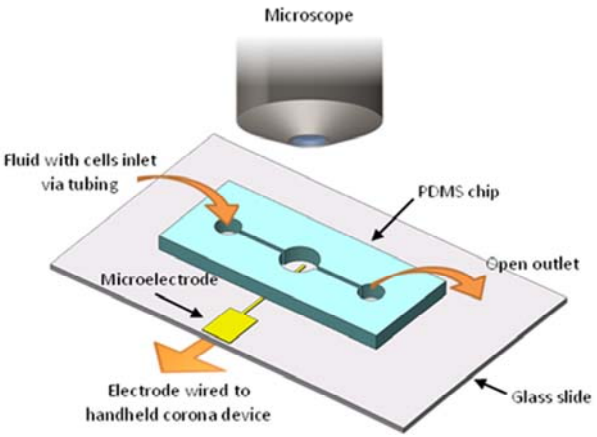

Figure 3.1. Schematic representation of the chip used in the cell lysis experiments. A microfluidic PDMS chip was affixed onto a glass slide containing the fabricated platinum microelectrodes. The microelectrodes were further connected to the corona handheld device.

The cells were grown to a density of 10^6 cells/ml and diluted every 3 days to a density of 10^5 cells/ml by removing cell suspension and refilling with fresh medium. For the fluorescence-based experiments, the cells were used at a density of 10^6 cells/ml and the medium was supplemented with the fluorescent life stains fluorescein diacetate (FDA, F7378, Sigma Aldrich) or calcein AM (cAM, C3100MP, life technologies) at concentrations of 2 μM, and the dead stain propidium iodide (PI, P4864-10ML, Sigma-Aldrich) at a concentration of 10 μM.

3.3.3 Image acquisition

Imaging was achieved by using upright visualization with a MacroFluo stereo microscope (Leica Microsystems GmbH, Germany) and an Olympus AX70TRF upright epi-fluorescent microscope. Bright-field visualization and image acquisition were

performed by using direct light from a halogen lamp source, whereas fluorescence imaging was done by using a mercury-vapor lamp source and GFP (excitation filter BP470/40 nm and emission filter BP525/50 nm) and Y3ET (excitation filter BP545/30 and emission filter BP610/75) filter cubes. The imaging system allowed for switching between the different light sources and filter cubes throughout the experiments. Images used for optical inspection of the preliminary lysis experiments were captured with a DFC 340 FX digital camera (Leica Microsystems GmbH, Germany), and the rest of the images was acquired using a MiroEX4 high-speed CCD camera (Vision Research, NJ), respectively. All the settings in the cameras, including exposure and gain, were set to manual and kept constant throughout the experiment. Image analysis and processing was done by using ImageJ software. For the experiments involving Rhodamine B dye, the initial fluorescence intensity value was set to one and all subsequent acquired images were normalized using this value.

3.3.4 Cell lysis

Microfluidic solution delivery was accomplished via a micro-screw syringe pump (Harvard Apparatus, MA) through 1/16 inch OD tubing connected to the punched inlet and outlet of the chip assembly. The chip was rinsed with DI water prior to introduction of the solutions with cells. After rinsing, the integrated chip, shown schematically in Figure 3.1, was loaded with BKH-21 cells. Once cells were visualized in the region of interest (ROI), the syringe pump was stopped, and the chip assembly was left undisturbed for exactly 2 minutes, which allowed floating cells to settle down onto the surface of the microelectrode. Prior to application of the electric discharge through the chip electrode, the corona device was set for delivering voltages of 10, 20 and 30 kV by adjusting the voltage level knob in the device and by measuring the voltage delivered at the tip electrode using a peak voltage calibrator (Model 12701, Electro-

Technic Products Inc., Chicago, IL). An electric discharge was then applied to microelectrode in the chip assembly, and images were acquired simultaneously throughout the process. Bulk lysis of non-adherent cells without using any metallic microelectrode was achieved by using the conductive liquid in the microfluidic chip to deliver the corona discharge to the cells.

3.4 Results and discussion

The experimental set up shown in the schematic of Figure 3.1 was used in bright-field (BF) mode to visualize the lysis process in the chip. After loading with cells, the chip was left to rest for about two minutes allowing the cells to settle on top of the microelectrode as documented by BF imaging. A brief electric discharge lasting ~2 seconds was applied via the handheld corona device and subsequently an image was immediately acquired. The central parameter to achieve lysis of mammalian cells through electrical discharge is the transmembrane potential which, according to experimental evidence to date, must exceed ~1 V.[37] However, many experimental studies demonstrate that this potential threshold may lead to reversible electroporation of the cell membrane and suggest that higher voltages are required for effective disruption of the cell membrane.[11,38] The relationship between transmembrane potential, inherent cell properties and frequency of the applied voltage can be estimated through the following expression:[39–41]

$$\Delta\varphi = 1.5\ r\ E_0 / (1 + (2\ \pi\ f\ \tau)^2)^{1/2} \qquad (1)$$

where r is the radius of the cell, E_0 is the external field strength, f is the frequency of the applied electric AC field, and τ is the relaxation time constant of the plasma membrane polarization, defined by the cell membrane capacitance per unit area, C_m, and the intracellular and extracellular resistivities, ρ_{int} and ρ_{ext} as follows:[38,42]

$$\tau = r\ C_m\ (\rho_{int} + (\rho_{ext} / 2)) \qquad (2)$$

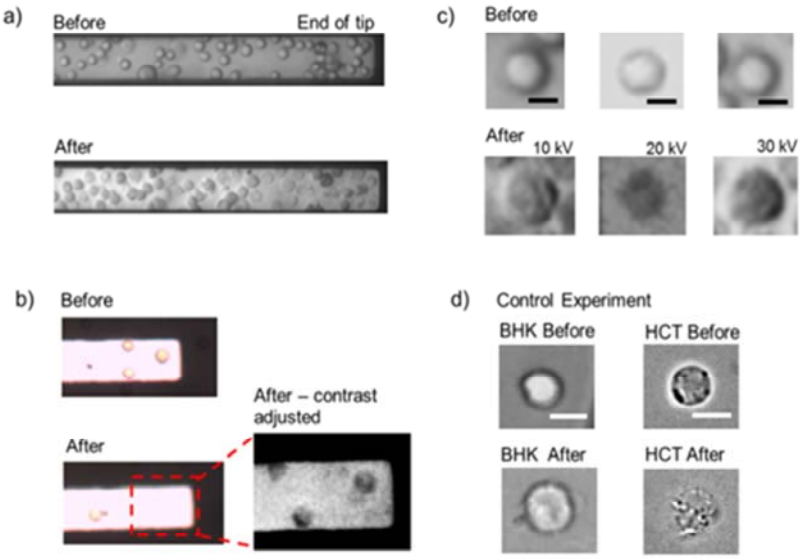

Figure 3.2. Optical images of non-trypsinized BHK cells before and after corona or electric discharge. (a) Bright-field images of multiple cells on top of the microelectrode before and after applying the corona electric field. (b) Same experiment, tracking the fate of three preselected cells. By adjusting the contrast of the image, the lysed cells can be observed. (c) Same experiment, tracking three pre-selected cells at three different applied voltages. (d) Control experiment using an electrical lysis method as described in the SI.

Below are typical values for the parameters in equations (1) and (2) for mammalian cells:[38–40,43] $C_m \sim 10^{-6}$ F cm^{-2}, $\rho_{int} \sim 100$ Ω m, $\rho_{ext} \sim 10$ Ω m, and $r \sim 10^{-5}$ m. The electrical field required for cell lysis is in the 10 kV/cm range. The electric potential delivered by the handheld corona device at ~ 4.5 MHz is above this threshold, but below the limit for breakdown of the liquid phase, as mentioned earlier. Under these conditions, the cells close to the electrode experience a strong dielectrophoretic force towards the electrode (more information in the SI), so that lysis occurs shortly afterwards.

In order to investigate bulk cell lysis, a chip without metallic microelectrodes was employed. In this case, the corona discharge was directly applied to the liquid medium through the inlet of the chip and reached the cells via the conductive medium. To elucidate the details and conditions of the lysis process, we conducted experiments while applying bright field and fluorescence imaging techniques as will be described below. In Figure 3.2, BF images before and after the application of the electric discharge are shown. For these tests, both BHK and HCT cells were used. In Figure 3.2a, most BHK cells seem to be in good condition with a well-defined round shape before the electric discharge. In contrast, after applying the electric discharge, the cells appear to have been flattened out, presumably lysed, which is in accordance with results reported in the past.[8,12] Of note is that the density of lysed cells is high in this case, ~10^9 cells/ml, and that lysis occurred for all cells in contact with or near the electrode. This opens up the possibility to control the number of cells to be lysed by modifying the volume of the microfluidic layer above the electrode. The increased cell density on the electrode in Figure 3.2a suggests that additional cells may have settled down in the time between taking the before-lysis image and the subsequent application of the discharge. Figure 3.2b shows BF pictures focusing on three specific BHK cells at the tip of the microelectrode before and after the application of a sub-second discharge. Before the discharge, the cells are perfectly round, lying on top of the microelectrode. After the discharge, the cells seem to have disappeared from the field of view. However, after adjusting the contrast of the image, the silhouettes of the cells can be observed, similar to Figure 3.2a. The subtle smear and seemingly flat profile of the cells over the microelectrode suggest that the viability of the cells has been compromised and that the cell membranes most likely have been disrupted. In other words, the three cells under study seem to have been lysed upon the application of the electric discharge. The additional live cell that appears in the after-lysis image, in all likelihood, settled down after the electric discharge. The

fact that this live cell can be observed at the original intensity and contrast settings further evidences the lysed state of the three cells of interest, similar to previously reported results.[44] In order to investigate the dependence of the lysis results on the applied voltages, the same corona lysis procedure was repeated using three pre-selected BHK cells and applied voltage settings to deliver 10, 20 and 30 kV through the corona device. The range of applied voltages is a consequence of the limited range of power settings of the device. Nevertheless, the experiments allowed for elucidating the effects of potential variation on corona lysis efficacy. The experimental setup was identical to that of the experiments previously described. The electric discharge was, however, applied off-stage to avoid any potential damage to the equipment as the associated electromagnetic field may disturb electronics due to the high frequency and high voltage delivered to the electrode from the internal coil in the handheld device. Figure 3.2c shows the bright-field images of the pre-selected cells before and after application of the three voltages. The images do not show any apparent difference between the three cells. All three cells look deformed and feature cellular debris in their vicinity, which suggests that lysis has occurred in similitude to other reported lysis studies.[11,44] Figure 3.2d shows the bright field pictures of a control experiment using an established electrical lysis protocol for BHK and HCT cells reported elsewhere.[38] Details on the applied electrical lysis procedure are provided in the Supporting Information (SI) section.

In order to study the time scales and the course of the cell lysis in more detail, we employed a high-speed camera to acquire images with a temporal resolution of milliseconds. For this experiment, we used trypsinized BHK cells to prevent adhesion to the electrode surface, so that they behaved similar to non-adherent cells or cells in suspension. The same experimental procedure for applying the electric discharge as described above Figure 3.2a was used in this experiment. Figure 3.3 shows an image sequence of three preselected BHK cells during the application of the electric discharge

over 2.5 s. In the row showing raw images, the cells undergo the same fate than those shown in Figure 3.2. However, in this image sequence, the increase in volume at time t_1 and t_2 is evident, which evidences damage to the cellular membrane during the treatment. During the experiments we observed pDEP forces so that nearby cells got attracted to the electrode.

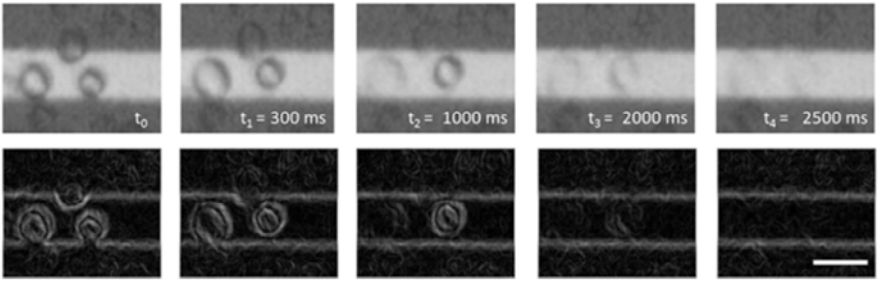

Figure 3.3. Image sequence of BHK cells during the application of the electric discharge using the corona apparatus. Top row: bright field raw images. Bottom row: corresponding processed images using an edge detection Sobel filter. The processed images suggest cell membrane disruption of the largest cell as early as 300 ms after the application of the electric field. The scale bar is 20 microns.

However, we also observed that more distant cells were pushed away from the electrode region due to, presumably, electrokinetic effects that produced flow. The pDEP forces seem to extend only over a small distance from the electrode, a distance similar to a cell diameter (more details in the SI). Different motion regimes related to DEP forces and depending on the magnitude rate of the real and imaginary Clausius-Mossotti factors have also been reported on in literature.[45] The bottom row in Figure 3.3 shows the same images as in the upper row after processing with an edge detection filter. The filter worked particularly well for the two cells laying entirely over the microelectrode as a consequence of the light contrast between the background and the edges of the cells. It is important to note the optical shortcoming of the processed images at the region where the

cell and the electrode overlap. However, the use of the filter allowed recognizing the edges of the cells, evidencing their morphological change and volume increase over time. As evidenced by the processed image sequence, the disruption of the membrane of the two cells located at the left and at the top was observed as early as 300 ms after the lysis pulse, and complete lysis achieved in less than one second.

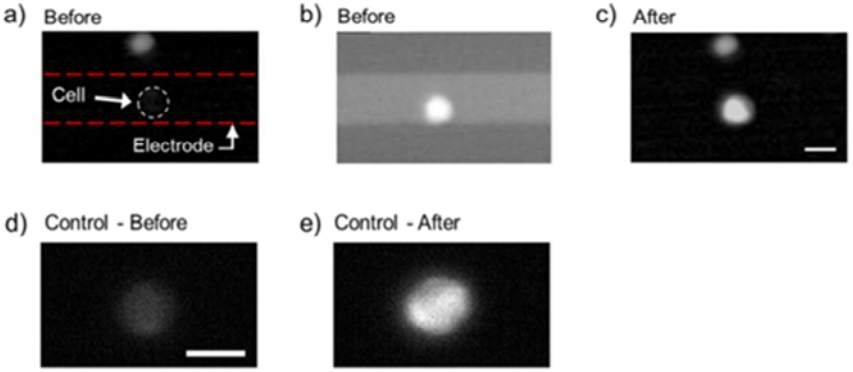

Figure 3.4. Cell lysis of eGFP HCT 116 cells in PI solution. (a) Image of the viable cell taken using emission filter BP610/75 before applying the electric discharge. (b) Image taken using the emission filter BP525/50 before applying the electric discharge. The living cell of interest is visible while the close-by dead cell does not fluoresce. (c) Image taken using the emission filter BP610/75 after the application of the electric discharge. The fluorescence signal from the cell of interest evidences the effective lysis. (d-e) Control experiments with electrical lysis of HCT cells while using a PI stain. Details on the control experiment are available in the SI. Scale bars are 10 microns.

The cell on the right settled down onto the electrode later, as evidenced by the relocation between t_0 and t_1, which resulted in a delayed lysis onset relative to the other two cells. The volume increase of the cells over time indicates the extracellular medium intake and evidences cell lysis, in a way similar to other methodologies.[46] The time to achieve the lysis of the cells was

comparable in both cases and noticeably faster than that of other methods reported in the literature.[11]

The cell lysis results using bright field microscopy were further validated by applying fluorescent dyes commonly used in cell viability studies.[47] A solution containing FDA and PI was used to assess the viability and non-viability of the cells in the experiments as shown in Figure 3.4. First, the viability of BHK cells was monitored by using the GFP filter in the fluorescence microscope, as FDA is a compound that is actively transformed by viable cells into fluorescein at a peak emission wavelength of ~520 nm. Under these conditions, a cell is observable only while it is still viable. Figure 3.4a shows an image sequence of a preselected viable cell undergoing lysis upon the application of the electric discharges via the corona device. The cell is clearly visible prior to the corona treatment and the fluorescence signal of the cell then fades away within 100 ms after the electrical discharge has been applied. The color map of the processed image evidences the round profile of the cell and the signal characteristics before and after lysis. Figure 3.4b shows an image sequence employing an inverse approach, in which only the fluorescence signal from non-viable cells is picked up, through the use of the Y3ET filter. A viable cell was preselected using BF, and the microscope was then switched to fluorescence mode. The cell was therefore invisible prior to the application of the electric discharge as shown in the upper figure. Upon application of the electric discharge, the compromised cellular structure resulted in the intake of medium by the cell and a resulting fluorescence signal as shown at the bottom Figure of Figure 3.4b. These results confirm that the cells were in fact lysed and did not simply vanish from the region of observation.

We employed GFP-expressing HCT cells to further validate the lysis method. Fig. 5 shows images of a preselected viable cell before and after the application of the electric discharge. A viable cell was first preselected using BF.

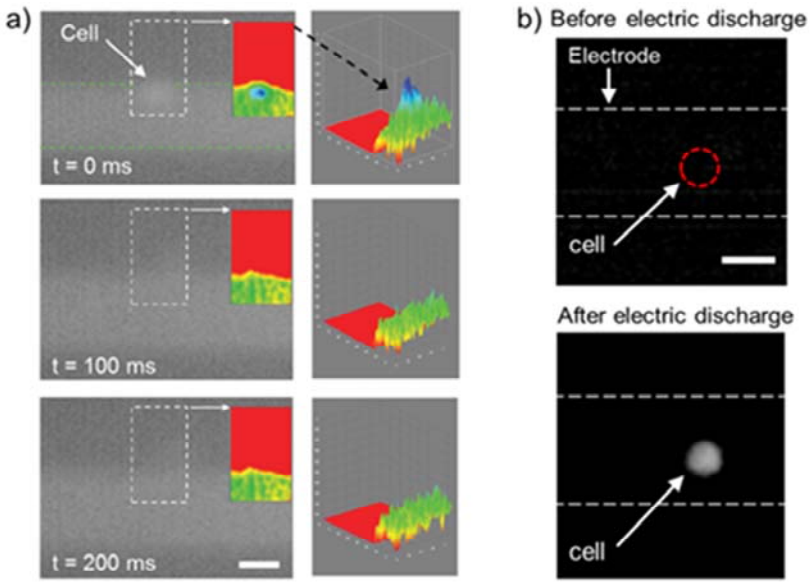

Figure 3.5. Fluorescence cell lysis experiments using BHK cells and fluorescence viability stains. (a) Experiment using FDA as cell viability stain. The cell exhibits fluorescence before the application of the electric field, and the fluorescence intensity decreases within a period of ~100 ms. (b) Experiment using PI as cell non-viability stain. The time between images is less than 3 seconds. The scale bar is 10 microns.

The Y3ET filter was then used for acquiring the picture in Figure 3.5a. The lack of fluorescence signal from the cell of interest indicates its viability. In contrast, a close-by dead cell can be observed in the same picture due to the fluorescence emission upon PI intake by that cell. The GFP filter cube was then used to acquire the fluorescence image shown in Figure 3.5b. The signal captured in this image corresponds to the fluorescence emitted directly by the GFP from the viable cell. In contrast to Figure 3.5a, the close-by cell now did not exhibit any fluorescence in Figure 3.5b, which confirms its non-viability already before the lysis treatment. Next, an electric discharge of less than 1 second was applied via the corona device, replicating the lysis experimental procedure used in the previous

experiments. The picture in Figure 3.5c was taken immediately after the treatment using the Y3ET filter cube. The fluorescence of the cell of interest in this picture suggests that the cell has been effectively lysed: there is only PI fluorescence emission in contrast to Figure 3.5a and Figure 3.5b.

The concurrent fluorescence emission of both, the cell of interest and the close-by already initially dead cell observed in Figure 3.5c provide further proof for the non-viability of healthy and intact cells after lysis treatment. Bubble formation was not observed in any of the experiments, so that electrolysis or hydrolysis due to the applied electric field can be excluded. Lytic effects due to formation of active chemicals, such as OH-, require breakdown of the liquid phase through a corona streamer with associated electric field strengths in the range of MV/cm,[23] or catalysis by enzymes, metal salts, acids or bases, such as alkali metal hydroxides. Additionally, the time scales for chemical cell lysis is on the order of tens to hundreds of seconds,[10] as compared to the millisecond range of the corona discharge approach used here.

As many lab-on-chip applications require bulk cell lysis and involve non-adherent cells, we repeated the same fluorescence-based experimental procedure, but using a microfluidic chip without any metallic microelectrode and non-adherent K562 cells. In this case, the corona discharge was applied to the cells through the liquid by bringing the corona device close to the inlet (~1 cm) without direct physical contact. Figure 3.6 shows a sketch of the experimental arrangement and a series of images of K562 cells before and after the discharge within a predefined region of interest (ROI) corresponding to a section of the microchannel of around 300 by 500 µm. The bright field image, the strong cAM fluorescence signal, and the missing fluorescence of the PI dye confirmed the viability of all the cells within the ROI. The bottom row of images in Figure 3.6 shows the K562 cells within the ROI after the corona discharge was applied. The noticeable damage to the cells observed in the bright

field image suggests that the cells were lysed. The appearance of the lysed cells is similar to that of cells after applying other lysis methods.[39] Through the strong electric field and associated DEP forces some cells may have been shifted in the images. Lysis has been also confirmed in the fluorescence images. The decrease in the cAM fluorescence signal and the intense fluorescence of the PI confirm that the cells within the ROI were indeed lysed

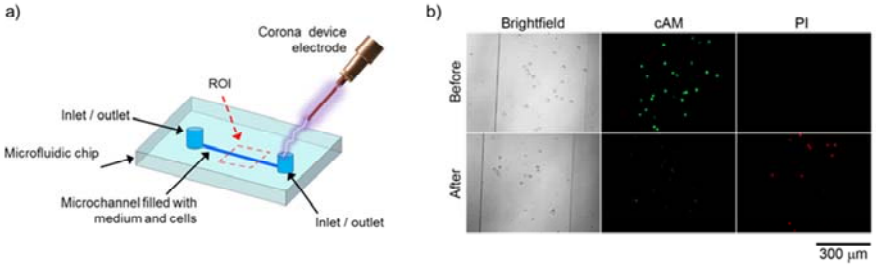

Figure 3.6. Bulk lysis of non-adherent K562 cells. (a) Schematic of the experimental setup used for the experiment. Cells were lysed without the use of a microelectrode by applying the corona discharge to the liquid directly through the inlet of the chip. (b) Cell lysis results. The upper row in the image series shows the bright field, as well as the cAM and PI fluorescence images of viable cells within a region of interest (ROI) of the microchannel before the application of the corona discharge. The bottom row shows the corresponding images of the same ROI after the corona discharge. The damage to the cells after the treatment is evident in the bright field image. The extinction and increase of the fluorescence signals upon using the cAM and PI filters confirms cell lysis within the ROI.

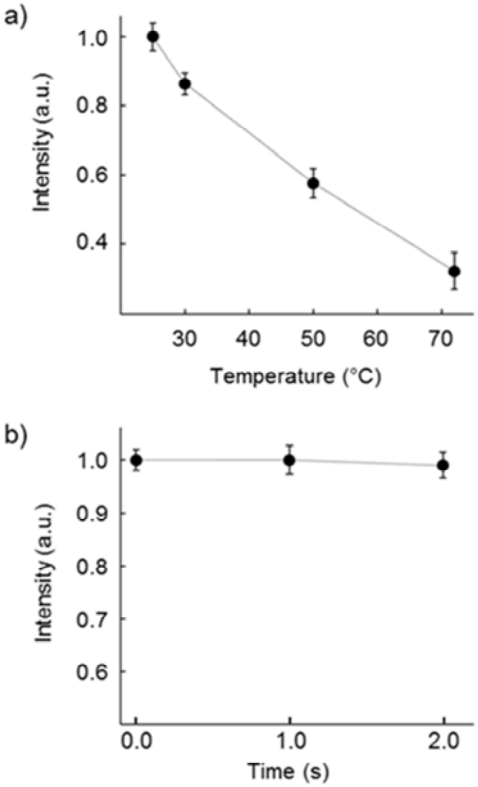

Figure 3.7. Fluorescence intensity plot of the temperature-sensitive dye Rhodamine B. (a) Calibration plot of the fluorescence intensity at different solution temperatures. (b) Fluorescence intensity of the solution during the continuous application of the electric discharge during 2 seconds. Error bars represent the standard deviation (n=5).

This experiment demonstrates that the technique can be used for bulk cell lysis within a microchannel without the need of any electrode. Additionally, these results confirm that the technique is also effective for lysing non-adherent cells.

Heating is always a potential drawback related to the application of electric fields in lab-on-a-chip applications. Thus, to elucidate the

heat characteristics of the corona method, we repeated the lysis experimental procedure using a Rhodamine B solution. The fluorescence intensity of this dye is strongly dependent on temperature and is widely used in microfluidics to determine the temperature of liquids on-chip without the need of invasive thermal sensors.[47,48] Figure 3.7a shows a calibration curve for different temperatures obtained for a chip with Rhodamine B solution. The values of this plot are in agreement with values reported previously by Ross and Locascio,[49] and by Samy et al.[48] Figure 3.7b shows the fluorescence intensity measurements of the same solution and chip versus time upon applying an electric discharge through the corona handheld device. The initial fluorescence intensity value was set to one, and all following measurements were normalized to this initial value. Figure 3.7 evidences that the lysis methodology presented here does bear any risk of significant heating for the conditions and exposure times in the experiments reported here. Additionally, it is worth noticing that no deterioration of the microelectrodes was observed during the experiments (n=5).

3.5 Conclusions

A new method for the lysis of mammalian cells on-chip by using electric discharges from a handheld corona device has been presented. In this method, a thin metal microelectrode is used to deliver an electric discharge of 10 to 30 kV from the corona device to the cells. Lysis of the cells under study was observed through bright-field microscopy and compared with electrical lysis control experiments, which indicated that the disruption of the cell membranes occurred as early as 300 ms after the application of the electric discharge. Fluorescence viability tests using FDA and PI dyes confirmed the lysis of preselected BHK cells. The same experimental procedure was used to lyse eGFP HCT 116 cells, and the results were compared electrical lysis control experiments. In using a combination of filter cubes, fluorescence viability dyes and

fluorescence emission of the cells, the experimental results confirmed the lysis of the HCT cells through electric discharges from the corona device. These findings confirm the results of the previous experiments with BHK cells. Bulk cell lysis of non-adherent B562 cells was also demonstrated by applying the corona discharge directly to the medium, without the use of a microelectrode. All cells within the investigated ROI were lysed as evidenced by bright field and fluorescence microscopy. The corona technique, therefore, can be used to either lyse selected individual cells or cells in a microfluidic chip through the use of a microelectrode, or for bulk lysis of all cells within a microchannel without requiring any electrode or physical interface. The lysis occurred at sub-second timescale which is in strong contrast to most other techniques that require longer time. Additionally, no bubble formation or heating was observed during the experiments, which renders the corona method suitable for many lab-on-a-chip applications that require the lysis of cells. Finally, the used equipment is low-cost and the device operation is simple so that corona-device-based lysis constitutes a viable alternative to electrical and other lysis techniques.

3.6 Acknowledgements

Financial support was provided through Swiss Systems Biology Program “SystemsX.ch” within the RTD-project “CINA”. The authors acknowledge Prateek Singh for providing the HCT116 cells as well as Dr. Sarah Geisler for providing the K562 cells and medium used in this study.

3.7 Supplementary information

3.7.1 Control experiment - electrical lysis

As a control experiment cells were electroporated in a previously reported microsystem.[38] The methods are summarized as follows:

Cells were harvested from culture flasks by trypsinization and re-suspended in isotonic sucrose buffer (adjusted to pH 7.4). For discrimination of live and dead cells the isotonic sucrose buffer was supplemented with the fluorescent live stain calcein AM and the dead stain propidium iodide. The cell suspension was loaded into a 100 uL glass syringe (ILS, Germany). Flow was provided by a syringe pump (nemesys, Cetoni GmbH, Germany) and the cells were injected into a microfluidic chip via a glass capillary (see Supplementary Figure 3.1). The chip was fabricated as a glass - SU-8 - glass sandwich device with facing platinum electrodes. These 18 um wide electrodes at the top and bottom of a channel (40 µm x 40 µm cross section) provided an electrical interface to the cells flowing through the channel. An AC voltage of 8 V amplitude and a frequency of 10 kHz was applied between the electrodes. This electric field was switched on for one single passage of a cell between the electrodes. The chip was placed on top of an inverted fluorescence microscope (DMI 6000, Leica Microsystems, Switzerland), and imaging was performed using a DFC340 camera (Leica Microsystems, Switzerland). For observation of the cells, the flow was inverted and the cell was shuttled back-and-forth for several minutes to allow for assessing the electroporation effects.

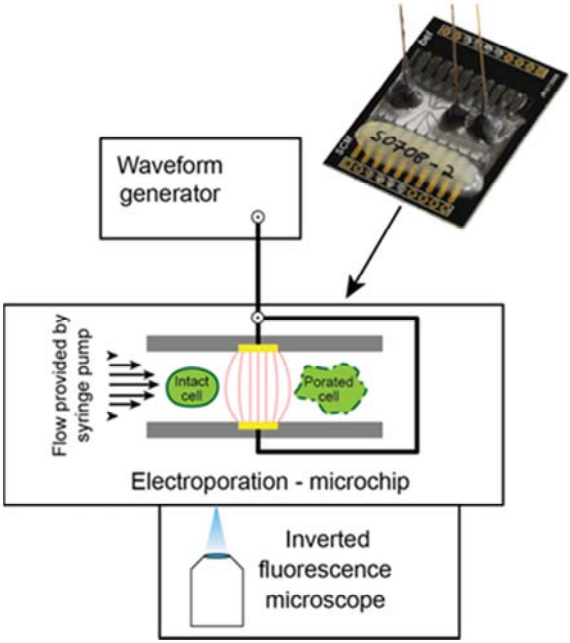

Supplementary Figure 3.1. Schematic representation of the control experiment for conventional electrical lysis in an integrated microfluidic platform.

3.7.2 Dielectrophoretic forces

The DEP forces exerted on a particle with spheroid-like morphology in a fluid is:

$$F_{DEP} = 2\pi R^3 \varepsilon_m Re(f_{CM}) \nabla {E_{RMS}}^2 \quad \text{(S2.1)}$$

where R is the radius of the particle, ε_m is the permittivity of the medium, E_{RMS} is the root-mean-square of the alternating-current external electric field and $Re(f_{CM})$ is the real part of the Clausius-Mossotti (CM) factor depending on the complex permittivity of the particle and the medium, ε_p^* and ε_m^*, as follows:

$$f_{CM} = \left[\frac{\varepsilon_p^* - \varepsilon_m^*}{\varepsilon_p^* + 2\varepsilon_m^*}\right] \quad \text{(S2.2)}$$

As indicated by the literature, the dielectrophoretic properties of mammalian cells generally correspond to one of three different frequency groups. The dominant factor at frequencies under the 10^2 Hz mark is the surface charge of the cell, whereas the dielectric permittivity of the cell rules at frequencies above ~10^3 Hz.[1] Determination of the dielectric properties of mammalian cells can be approached by using a proposed protoplast model by neglecting the conductance of the cell membrane,[2] which leads to a CM factor defined by the following expression for viable cells:[43,50]

$$f_{CM}(\omega) = -\frac{\omega^2(\tau_m\tau_c^* - \tau_c\tau_m^*) + j\omega(\tau_m^* - \tau_m - \tau_c^*) - 1}{\omega^2(2\tau_m\tau_c^* + \tau_c\tau_m^*) - j\omega(\tau_m^* + 2\tau_m + \tau_c^*) - 2} \quad \text{(S2.3)}$$

where $\tau_c^* = c_m R/\sigma_c$ and $\tau_c = \varepsilon_c/\sigma_c$ are time constants, c_m is the cell membrane capacitance, and σ_c and ε_c are the cytoplasm electrical conductivity and permittivity. In previous studies, mammalian cells have shown strong nDEP at low frequencies and strong pDEP at high frequencies. This characteristic difference have enabled sorting of viable and non-viable cells due to their inherent dielectric characteristics.[3] Specifically, for frequencies higher than 10 kHz and less than MHz, experimental studies demonstrate that cells experience strong pDEP within the high electric field region that decays exponentially with distance due to the force dependence on the field gradient.[43,51,52] A schematic representation of the particle (i.e. the cell) under the influence of a DEP force is shown in Supplementary Figure 3.2.

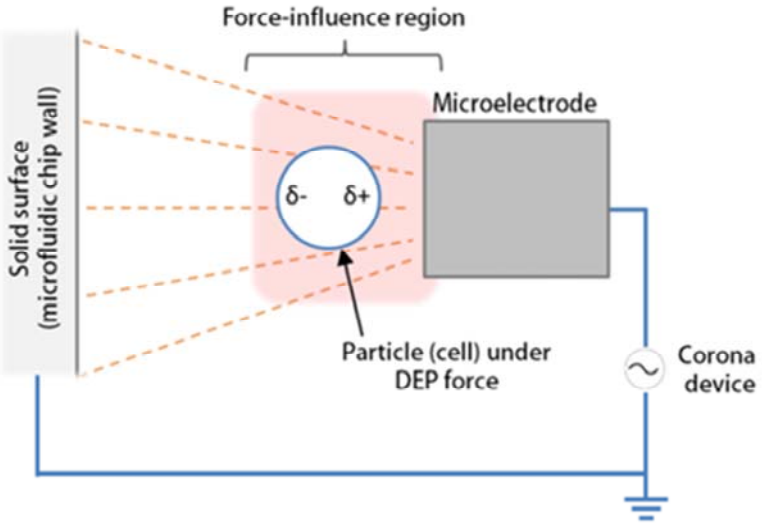

Supplementary Figure 3.2. Schematic representation of a pDEP force acting on a particle, due to an electric discharge from a handheld corona device.

Under the influence of DEP forces, particles, such as cells, may follow different traveling behaviors when they are close to microelectrodes.[45] This traveling behavior depends on the CM factor and travelling motion forces due to induced electrokinetics. Particles may experience both pDEP and motion forces, and the ratio of these defines the regions in which the particle is attracted or repelled. If the real component of the CM factor is dominant, the particle will be attracted to the electrode, but if the real part is small and the imaginary part is dominant, for instance, the particle may exhibit an apparent erratic motion along the edges of the electrode. This means, as explained by Hughes,[45] that the attracting forces and the motion forces are of similar magnitude (i.e. $|Im[f_{CM}(\omega)]| > 4Re[f_{CM}(\omega)]\ and\ Re[f_{CM}(\omega)] > 0$) then the net force depends on whichever force prevails due to, for instance, local electric field gradients. The effect of the force is spatially variable and, at shorter

distances, pDEP may dominate. The particle, or cell, may also experience some motion even within a region close to the microelectrode. The strength of the force, however, decays with distance and cells at a certain distance from the electrode may actually be pushed away due to other forces (e.g. electro-hydrodynamic), also observed in the experiments in this study. The direction of the resulting force vector in DEP is characterized by a cross-over frequency. Experimental studies have demonstrated that viable cells may experience a transition from nDEP to pDEP, and *vice versa*, depending on the combination of the real and the imaginary components of the CM factor.[53] It is important to note that the complete picture involves a more complex electro-hydrodynamic scenario with additional hydrodynamic and electrothermal-induced forces occurring in the bulk liquid. Our experimental observations, however, agree well with the study reported by Menachery et al. and confirm that cells experience a pDEP force past the crossover frequency. Supplementary Figure 3.3 shows that this field region lies within ~10 microns from the microelectrode, which is a length scale comparable to the size of one cell. For this reason, the cells within this region are strongly influenced by the DEP force, while the cells in the more distant regions experience a combination of forces including, for instance, hydrodynamic effects.[30,54] Only the cells in the vicinity of the electrode get strongly attracted, experience the high electric field and get lysed: the force decays by about 3 orders of magnitude within a distance of ~30 microns.

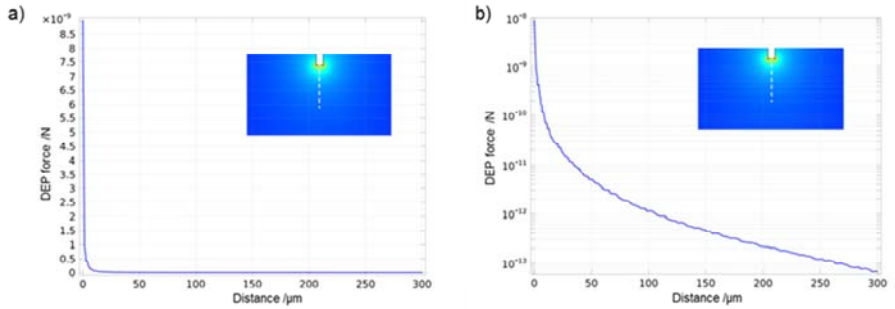

Supplementary Figure 3.3. Dielectrophoretic (DEP) force results from FEA simulations in a) normal and b) semi-logarithmic scale. The forces are plotted along the dashed line shown in the Figure inset as a function of distance from the electrode. The inset shows the electric field results of the same simulation in color code.

3.7.3 Finite element model simulation

The simulations were performed using the Microfluidics, Particle Tracing and Electric Currents modules in COMSOL Multiphysics 5.0 software. The simulations rely on a 2D model of the 20-micron-width microelectrode integrated into the microfluidic chamber. The mesh of the geometry was formed by free-triangular elements with extra-fine refinement at the interface between the electrode and the medium (i.e., the dielectric). The minimum element quality of the mesh was 0.8 as observed in Supplementary Figure 3.4. If not otherwise stated, water standard values were used for the density and dynamic viscosity of the medium, while the conductivity was set to 87 mS/cm. The electric current component of the model included the simulation of a 4.5 MHz AC electric field using the frequency domain feature in the electric current module. Creeping flow was used for the microfluidic component of the simulation, setting no-slip conditions at all boundaries. The dielectrophoretic (DEP) force was simulated using the Shell feature of the Particle Tracing module, assuming a thin-shell cell model. The parameters used for the shell model are: cell density 1050 kg/m^3, cell diameter 10 μm, cell

conductivity 0.25 S/m, shell electrical conductivity 10^{-6} S/m, shell relative permittivity 20, shell thickness 8 nm, particle density 1050 kg/m^3, medium viscosity 10^{-3} Pa*s and medium density 10^3 kg/m^3.

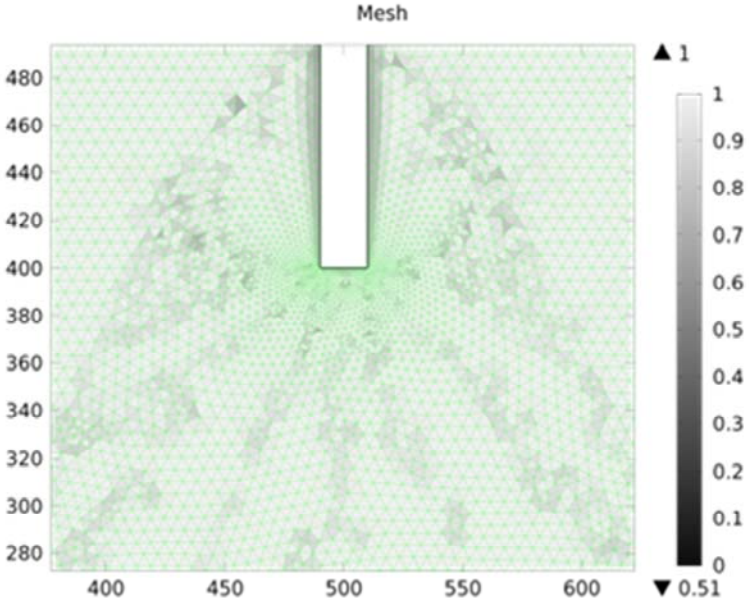

Supplementary Figure 3.4. Mesh quality image of the FEA.

3.8 Bibliography

1 Figeys and Pinto, *Anal. Chem.*, 2000, **72**, 330A–335A.

2 A. R. Wheeler, W. R. Throndset, R. J. Whelan, A. M. Leach, R. N. Zare, Y. H. Liao, K. Farrell, I. D. Manger and A. Daridon, *Anal. Chem.*, 2003, **75**, 3581–3586.

3 Y. Lin, R. Trouillon, G. Safina and A. G. Ewing, *Anal. Chem.*, 2011, **83**, 4369–4392.

4 R. B. Brown and J. Audet, *J. R. Soc. Interface*, 2008, **5 Suppl 2**, S131–8.

5 J. Gao, X.-F. Yin and Z.-L. Fang, *Lab Chip*, 2004, **4**, 47–52.

6 J. El-Ali, P. K. Sorger and K. F. Jensen, *Nature*, 2006, **442**, 403–11.

7 W. Wan and J. T. W. Yeow, *Biomed. Microdevices*, 2011, **13**, 527–532.

8 J. Kim, J. W. Hong, D. P. Kim, J. H. Shin and I. Park, *Lab Chip*, 2012, **12**, 2914–21.

9 J.-Y. Kim, D. A. Fluri, R. Marchan, K. Boonen, S. Mohanty, P. Singh, S. Hammad, B. Landuyt, J. G. Hengstler, J. M. Kelm, A. Hierlemann and O. Frey, *J. Biotechnol.*, 2015, **205**, 24–35.

10 D. Di Carlo, C. Ionescu-Zanetti, Y. Zhang, P. Hung and L. P. Lee, *Lab Chip*, 2005, **5**, 171–8.

11 L. Nan, Z. Jiang and X. Wei, *Lab Chip*, 2014, **14**, 1060–73.

12 P. a Quinto-Su, H.-H. Lai, H. H. Yoon, C. E. Sims, N. L. Allbritton and V. Venugopalan, *Lab Chip*, 2008, **8**, 408–14.

13 E. Zeira, A. Manevitch, A. Khatchatouriants, O. Pappo, E. Hyam, M. Darash-Yahana, E. Tavor, A. Honigman, A. Lewis and E. Galun, *Mol. Ther.*, 2003, **8**, 342–50.

14 T. Y. Tsong, *Biophys. J.*, 1991, **60**, 297–306.

15 S.-W. Lee and Y.-C. Tai, *Sensors Actuators A Phys.*, 1999, **73**, 74–79.

16 T. Nakayama, M. Namura, K. V Tabata, H. Noji and R. Yokokawa, *Lab Chip*, 2009, **9**, 3567–73.

17 T. Geng, N. Bao, N. Sriranganathanw, L. Li and C. Lu, *Anal. Chem.*, 2012, **84**, 9632–9.

18 M. Khine, A. Lau, C. Ionescu-Zanetti, J. Seo and L. P. Lee, *Lab Chip*, 2005, **5**, 38–43.

19 C. Martino, M. Zagnoni, M. E. Sandison, M. Chanasakulniyom, A. R. Pitt and J. M. Cooper, *Anal. Chem.*, 2011, **83**, 5361–8.

20 S. Wang, X. Zhang, W. Wang and L. J. Lee, *Anal. Chem.*, 2009, **81**, 4414–21.

21 R. Ziv, Y. Steinhardt, G. Pelled, D. Gazit and B. Rubinsky,

Biomed. Microdevices, 2009, **11**, 95–101.

22 A. A. Joshi, B. R. Locke, P. Arce and W. C. Finney, *J. Hazard. Mater.*, 1995, **41**, 3–30.

23 D. Staack, A. Fridman, A. Gutsol, Y. Gogotsi and G. Friedman, *Angew. Chem. Int. Ed. Engl.*, 2008, **47**, 8020–4.

24 M. M. Sein, Z. Bin Nasir, U. Telgheder and T. C. Schmidt, *J. Phys. D. Appl. Phys.*, 2012, **45**, 225203.

25 B. R. Locke, M. Sato, P. Sunka, M. R. Hoffmann and J.-S. Chang, *Ind. Eng. Chem. Res.*, 2006, **45**, 882–905.

26 S. Thorslund and F. Nikolajeff, *J. Micromechanics Microengineering*, 2007, **17**, N16–N21.

27 P. Seimandi, G. Dufour and F. Rogier, *Math. Comput. Model.*, 2009, **50**, 574–583.

28 R. Morrow, *J. Phys. D. Appl. Phys.*, 1997, **30**, 3099–3114.

29 C. Escobedo and D. Sinton, *Microfluid. Nanofluidics*, 2011, 653–662.

30 L. Y. Yeo, J. R. Friend and D. R. Arifin, *Appl. Phys. Lett.*, 2006, **89**, 103516.

31 A. Starikovskiy, Y. Yang, Y. I. Cho and A. Fridman, *Plasma Sources Sci. Technol.*, 2011, **20**, 024003.

32 A. Denat, *IEEE Trans. Dielectr. Electr. Insul.*, 2006, **13**, 518–525.

33 K. Schoenbach, J. Kolb, S. Xiao, S. Katsuki, Y. Minamitani and R. Joshi, *Plasma Sources Sci. Technol.*, 2008, **17**, 024010.

34 P. Hoffer, 2014.

35 P. Bruggeman and C. Leys, *J. Phys. D. Appl. Phys.*, 2009, **42**, 053001.

36 J. C. McDonald, D. C. Duffy, J. R. Anderson, D. T. Chiu, H. Wu, O. J. Schueller and G. M. Whitesides, *Electrophoresis*, 2000, **21**, 27–40.

37 L. Nan, Z. Jiang and X. Wei, *Lab Chip*, 2014, **14**, 1060–73.

38 S. C. Bürgel, C. Escobedo, N. Haandbæk and A. Hierlemann, *Sensors Actuators B Chem.*, 2015, **210**, 82–90.

39 H. Lu, M. a Schmidt and K. F. Jensen, *Lab Chip*, 2005, **5**, 23–29.

40 M. Poudineh, R. M. Mohamadi, A. Sage, L. Mahmoudian, E. H. Sargent and S. O. Kelley, *Lab Chip*, 2014, **14**, 1785–90.

41 V. L. Sukhorukov, H. Mussauer and U. Zimmermann, *J. Membr. Biol.*, 1998, **163**, 235–245.

42 V. L. Sukhorukov, H. Mussauer and U. Zimmermann, *J. Membr. Biol.*, 1998, **163**, 235–45.

43 C. P. Jen and T. W. Chen, *Biomed. Microdevices*, 2009, **11**, 597–607.

44 S.-S. Yun, S. Y. Yoon, M.-K. Song, S.-H. Im, S. Kim, J.-H. Lee and S. Yang, *Lab Chip*, 2010, **10**, 1442–1446.

45 M. P. Hughes, *Nanoelectromechanics in Engineering and Biology*, 1st Editio., 2002.

46 J. T. Nevill, R. Cooper, M. Dueck, D. N. Breslauer and L. P. Lee, *Lab Chip*, 2007, **7**, 1689–95.

47 T. Glawdel, Z. Almutairi, S. Wang and C. Ren, *Lab Chip*, 2009, **9**, 171–4.

48 R. Samy, T. Glawdel and C. L. Ren, *Anal. Chem.*, 2008, **80**, 369–75.

49 D. Ross and L. E. Locascio, *Anal. Chem.*, 2002, **74**, 2556–64.

50 T. B. Jones, *Electromechanics of Particles*, Cambridge University Press, Cambridge, 1995.

51 C.-P. Jen and H.-H. Chang, *Biomicrofluidics*, 2011, **5**, 34101–3410110.

52 D. S. Gray, J. L. Tan, J. Voldman and C. S. Chen, *Biosens. Bioelectron.*, 2004, **19**, 771–80.

53 A. Menachery, C. Kremer, P. E. Wong, A. Carlsson, S. L.

Neale, M. P. Barrett and J. M. Cooper, *Sci. Rep.*, 2012, **2**, 775.

54 J. A. Wood, B. Zhang, M. R. Tomkins and A. Docoslis, *Microfluid. Nanofluidics*, 2007, **3**, 547–560.

4 AUTOMATED, MULTIPLEXED ELECTRICAL IMPEDANCE SPECTROSCOPY PLATFORM FOR CONTINUOUS MONITORING OF MICROTISSUE SPHEROIDS

Sebastian C. Bürgel, Laurin Diener, Olivier Frey, Jin-Young Kim, and Andreas Hierlemann

Submitted to Analytical Chemistry

4.1 Abstract

Microtissue spheroids in microfluidic devices are increasingly used to establish novel *in vitro* organ models of the human body. As the spheroids are comparably sizeable, it is difficult to monitor larger numbers of them by optical means. Therefore, electrical impedance spectroscopy (EIS) emerges as a viable alternative to probing spheroid properties. Current spheroid EIS systems are, however, not suitable for investigating multiple spheroids in parallel over extended time in an automated fashion. Here we address this issue by presenting an automated, multiplexed EIS (AMEIS) platform for impedance analysis in a microfluidic setting. The system was used to continuously monitor the effect of the anti-cancer drug Fluorouracil (5-FU) on HCT116 cancer spheroids. Simultaneous EIS monitoring of up to 15 spheroids was performed in parallel over four days at a temporal resolution of two minutes without any need for pumps or any interference with the setup. A baseline normalization method to improve robustness and to reduce the influence of slow changes in the medium conductivity on the spheroid EIS readings has been developed and validated by experiments and means of a finite-element model. The same method and platform was then used for on-line monitoring of cardiac spheroids. The beating frequency of each cardiac spheroid could be read out in a completely automated fashion. The developed system constitutes a promising method for simultaneously evaluating drug impact and/or toxic effects on multiple microtissue spheroids.

4.2 Introduction

Three-dimensional (3D) microtissue spheroids are emerging as a novel tool for better predicting drug effects, since they more closely mimic an *in vivo* environment as opposed to conventional two dimensional cell layers.[1–3] Flat cell cultures cannot sufficiently mimic the cell-to-cell or cell-extracellular matrix interactions found in *in vivo*

systems, and the cells often lose fundamental properties when taken out of their natural environment.[4] Spheroids can be reproducibly fabricated and different types of spheroids can be handled and used with existing industrial liquid handling systems. The combination of 3D organotypic microtissues with microfluidic devices holds great potential for developing novel *in vitro* methods for drug screening and toxicology assays. The fluidic interconnection of several different organotypic microtissues on a chip gave rise to developments towards body-on-a-chip platforms.[5–7]

The 3D spheroid systems, however, require new readout techniques, as common readout assays for 2D cell cultures are largely incompatible with the 3D systems. Spheroids with typical diameters of at least 200 µm are difficult to analyze optically in their entirety, even with confocal microscopy, due to the large number of cells and overall volume. Further, advanced imaging methods that feature a large field of view and a large depth of focus in order to assess an entire spheroid are typically not scalable for parallel *in situ* analysis of many spheroids. Ideally, the new readout methods should not interfere with the experiment and should be continuously applicable in an incubator environment on many samples in parallel in an automated fashion. The beating rates of cardiac spheroids are, for example, very sensitive to temperature changes, so that any transfer for analysis will produce artifacts.[8]

Electrical impedance spectroscopy (EIS) receives growing interest as an alternative method to probe the properties of spheroids. EIS for spheroid analysis is based on applying an AC voltage to a set of microelectrodes and reading out the resulting current to calculate the corresponding inter-electrode impedance values. The characteristic impedance of the microtissue can be measured and analyzed by placing the spheroid between the electrodes. EIS has been previously used, e.g., for the analysis of bacteria,[9] micro-particles,[10] single yeast cells[11], and various blood cell types.[12]

Different systems have been presented to date for EIS analysis of spheroids. Apoptosis or tissue necrosis in breast carcinoma spheroids upon drug exposure have been analyzed by using a capillary screening system.[13] Next, a chip featuring microwells with electrodes located at the side walls for EIS measurements has been used.[14] Spheroids were sequentially loaded into and removed from the measurement cavity by means of a micromanipulator and analyzed at selected time points. Another spheroid EIS chip relied on high-aspect-ratio SU-8 structures within a poly(dimethylsiloxane) (PDMS) channel to trap a spheroid between a set of facing and interdigitated electrodes.[15] It was shown that the EIS measurements could be used to discriminate different dilutions of medium and various spheroid sizes.

The EIS platforms for spheroids mentioned above have a number of limitations for drug testing or toxicity assays. Typically, drug candidates have to be studied on longer time scales (several days), and different compounds have to be analyzed in parallel. Therefore, a system is required which enables (i) continuous recordings over several days, (ii) parallelized readout of multiple tissues, cultured under different conditions, and (iii) automated operation without the need of operator interference with the setup to perform measurements.

Here, we present an automated multiplexed EIS (AMEIS) prototype platform, which is meeting the three requirements outlined above. The integrated platform is targeted at culturing and performing EIS measurements of multiple microtissue spheroids. The device can autonomously acquire impedance spectra of up to 15 individual spheroids over multiple days without the need for interfering with the setup. While the current system has been demonstrated for 15 microtissues in parallel, the architecture and operation of the microsystem, the readout electronics, and the controlling and analysis software were designed to be scalable.

Furthermore, beating cardiac spheroids are particularly sensitive to environmental changes, as, for example, removing them from an incubator for microscopic evaluation can induce temperature changes, which then significantly influence the beating rate.[8] Microscopic evaluation would significantly limit throughput, as the extraction of the beating rate requires video recordings of several seconds per spheroid, a procedure that is typically not suitable for parallelization. Therefore, providing an automated, non-invasive and label-free *in situ* assessment method for multiple cardiac spheroids in parallel, which is compatible with a conventional incubator environment is desirable.

4.3 Materials and methods

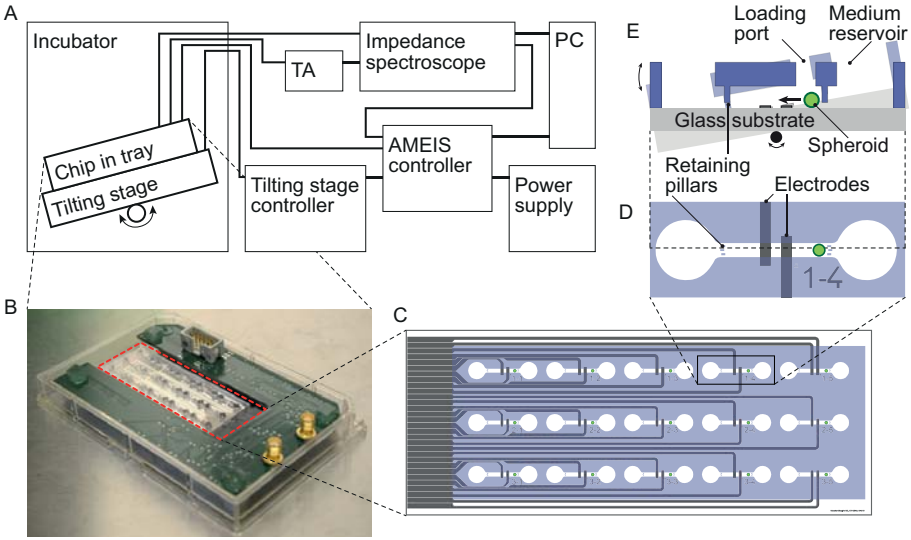

Figure 4.1. Overview of the AMEIS platform. A: schematics of the entire system (TA: trans-impedance amplifier); B: chip (highlighted in dashed red line) and switch-board placed in omni-tray; C: schematic of the chip with 15 separate chambers featuring gray electrodes and blue PDMS structures; D: close-up of one chamber with reservoirs on the left and right. The spheroid movement in the central channel was confined by retaining pillars on both sides of the channel, the coplanar EIS electrode set was arranged centrally in the channel. E: schematic side view showing the medium reservoir and spheroid loading port, as well as the tilting-induced motion of the spheroid over the electrodes.

4.3.1 Setup

The EIS recordings were conducted during multiple days and, therefore, had to be carried out in a standard incubator environment at 37 °C, 5% CO_2 and 95% relative humidity. As schematically shown in Figure 4.1A, the chip and the supporting printed circuit board (PCB, AMEIS switch board) were placed in an omni-tray and affixed on a tilting stage. The chip fabrication was based on standard soft-lithography and Pt microelectrodes patterning by lift-off as outlined in the supporting information. The AMEIS switch board, shown in Figure 4.1B, multiplexed the analog EIS input/output to any of the 15 chambers and automatically switched from one chamber to another. It featured multiple integrated circuits (IC) for switching, an edge-card connector for electrical interfacing and easy exchange of microfluidic chips, a flat-ribbon connector to the controller board outside the incubator, as well as the two analog SMA connectors connecting to the impedance spectroscope input and output via shielded coaxial cables (see Supplementary Figure 4.2 for a view of the PCB back side). The AMEIS switch board was placed inside a standard omni-tray and closed with an environmental lid (LLS-0310, Labcyte Europe, Dublin, Ireland) soaked with PBS. Some modifications were made: Access holes for the cables were drilled into the lid and sealed with tape before UV sterilization to minimize the openings of the plate. This approach allowed for maintaining

maximal humidity around the chip and limited the evaporation of medium. Impedance measurements were performed with a HF2 impedance spectroscope (Zurich Instruments AG, Zurich, Switzerland) in a frequency range between 10 kHz and 2 MHz, further details can be found in the supporting information.

Both, the AMEIS switch board and the tilting stage had control units outside the incubator. The connecting cables were fed through a hole in the back wall or through the door of the incubator. The AMEIS controller board outside the incubator comprised of a custom-made PCB and an Arduino (Arduino Uno R3, Arduino LLC, www.arduino.cc) for interfacing to a PC and generating the digital control signals that were required to switch from one spheroid chamber to another. The Arduino was also keeping track of the currently active spheroid chamber, the identification of which was sent to the impedance spectroscope and recorded along with the EIS data. This procedure simplified subsequent data-analysis: it provided the necessary information of which chamber has been recorded at what times. The control software on the PC was a custom C# program, which performed the following four primary tasks: (1) read configurations of the PCB and chip layout, (2) continuous switching through all chambers hosting spheroids in a cyclic fashion, (3) create digital signals for the switch board and tilting controller, and (4) transfer of all these data to the Arduino on the AMEIS controller board. Data were recorded on a PC for later off-line analysis.

4.3.2 Chip loading

Before use, the chip was sterilized for at least 30 minutes by UV light in a sterile bench. Afterwards, standard medium was introduced into each chamber via the loading ports. Spheroids were prepared as outlined in the supporting information and then extracted from the U-bottom 96-well plate by a pipette using a 200-µL tip and injected into

the chip. During the loading procedure, the chip was manually tilted at least once per minute to prevent any adhesion of the tissues to the channel walls and channel bottom. For control experiments, we used polystyrene beads of 200 µm and 500 µm diameter (SLGMS-2.5 212-250µm - 10g and PMMAMS-1.2 425-500µm - 5g, Cospheric LLC, Santa Barbara, CA, USA).

4.3.3 Data analysis

After the experiment was finished, the recorded data were analyzed by a custom Matlab tool. The data of all chambers were recorded sequentially and processed in chunks of one chamber at a time. The following steps were performed for each single recording cycle of each chamber: (1) extract baseline current at all simultaneously recorded six frequencies; (2) find peak position using the frequency with the largest baseline current (typically 653 kHz); since the peak is w-shaped, the smaller of the two minima has been used to gain reproducible values over multiple tilting cycles; (3) extract peak-to-baseline currents (ΔI) at all six frequencies using the previously obtained peak position; (4) calculate normalized peak-to-baseline current values (ΔI_{norm}) by dividing the ΔI value by the corresponding baseline value; (5) store baseline, ΔI and ΔI_{norm} for each of the six frequencies along with timestamp and chamber index for plotting of spectra or data sequences over multiple days.

4.4 Results and discussion

4.4.1 Time domain analysis

The platform presented in Figure 4.1 was designed to record EIS data of multiple spheroids over extended periods of time. The spheroid cultivation and measurement relied on periodically tilting the entire platform at defined times. Tilting induced a difference in

hydrostatic pressures between the two connected medium reservoirs (cf. Figure 4.1E). The medium was consequently flowing from the higher-level reservoir through the channel containing the spheroid into the lower-level reservoir. The spheroid was moved over the electrode set to the lower end of the microchannel by gravity and liquid drag forces of the medium flow. Repeated back-and-forth tilting of the platform served three goals: (1) medium perfusion of the spheroid without use of tubings and pumps, (2) prevention of adhesion of the spheroid to the channel surfaces without any need for surface treatment, and (3) back-and-forth shuttling of the spheroid over the set of EIS measurement electrodes at defined times to perform dynamic round-robin EIS recordings.

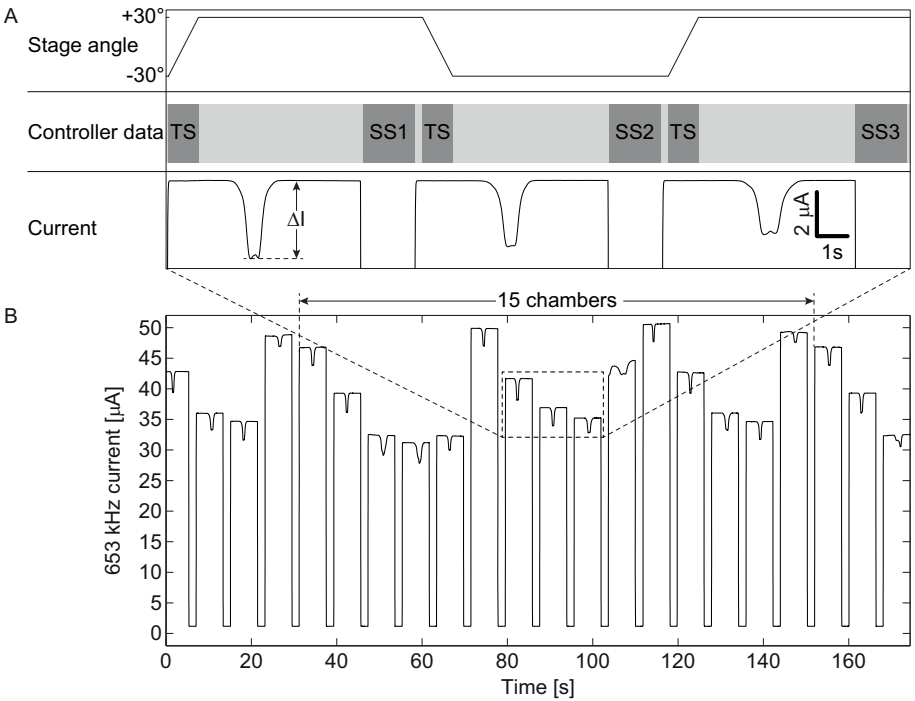

Figure 4.2. Measurement principle in the time-domain. A: Temporal sequence of stage tilting, controller signals (switching sequences, indicated as SS, and tilting sequence, indicated as TS) and corresponding current dips caused by spheroids moving over the electrodes; B: Raw current signals of an entire measurement cycle of all 15 chambers measured at 653 kHz. ΔI denotes peak-to-baseline signal heights.

Tilting the platform and switching the EIS recording from one chamber to another was achieved via an Arduino-based AMEIS controller board in an automated fashion: As schematically shown in Figure 4.2A the stage, which holds the microchip was tilted in periodic intervals (top row). The tilting caused a movement of the spheroid over the electrodes, which yielded a characteristic spike in the current (bottom row). EIS recordings were interrupted, while the AMEIS controller board was sending a switch control signal to the AMEIS switch board holding the microchip. Upon receiving the entire switch sequence (indicated as SS1, SS2, SS3 in the center row), the EIS signal was recorded from the next chamber. The controller board was then sending a tilt signal (indicated as TS) to the tilting stage controller in order to initiate the next tilting step of the stage. In this way, the single analog input and output of the impedance spectroscope were sequentially multiplexed to each of the 15 chambers in an automated cyclic fashion for multi-day EIS recordings.

Whenever a spheroid was passing over the electrode set, it changed the impedance between the two electrodes. To measure the impedance, an impedance spectroscope was used to apply AC voltages of different frequencies and constant amplitudes of 200 mV between a set of coplanar electrodes. The resulting currents were measured via the external trans-impedance amplifier. The output voltage of this amplifier was fed back to the impedance spectroscope. The recorded current depicted in Figure 4.2A and Figure 4.2B as well as the results from finite the finite element model in Supplementary Figure 4.6 show a characteristic w-shaped dip,

when a spheroid was moving over the electrodes. Since the cell membranes were less conductive than the surrounding medium,[16–18] the presence of the spheroid increased the inter-electrode impedance and reduced the recorded current. The level of the baseline before and after the passage of the spheroid depends on the electrical properties of the medium, the electrodes and interfaces. Peak-to-baseline currents (ΔI, as indicated in Figure 4.2A) were automatically extracted for every measurement point recorded in every chamber and later analyzed for multi-day monitoring (Figure 4.3). Since parasitics and medium compositions varied from chamber to chamber, the baseline current of each chamber was different, as can be seen in Figure 4.2B. Switching between chambers every 8 seconds yielded a temporal resolution of 2 minutes for a measurement cycle including all 15 chambers. The tilt-and-switch concept thus enabled medium perfusion and shuttling of the spheroid over the EIS electrode set for sequential evaluation of multiple tissues and different electrode sites.

Additionally, rolling the spheroid over the electrode pair is advantageous in comparison to immobilizing it on an electrode: While a drift or change in the medium composition will be included in an impedance measurement of an immobilized spheroid and cannot necessarily be differentiated from changes of the spheroid itself, any change in the impedance signal of a rolling spheroid can be readily separated from a change in the baseline impedance of the medium.

Frequent tilting of the chamber can further be used as a strategy to prevent adhesion of spheroids to the channel walls and channel bottom. In an experiment, shown in Supplementary Figure 4.3, the tilting interval of the measurement platform was logarithmically varied from 15 s to 170 min. For tilting intervals below 20 min, all 15 spheroids were moving over the electrodes, yielding an impedance signal as shown in Figure 4.2B. For increasing tilting intervals beyond 20 min, more and more tissues were adhering to the channel walls. For the largest interval of 170 min only 3 of 15

spheroids (20%) were still moving. Even longer tilting intervals could not be evaluated, as the spheroids started to dissociate. This dissociation was most likely caused by insufficient nutrient supply in the stagnant medium: nutrient diffusion from the reservoir through the microchannel is slow, and the medium volume surrounding the spheroid in the confined microchannel is very limited.

4.4.2 Frequency domain analysis

Further insights into the electrical properties of medium and spheroids were gained by multi-frequency recordings. The current spectra in Supplementary Figure 4.4A were obtained by evaluating the baseline currents as shown in Figure 4.2 for each of the six recorded frequencies. Thus, the fifth magnitude value from the left (653 kHz) of the baseline spectrum in Supplementary Figure 4.4A corresponds to the baseline value of one chamber observed in the time-domain in Figure 4.2. At frequencies below 100 kHz, the magnitude increased with increasing frequencies. This is due to the electric double layer at the electrode-liquid interface, which shows capacitive behavior and, therefore, entails lower impedance – and higher currents – for increasing frequencies. For frequencies larger than 1 MHz, the magnitude decreased due to coupling losses.

Despite using humidifier pads below and above the chip and placing the setup in a maximum-humidity incubator, slight evaporation of medium was observed. This was evidenced in the EIS measurements by increasing baseline currents across the spectrum in Supplementary Figure 4.4A over the course of two days. Over time, the current increased across all frequencies, since the evaporating water led to an up-concentration of salts. Thus, the conductivity of the medium increased, yielding higher currents between the electrodes. Exchanging the medium after two days led to initially decreased currents, which later again increased due to evaporation.

The peak-to-baseline current spectrum in Supplementary Figure 4.4B was obtained by subtracting the baseline current from the dip minimum (cf. Figure 4.2) at each frequency. This spectrum reflects the characteristic properties of the spheroid. The decreasing peak-to-baseline currents (increasing absolute values) over time at all frequencies suggest a growth of the spheroid. An increasing size of a spheroid led to increasing inter-electrode impedance and, thus, increasing peak-to-baseline values at all frequencies. Any subsequent single-frequency analysis was carried out at the frequency with the highest absolute ΔI values of 81 kHz. Growth of the spheroid was monitored optically at selected time-points as shown in Supplementary Figure 4.4C. The optically observed growth of the spheroid from a diameter of 370 µm (day 0) to 470 µm (day 2) and 590 µm (day 4) confirm the continuously acquired data by EIS.

The importance of dynamic instead of static EIS recordings can be seen in Supplementary Figure 4.4A and B: The change in baseline magnitude due to evaporation over time (20 µA over 1 d at 653 kHz, cf. Supplementary Figure 4.4A) was significant compared to the changes in the peak-to-baseline magnitudes due to spheroid growth (4 µA over 1 d at 653 kHz, cf. Supplementary Figure 4.4B). This was despite all efforts to reduce evaporation including a maximum-humidity incubator and the use of humidifier pads. Precise measurements of slow spheroid growth without monitoring the medium conditions are thus not possible. While monitoring medium properties via a separate set of electrodes is possible, the use of the very same integrated electrode set is preferable, as the interpretation of results is straightforward due to a lower number of parasitic elements and no difference in drift behavior. Decoupling the measurements of medium and spheroid impedance may also enable the dosing of compounds while monitoring their concentration.

4.4.3 Continuous measurements

The presented platform allows for continuous multi-day EIS measurements of up to 15 spheroids. The electrically and fluidically separated chambers (cf. Figure 4.1D) contained one spheroid each. For every activation of the electrodes and tilting of the platform, the impedance spectrum at multiple frequencies was recorded. The impedance measurement time of one chamber was set to 8 s, so that one measurement cycle of all 15 chambers took 2 minutes. This was deemed sufficient, as the time-scales of spheroid growth, death or of physiological changes are typically on the order of hours or days.[19] 81 kHz peak-to-baseline currents ΔI recorded from one spheroid over 4 days are shown in Figure 4.3A. As in Supplementary Figure 4.4B, the peak-to-baseline currents decreased due to growth of the tissue. Rotation and position differences of the spheroid during the impedance measurements led to slight variations in the peak-to-baseline current values of subsequent measurements, as can be seen looking at the individual data points in Figure 4.3A.

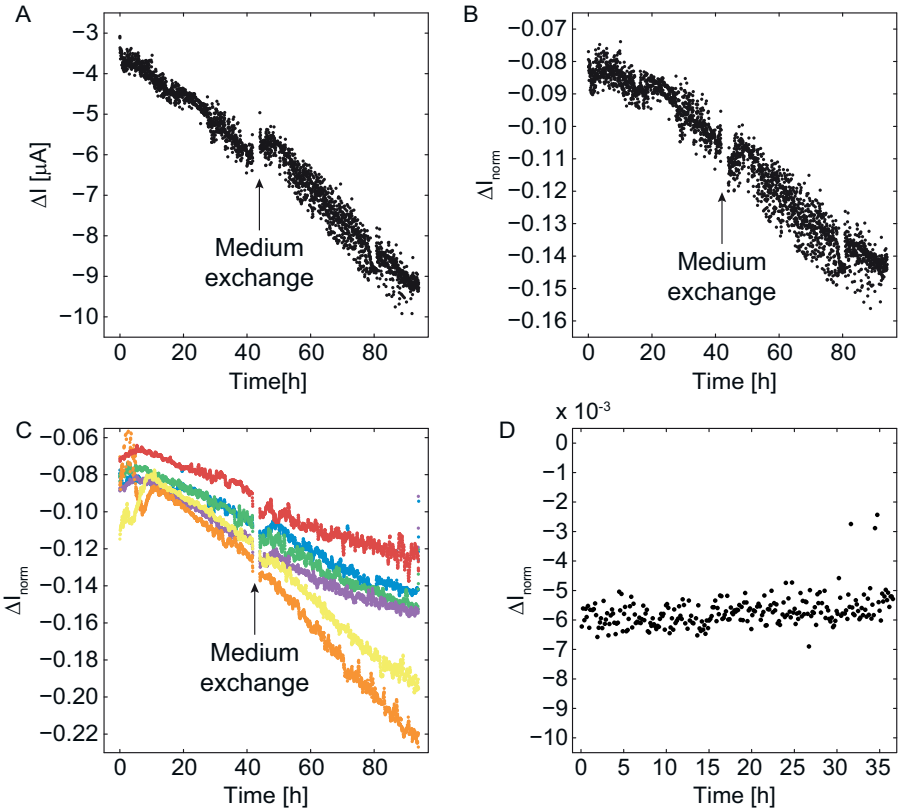

Figure 4.3. Current-versus-time curves for growing cancer spheroids (A-C) and a pancreatic microislet, which was not expected to grow in D. A: Continuous recordings during 90 hours show a noticeable discontinuity upon medium exchange after 42 h in the peak-to-baseline (ΔI) current at 81 kHz. B: The same data have been normalized with the corresponding baseline currents, so that a growth curve without discontinuity upon medium exchange results. C: Normalized ΔI_{norm} currents of six exemplary cancer spheroids after applying a moving-average method including ten subsequent measurement values. D: ΔI_{norm} for a pancreatic microislet, which expectedly does not grow. In contrast to the cancer spheroids, there are no large variations or a current decrease. The significantly smaller values in D compared to C are a consequence of the smaller size of the microislet (150 μm diameter).

4.4.4 Baseline drift compensation

The medium-exchange after 42 h led to a significant kink in the peak-to-baseline current plot in Figure 4.3A. This can be explained by a slow change in medium conductivity due to evaporation. As evaporation can be quantified by the shift of the baseline (Supplementary Figure 4.4A), the data were normalized (divided) by the corresponding baseline current values to yield the normalized peak-to-baseline currents (ΔI_{norm}) in Figure 4.3B. These normalized ΔI_{norm} data do not show decreasing values or a kink upon medium exchange, since the influence of changes in medium conductivity was eliminated by the normalization. The continuous decrease of the normalized peak-to-baseline signal was observed for all growing cancer spheroids. Exemplary 4-day recordings of six cancer spheroids shown in Figure 4.3C were smoothed by a moving-average method including ten subsequent measurement values for better visualization. All cancer spheroids in Figure 4.3C were growing so that ΔI_{norm} decreased over time. The different growth rates, reflected by different slopes in ΔI_{norm}, can be attributed to differences in initial tissue size and, hence, in the number of growing cells. A control experiment using a non-growing pancreatic microislet is shown in Figure 4.3D: ΔI_{norm} did not change significantly over the course of 36 h, which also demonstrates the stability of the setup and measurements. Since microislets are much smaller (~150 µm diameter) than the cancer spheroids used here (300-600 µm diameter), the ΔI_{norm} values in Figure 4.3D are considerably smaller than those in Figure 4.3B and C. These measurements show the robustness of the method even for small spheroids, which only cover a fraction of the measurement volume (500 µm x 700 µm x 580 µm). A second control experiment shown in Supplementary Figure 4.5 was performed with beads of diameters between 200 µm and 500 µm. It shows the stability of the signals for measurements over four days with relative variations in impedance values of below 10% for all bead sizes. This suggests that slight variations in media

salinity due to evaporation do not lead to significant changes in ΔI_{norm}. As previously reported[10,11], the impedance signals scaled with the size of the beads.

The validity of baseline normalization as a means for decoupling the ΔI_{norm} values from media conductivity was further supported by a finite-element model shown in Supplementary Figure 4.6. The model in Supplementary Figure 4.6A comprises a 2D representation of the microchannel with two electrodes at the bottom and a non-conductive spherical particle in the channel. Simulated values for baseline current and peak-to-baseline current were obtained by calculating the current density at the electrode surface for different positions of the spherical particle. The position of the spheroid for the current minimum was obtained by sweeping the spheroid position axially along the channel as shown in Supplementary Figure 4.6B. That position was then used to calculate the minimal current between the electrode set. The simulation also showed that the two minima in the measured time-domain current in Figure 4.2A corresponded to the spheroid passing the regions of the strongest electric field at the inner edges of the electrode set. A second simulation of the current was performed without the spheroid to obtain the baseline current. Peak-to-baseline values (ΔI) were then obtained by subtracting the current density peak value from the baseline value.

For obtaining baseline-normalized peak-to-baseline values (ΔI_{norm}), peak-to-baseline currents were divided by the corresponding baseline currents. Both, the ΔI and ΔI_{norm} values were plotted in Supplementary Figure 4.6C for a variety of different medium conductivities and two different particle sizes. It can be seen that the ΔI_{norm} values featured negligible dependence on the medium conductivity for conductivity variations between 0.5 S/m and 5 S/m compared to a relative change of approximately 20% upon increasing the particle size from 300 µm to 350 µm.

4.4.5 Monitoring drug response through EIS

The growth of HCT116 cancer spheroids has been assessed in presence of the anti-cancer drug 5-FU. The baseline-normalized values ΔI_{norm} (as shown in Figure 4.3B) were additionally start-point normalized to obtain the parameter $\Delta I_{norm,0}$ shown in Figure 4.4A. $\Delta I_{norm,0}$ – in contrast to ΔI_{norm} – is not sensitive to slight differences in the initial spheroid size. The start point normalization produces rising curves for spheroid growth – as opposed to the falling curves in Figure 4.3. $\Delta I_{norm,0}$ values for over 90 hours are displayed in Figure 4.4A and reflect the growth of the three spheroids under control conditions and upon DMSO and 0.4 µM 5-FU exposure. The spheroid treated with 4 µM 5-FU stops to grow after 40 h and starts to dissociate towards the end of the recording. The spheroid exposed to 40 µM 5-FU does not grow during the first 40 h and starts to dissociate thereafter. The trends observed by means of EIS – growth of the control group, DMSO- and 0.4 µM-5-FU-exposed spheroids, growth followed by dissociation for 4 µM 5-FU exposure and growth inhibition followed by dissociation for 40 µM 5-FU exposure – are supported by both, optical assessments of the spheroid cross-sections in Figure 4.4B and ATP assays in Figure 4.4C. In contrast to optical assessments and ATP assays, EIS offers the ability to monitor spheroid growth *in situ* in a continuous, non-invasive and automated fashion.

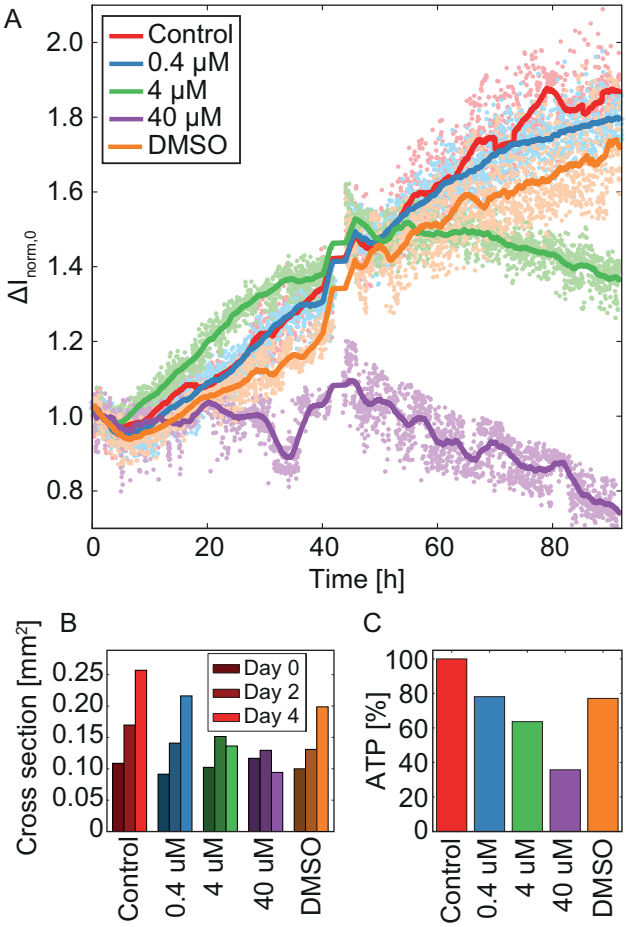

Figure 4.4. Impact of the drug 5-FU on HCT116 cancer spheroids. A: The start-point-normalized current $\Delta I_{norm,0}$ of cancer spheroids which were grown in 0.4 µM, 4 µM and 40 µM 5-FU, a control condition without drug and a second control condition with just DMSO in the same concentration as has been used for the 40 µM concentration of 5-FU. The medium was exchanged after 42 h. B: Cross-section assessed via microscopy every two days; C: Control-normalized ATP values at the end of the experiment. EIS data, optical size and ATP was measured on the same tissues respectively.

4.4.6 Monitoring of beating of cardiac microtissues

The analysis of beating human cardiac spheroids has been performed to demonstrate the ability of assessing different tissue types while using the same method and platform. The *in situ* assessment of cardiac beating is a particularly important feature of the platform here, as minor variations in environmental conditions – such as slight temperature changes upon transfer of the spheroids from an incubator to a microscope for optical assessment – can significantly influence the beating rate.[8] Monitoring the continuous beating of cardiac spheroids is a common readout not only to monitor cardiotoxicity effects, which usually entail a complete stop of cardiac beating, but also to detected different patterns of arrhythmia induced by pro-arrhythmic drugs.[20,21] Such analysis is not trivial to facilitate by optical means, as it requires *in situ* parallel and long-term microscopic video analysis.

Since the cardiac spheroids do not change in size, they are not studied while passing the electrodes. In order to extract their beating rates, they have to be transitionally immobilized in between the EIS electrodes. This was facilitated by moving the electrodes laterally to one end of the microchannel so that the retaining pillars are located between the electrodes (compare insets in Figure 4.5A to those of Figure 4.1D). Upon tilting the device up on the right side (t = 1 s in Figure 4.5A), the spheroid moves away from the retention pillars and out of the EIS sensing area. The inter-electrode impedance is reduced and the output current increased. Upon tilting the device down at the right side (t = 10 s in Figure 4.5A), the spheroid moves back into the sensing area, and the beating of the spheroid can be detected as ripples in the baseline current. A detailed view of the beating patterns, depicted in Figure 4.5B, shows that the contraction of the cardiac spheroid is significantly faster than the relaxation, which is in agreement with previous observations on such cardiac spheroids.[8] An 18 hour recording of the beating rate of a spheroid shown in Figure 4.5C revealed a regular beating of the spheroid,

initially at a rate around approx. 1.1 Hz, with standard deviations as low as 0.05 Hz and a slow change of the beating rate. These results demonstrate the sensitivity of the EIS spheroid analysis method.

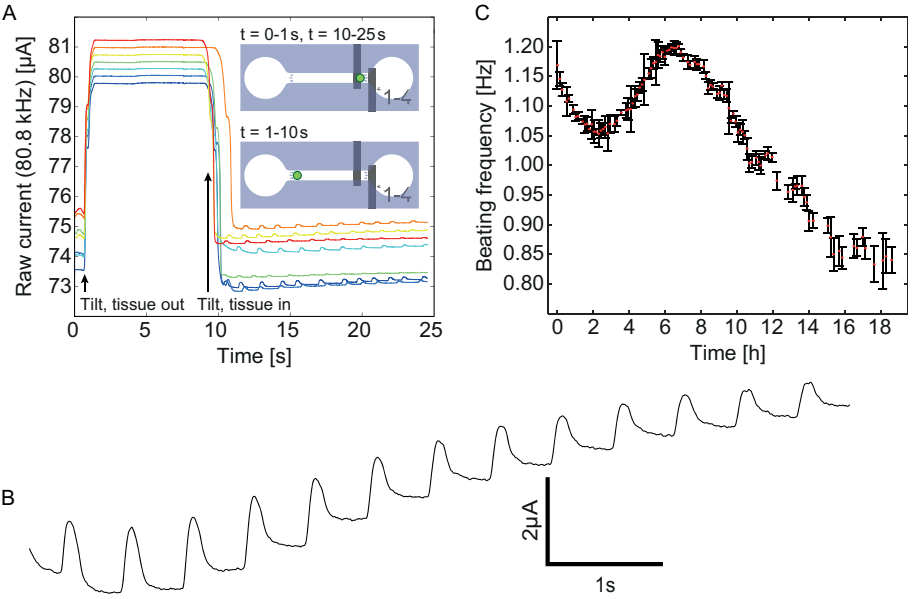

Figure 4.5. Measurements of cardiac spheroids. A: Tilting the chip with an off-center electrode arrangement allows for analysis of the cardiac beating; B: Detailed view of a typical beating pattern when the spheroid is located between the electrodes; C: 18 hour recording of the beating rate of a single spheroid, at each measurement point the mean beating rate and standard deviation is shown for a recording time span of 15 s (t = 10 - 25 s in A).

4.5 Conclusion

The presented platform provides an automated method to perform EIS measurements of multiple microtissue spheroids in parallel over several days. Compared to existing spheroid EIS platforms,[13–15] our system provides the following key advantages: (i) integration of EIS functions into a microfluidic spheroid device, which allows for medium perfusion and exchange, (ii) automated measurements and

culturing of multiple spheroids over several days without the need to relocate the spheroids, (iii) no need for surface-coating of the microfluidic device to avoid spheroid adhesion, as there is continuous tilting and spheroid movement, and (iv) continuous and independent multi-parameter measurements and analysis of different spheroids and medium properties in parallel and via the same set of electrodes.

The platform enabled the automated investigation of organ specific readout parameters at suitable temporal resolution: Examples included cardiac beating and growth of cancer with and without drug dosage. The presented platform includes a pump-free setup without complex fluidic or electrical interfacing, which entails a reduced risk of contamination. An up-scaled version of this prototype platform could host multiple microfluidic chip units, which would increase throughput via parallelization while still allowing for application- or organ-specific customization of the microfluidic units. The continuous EIS readout can be used to complement existing well-plate-based body-on-a-chip systems for *in situ* drug efficacy and cardiotoxicity assessments in the same microenvironment.[22–24] In summary, the AMEIS platform constitutes a scalable technology for parallelized EIS recordings of multiple spheroids.

4.6 Acknowledgements

This work was supported by the European Union FP7 grant under the project ‘Body on a chip’ ICT-FET-296257 and an individual Ambizione Grant 142440 of the Swiss National Science Foundation for Olivier Frey. We would like to thank InSphero AG, Schlieren, Switzerland, for providing the pancreatic microislets, cardiac spheroids and related media used in this study.

4.7 Bibliography

1 A. Abbott, *Nature*, 2003, **424**, 870–2.

2 J. M. Kelm and M. Fussenegger, *Trends Biotechnol.*, 2004, **22**, 195–202.

3 M. T. Santini, G. Rainaldi and P. L. Indo, *Int. J. Radiat. Biol.*, 1999, **75**, 787–799.

4 F. Pampaloni, E. G. Reynaud and E. H. K. Stelzer, *Nat. Rev. Mol. Cell Biol.*, 2007, **8**, 839–845.

5 A. Williamson, S. Singh, U. Fernekorn and A. Schober, *Lab Chip*, 2013, **13**, 3471.

6 D. Huh, Y. Torisawa, G. A. Hamilton, H. J. Kim and D. E. Ingber, *Lab Chip*, 2012, **12**, 2156.

7 Y. S. Zhang and A. Khademhosseini, *Nanomedicine*, 2015, **10**, 685–688.

8 P. Beauchamp, W. Moritz, J. M. Kelm, N. D. Ullrich, I. Agarkova, B. D. Anson, T. M. Suter and C. Zuppinger, *Tissue Eng. Part C Methods*, 2015, **21**, 852–861.

9 N. Haandbæk, O. With, S. C. Bürgel, F. Heer and A. Hierlemann, *Lab Chip*, 2014, 3313–3324.

10 S. Gawad, L. Schild and P. H. Renaud, *Lab Chip*, 2001, **1**, 76–82.

11 Z. Zhu, O. Frey, D. S. Ottoz, F. Rudolf and A. Hierlemann, *Lab Chip*, 2012, **12**, 906–15.

12 D. Holmes, D. Pettigrew, C. H. Reccius, J. D. Gwyer, C. van Berkel, J. Holloway, D. E. Davies and H. Morgan, *Lab Chip*, 2009, **9**, 2881–9.

13 H. Thielecke, A. Mack and A. Robitzki, *Biosens. Bioelectron.*, 2001, **16**, 261–269.

14 D. Kloss, R. Kurz, H.-G. Jahnke, M. Fischer, A. Rothermel, U. Anderegg, J. C. Simon and A. A. Robitzki, *Biosens. Bioelectron.*, 2008, **23**, 1473–80.

15 K. Luongo, A. Holton, A. Kaushik, P. Spence, B. Ng, R. Deschenes, S. Sundaram and S. Bhansali, *Biomicrofluidics*, 2013, **7**, 34108.

16 V. L. Sukhorukov, H. Mussauer and U. Zimmermann, *J. Membr. Biol.*, 1998, **163**, 235–45.

17 S. Gawad, K. Cheung, U. Seger, A. Bertsch and P. Renaud, *Lab Chip*, 2004, **4**, 241–51.

18 S. C. Bürgel, C. Escobedo, N. Haandbæk and A. Hierlemann, *Sensors Actuators B Chem.*, 2015, **210**, 82–90.

19 S. Poenick, H.-G. Jahnke, M. Eichler, S. Frost, H. Lilie and A. A. Robitzki, *Biosens. Bioelectron.*, 2014, **53**, 370–6.

20 H.-G. Jahnke, D. Steel, S. Fleischer, D. Seidel, R. Kurz, S. Vinz, K. Dahlenborg, P. Sartipy and A. A. Robitzki, *PLoS One*, 2013, **8**, e68971.

21 Y. A. Abassi, B. Xi, N. Li, W. Ouyang, A. Seiler, M. Watzele, R. Kettenhofen, H. Bohlen, A. Ehlich, E. Kolossov, X. Wang and X. Xu, *Br. J. Pharmacol.*, 2012, **165**, 1424–41.

22 J.-Y. Kim, D. A. Fluri, J. M. Kelm, A. Hierlemann and O. Frey, *J. Lab. Autom.*, 2015, **20**, 274–282.

23 J.-Y. Kim, D. A. Fluri, R. Marchan, K. Boonen, S. Mohanty, P. Singh, S. Hammad, B. Landuyt, J. G. Hengstler, J. M. Kelm, A. Hierlemann and O. Frey, *J. Biotechnol.*, 2015, **205**, 24–35.

24 S. Rismani Yazdi, A. Shadmani, S. C. Bürgel, P. M. Misun, A. Hierlemann and O. Frey, *Lab Chip*, 2015.

4.8 Supporting information

4.8.1 Chip fabrication

The device was fabricated in PDMS and bonded onto a glass slide that featured platinum electrodes as schematically shown in Supplementary Figure 4.1. Microfluidic structures were patterned in PDMS to retain the spheroids in the central channel and to guide them over the electrodes upon tilting of the device. The respective PDMS piece was casted from an SU-8 mold on a 4-inch silicon wafer and was bonded onto a glass slide, which has been patterned with the platinum microelectrodes. The SU-8 mold consisted of an 80 µm bottom layer, made of SU-8 50, and a 500 µm top layer, made of SU-8 100. The mold was silanized for 2 h with trichloro(1H,1H,2H,2H-perfluoro-octyl)silane (Sigma-Aldrich, USA) in a vacuum desiccator. 25 g of PDMS (Sylgard 184, Dow Corning Corp., USA), mixed with 10% cross-linking agent, were poured over the wafer yielding a device thickness of 5 mm. After 1 h of degassing in a vacuum chamber, the mold was baked for 2 h at 80 °C, pealed from the master and cut into individual chips. After punching 0.75-mm-diameter loading ports and 3-mm-diameter medium reservoirs, the PDMS pieces and glass slides were cleaned with acetone, isopropanol and water. The blow-dried pieces were treated in oxygen plasma before bonding. Irreversible bonding was ensured by a final baking step at 80 °C for 2 h. The microfluidic channel had a width of 700 µm, the retaining pillars on each side of the channel had a width and spacing of 100 µm (Figure 4.1D and E).

Platinum electrodes were patterned on the glass slides by a lift-off procedure. A four-inch glass wafer of 500 µm thickness was spin-coated with the positive-tone resist S1813 on top of an LOR3B resist (both from micro resist technology GmbH, Berlin, Germany) bottom layer. Efficient lift-off without side-wall metallization was ensured by a 1.5 µm undercut of the bottom LOR3B layer. A 200 nm Pt layer

was then deposited on top of a 20 nm W/Ti seed layer. The lift-off of the metal was carried out by using mr-rem-400 remover (micro resist technology GmbH, Berlin Germany). After metallization, the glass wafers were diced into individual glass slides of 32 mm x 80 mm. The electrodes extended across the entire channel and had a width and spacing of 500 µm (Figure 4.1D and E).

Some designs required isolation of the electrodes to prevent electrical shortcuts through the large media reservoirs on the chip. Therefore, an optional 500 nm Si_3N_4 deposition was performed after the metallization and before dicing. The areas, in which the Si_3N_4 was intended to remain, were masked using a lithographically structured S1813 layer. The nitride layer was then opened by plasma etching, and the S1813 mask layer was removed by mr-rem-400 wet etching.

The device was designed for an alignment precision of +/- 200 µm between the PDMS piece and the electrodes on the glass chips, which could be achieved by manual alignment under a stereomicroscope. Irreversible bonding was achieved by oxygen plasma treatment of both, the PDMS piece and the glass substrate followed by a baking step for 2 h at 80 °C on a hotplate.

4.8.2 EIS measurements

The impedance of the 15 separate spheroid chambers was evaluated by supplying AC voltages and analyzing the resulting currents. Six frequencies were equidistantly spaced on a logarithmic scale between 10 kHz and 1.86 MHz and simultaneously applied via the microelectrode set. The output voltages of 200 mV at each frequency were supplied by an HF2 impedance spectroscope (Zurich Instruments AG, Zurich, Switzerland). The resulting currents were transformed into voltages using a trans-impedance amplifier (TA) with a feedback gain of 100 Ω and then fed back to the impedance spectroscope for recording. The impedance

spectroscope featured maximally two signal outputs and inputs, but up to 15 separate chambers were to be measured. Thus, a multiplexing and switching architecture was required to supply the output of the impedance spectroscope as the input signal to each of the 15 chambers. Correspondingly, a de-multiplexing stage was used to receive the output signals from each of the 15 chambers and routing it to the input of the trans-impedance amplifier. This multiplexing/de-multiplexing and switching was facilitated via the previously described custom-made AMEIS switch board, which was directly interfaced to the microfluidic chip as shown in Figure 4.1B. In this way, the input and output channels of the impedance spectroscope could be connected to any of the 15 chambers in the microfluidic chip. The output current of the AMEIS switch board was fed back via the trans-impedance amplifier to the impedance spectroscope and recorded on a PC for later off-line analysis. Both, the impedance spectroscope and the trans-impedance amplifier were acquired from Zurich Instruments AG, Zurich, Switzerland.

4.8.3 Spheroid preparation

HCT116 cells were grown in RPMI 1640 medium (Chemie Brunschwig AG, Basel, Switzerland), supplemented with 10% fetal bovine serum (Sigma-Aldrich) and 100 IU/ml penicillin, 100 µg/ml streptomycin (P/S, Chemie Brunschwig AG, Basel, Switzerland) and 0.3 µg/ml puromycin. The cells were grown to 80% confluence in cell culture flasks, harvested by trypsinization and seeded into U-bottom 96-well plates. After 4 days, spheroids had formed and were ready to be transferred into the chip. For control experiments Langerhans microislets were used and kept in pancreatic microislet maintenance medium. Human cardiac microtissues were maintained in cardiac maintenance medium. The micro-islets and cardiac spheroids, as well as the respective media were provided by InSphero AG, Schlieren, Switzerland. Islets and cardiac spheroids were handled and loaded in the same way as the other cancer spheroids. All

spheroids were maintained in a humidified incubator at 37 °C and 5% CO_2. Some cancer spheroids were exposed to different concentrations of the anti-cancer drug Fluorouracil (5-FU) in the microfluidic chip. 5-FU was dissolved in dimethyl sulfoxide (DMSO) before diluting it to the target concentrations (0.4 µM, 4 µM and 40 µM) in culturing medium. Two different control groups were used: One group was grown in standard RPMI medium without 5-FU, the second control group contained RPMI, supplemented with DMSO at the concentration that has also been used for delivering the highest concentration of 5-FU.

4.8.4 Finite-element modelling

A finite-element model (FEM) was used to verify the independence of the ΔI_{norm} values from the medium conductivity (see Results section). The current through one electrode in the measurement chamber was calculated in the FEM by integrating the current density over the electrode surface using Comsol Multiphysics 4.3 (COMSOL AB, Sweden). Since a simplified cross-sectional 2D model was used, as shown in Supplementary Figure 4.6A, current values were given in units of [A/m]. In order to obtain the ΔI data, the position of the particle along the channel had to be obtained first. Therefore, the position of a 300-µm-diameter, non-conductive particle was swept axially through the channel, and the current density was determined for every increment to obtain the plot in Supplementary Figure 4.6B.

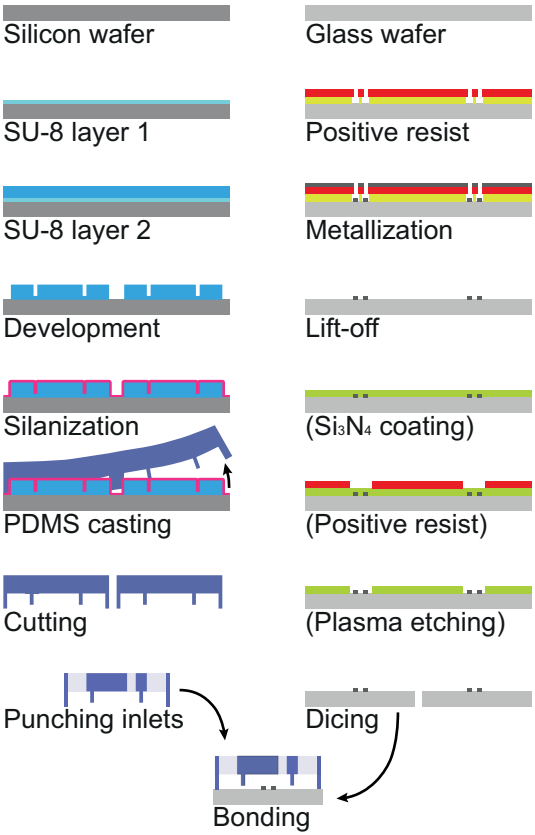

Supplementary Figure 4.1. Fabrication of the microfluidic chip. The left column shows the steps required for the SU 8 mold, which was then used to cast the PDMS device. The right column shows the electrode fabrication process on the glass substrate with the optional Si3N4 deposition and structuring step.

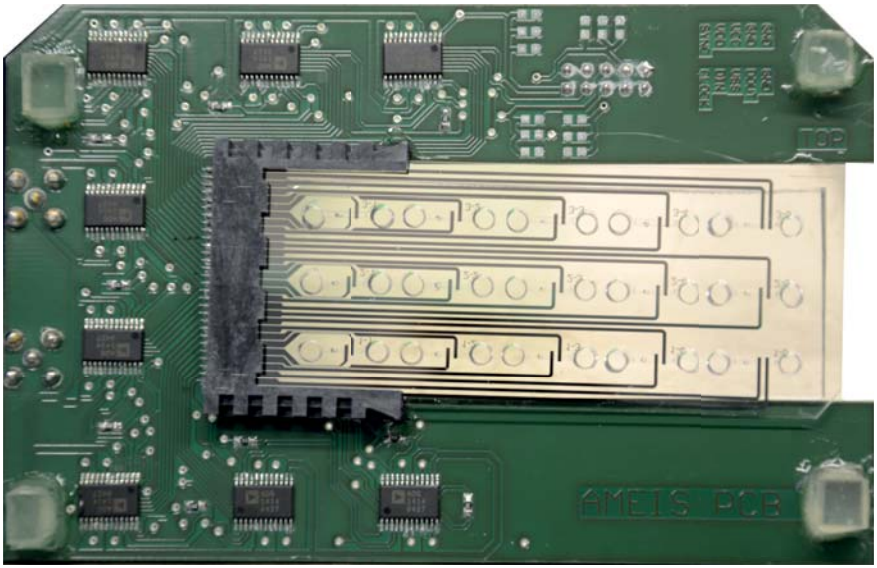

Supplementary Figure 4.2. The back side of the AMEIS switch board with a PDMS/glass chip inserted is showing the arrangements of switching ICs and the edge card connector for electrical interfacing with the microfluidic chip.

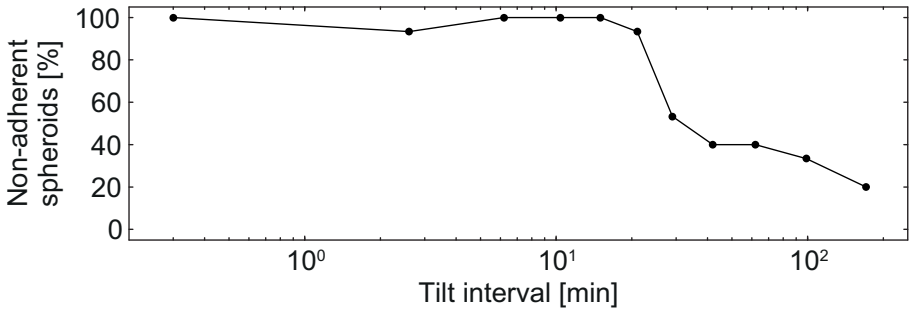

Supplementary Figure 4.3. Adhesion of microtissue spheroids with increasing tilting interval. The percentage of spheroids that was still moving and not adhering to the channel walls and bottom was decreasing, as the tilting interval exceeded 20 minutes.

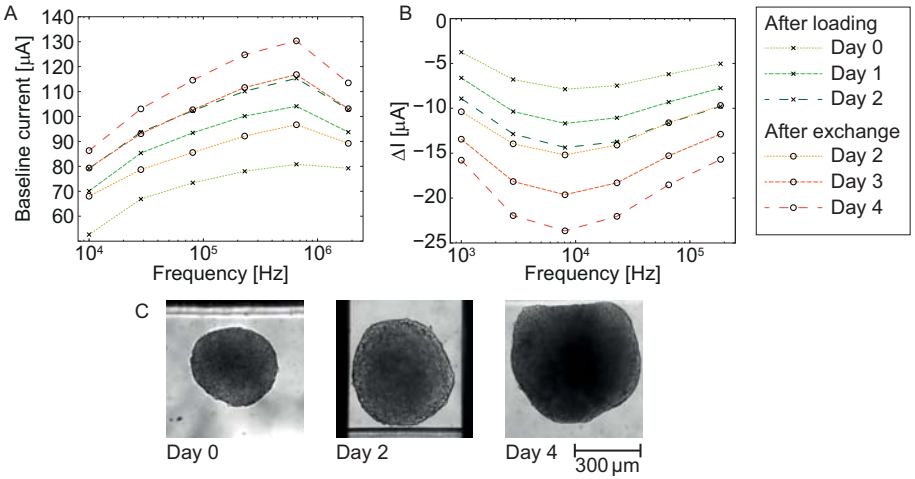

Supplementary Figure 4.4. Current spectra of a cancer spheroid at selected time points. A: baseline current spectra; B: ΔI peak-to-baseline spectra. Spectra are shown for selected time points between days 0 and 4; on day 2, the medium in all reservoirs was exchanged, so that data before and after medium exchange on the same day are shown. C: Optical monitoring of the growth of the very same spheroid measured by EIS in B.

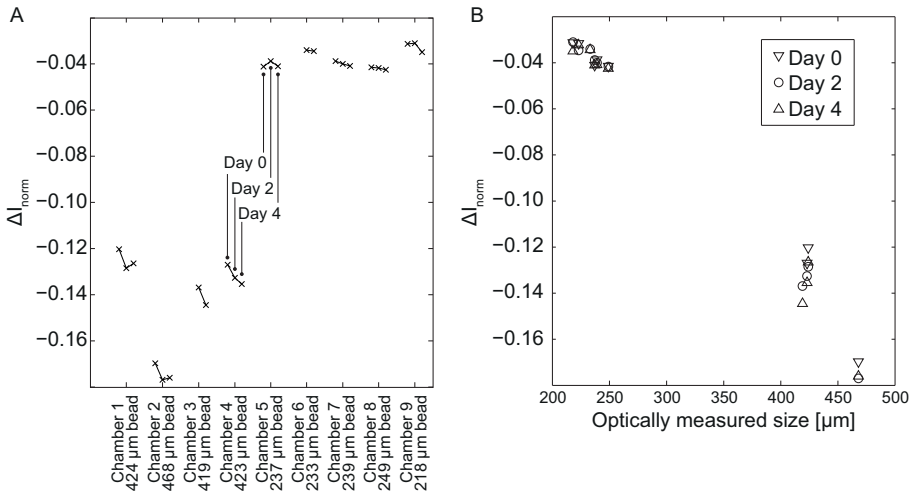

Supplementary Figure 4.5. Control experiment using 200-µm and 500-µm diameter beads. A: The ΔI_{norm} signal was evaluated at day 0, 2 and 4 for each size and shows that the signal was stable over multiple days with relative impedance variations below 10%. B: Different visualization of the same dataset shows that ΔI_{norm} scaled with the size of the beads.

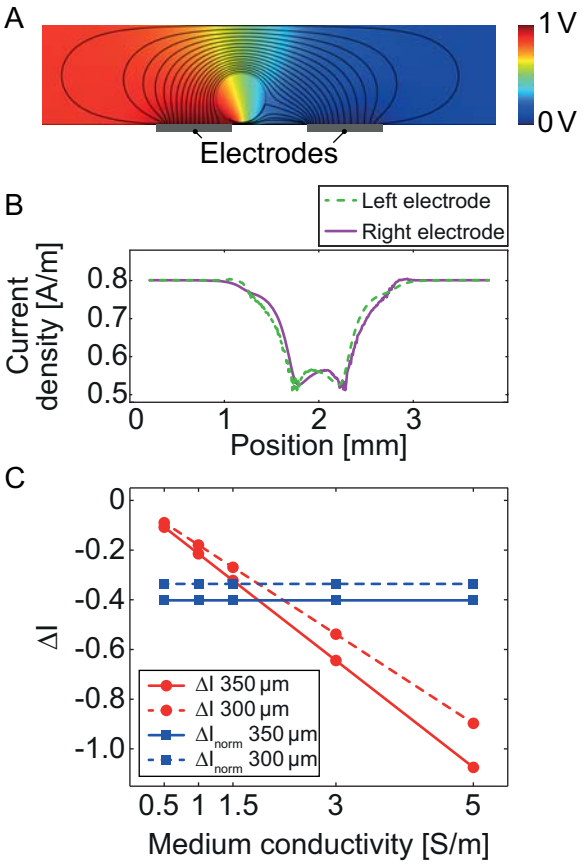

Supplementary Figure 4.6. Finite-element model of EIS measurements in the microchannel with electrodes. A: The electrical potential (rainbow surface) and electric field lines are shown for a non-conductive particle of 300 µm diameter. B: The shown particle position leads to a minimum in the plot of current density vs. position. Here, the center of a 300-µm-diameter non-conductive particle (cf. A) was swept axially through the channel. The resulting current densities for each position were integrated over the electrode surfaces and plotted versus the center coordinate of the particle. C: The peak-to-baseline (ΔI, in A/m) and baseline-normalized peak-to-baseline (ΔI_{norm}, no unit) have been simulated for different values of medium conductivity and two different spheroid sizes. The normalized magnitudes do not depend on the medium conductivity but primarily on the spheroid size.

5 CONCLUSION AND OUTLOOK

5.1 Conclusion

At the beginning of this thesis, only one microfluidic single-cell EIS device with facing electrodes had been published,[1] which was based on polyimide and which was later also used by another group.[2] Here, an SU-8 based device with facing electrodes tunable to various channel heights was fabricated. The device was then used for EIS studies of mammalian cells[3], mammalian cell electroporation (cf. chapter 2), and, in parallel, also for single yeast cells[4,5] and bacteria.[6] While the integration of electroporation and impedance analysis provides an interesting tool for basic insights into the poration process, the fabrication and integration is complex and requires costly and bulky equipment (at least high-frequency waveform generators). The electroporation process was significantly simplified by using a handheld corona discharge device, fow which not even microelectrodes are required. However, the strong electric fields and corona arcing prevents co-integration of this method with other sensitive measurement methods and device structures.

The focus then moved from single-cell studies with decades of experimental and theoretical foundations towards the more recent but rapidly expanding field of multicellular spheroids (cf. chapter 4). The fundamental insights and impedance-based characterization of

single cells obtained from experimental data and finite element models[5], as well as the derived analytical models (cf. chapter 2) will, however, form the basis for better analysis and understanding of spheroids. The size of the spheroids is roughly two orders of magnitude larger than that of single cells, which has implications for the microfabrication methods: Spheroids are not available in as large numbers as yeast or mammalian cells (at least 100'000 cells/ml). Therefore, in contrast to single cells, they are typically not studied in a flow-through fashion, butsingle spheroids are monitored over extended periods of time.[7] This approach requires more and larger chips without using complex, and costly glass-SU-8-glass sandwich fabrication yielding facing electrodes. Therefore, the spheroid chips rely on traditional soft-lithography PDMS structures, bonded to a glass slide that has been patterned with coplanar platinum microelectrodes for EIS readout. To date, no platform has been published, which is suitable for parallelized EIS monitoring of spheroids under medium perfusion.

The integration of a parallelized EIS readout into a microfluidic system is a powerful tool for analysis of multicellular spheroids. It addresses key limitations of existing systems,[7,8] which include (i) missing perfusion, and (ii) no possibilities of monitoring spheroid impedance over extended periods of time in an automated fashion. The time-resolved readout of cancer tissue growth by EIS, as presented in chapter 4, provides a simple yet translatable assay: quantification of volumetric cancer growth is also a typical readout quantity in clinical studies in humans and in animal *in vivo* experiments.

5.2 Outlook

The presented features of EIS for extraction of cancer spheroid growth and cardiac beating rate are two building blocks for future interconnected multi-organoid systems: One possible application is a cancer drug efficacy study in parallel to assessing cardiotoxicity.

This could be facilitated by integrating multiple EIS electrodes into one fluidically interconnected multi-organoid system.[9,10] Cancer and cardiac spheroids could be cultured in parallel while automatically assessing cancer growth and cardiac beating rate through EIS.

Direct translation of *in vitro* to *in vivo* results (e.g. IC_{50} values) by using the platform presented in Chapter 2 is so far not possible, since (i) PDMS is clearing especially small hydrophobic molecules rapidly from the solution and since (ii) the device does not feature a sufficiently large number of chambers for estimating IC_{50} values with a suitable number of repetitions (e.g., 5 concentrations plus 2 controls with 5 repetitions each). Currently ongoing efforts address this issue and are aimed at up-scaling the presented 15 chamber device to a 96-well-plate-compatible spheroid EIS device. The platform shown in Figure 5.1 features 4 chips with 18 spheroid chambers each. Spheroid chambers are vertically interconnected by microfluidic channels that allowing for culturing of different organoids in the same environment. This platform will allow for high-resolution extraction of IC_{50} and IC_{20} values with 10 different concentrations and 2 controls at 6 repetitions each. A plastic version of this platform in order to avoid typical PDMS compound absorption issues will be a versatile tool for EIS-based drug screening and toxicity assays. It will also allow for different types of microtissue spheroids to be cultured and analyzed by EIS. This platform will enable multiple toxicity assays, as well as compound-clearance or pro-drug studies through incorporation of liver spheroids.

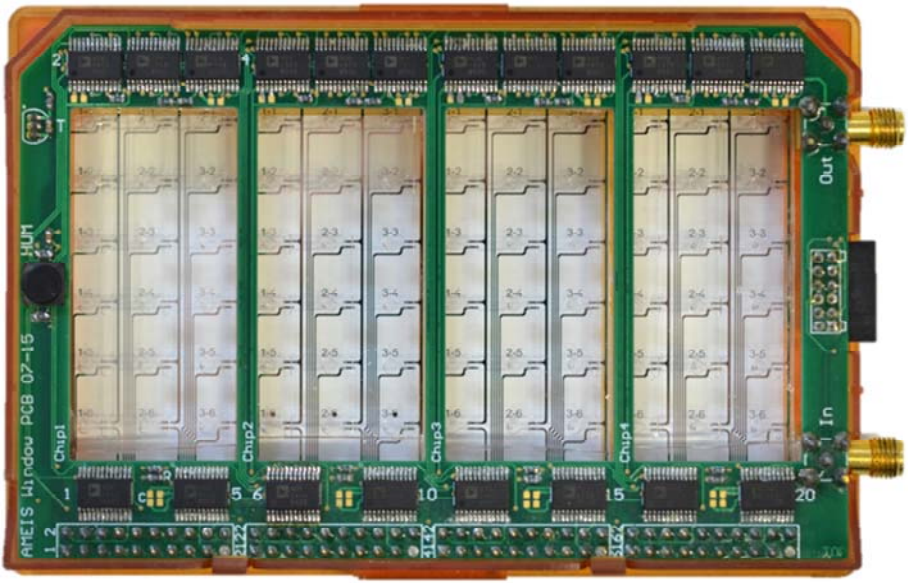

Figure 5.1. The up-scaled 96-well-plate-compatible version of the AMEIS platform. A 3D printed frame (orange) is used to hold the PCB (green) with the switches (black ICs), analog and digital connectors (right), as well as the humidity and temperature sensors (left). The frame also aligns the PCB with the four PDMS microfluidic chips, bonded to a glass slide with microstructured Pt electrodes.

The extraction of additional parameters from impedance spectra, besides changes in size, may be feasible in the future. Similar to single cells, the high-frequency electric field penetrates deeper into the spheroid and, thus, provides insights into changes in the internal composition. Specifically, it would be interesting to characterize the occurrence of a necrotic core inside larger spheroids by means of EIS. Currently, the parasitic capacitance of the PCB is limiting the frequency range to maximally 1 MHz and is thus limiting the sensitivity of the impedance readout at higher frequencies. Decreasing the parasitic capacitance is feasible by integrating the impedance readout more closely to the chip. This could be done by devising a custom multi-channel impedance ASIC, which could

either feature integrated multiplexing or multiple input/output units. A similar multi-channel CMOS impedance device for single cells is under development in our group.[11] Integrating a multi-channel readout will also increase the temporal resolution of the spheroid readout, since multiple spheroids can be measured in parallel. Currently, the need of sequential assessment of each chamber is limiting the temporal resolution. Especially in case of the cardiac spheroids, each spheroid has to be probed for typically 30 s to gain information about the regularity of the beating pattern, which entails considerable time to measure the entire platform comprising 72 spheroids.

Apart from employing a multi-channel EIS ASIC, the temporal resolution can be increased by a fast switching between chambers to obtain a quasi-parallel readout as schematically shown in Figure 5.2: When switching through all chambers (in the depicted example just 3) significantly faster than the time required for the spheroid moving over the electrodes (cancer spheroid) or beating (cardiac spheroid), then the spheroids can be recorded in parallel by down-sampling the raw signal of the corresponding chambers. The switch ICs used here (ADG1414, Analog Devices) operate at clock rates of up to 50 MHz. The clock rate of 50 MHz would need a different controller as the current Arduino but should be feasible with an FPGA. All 20 ICs require 8 bit per switch, thus the total bit-sequence of 160 bits could be written within 3.2 microseconds. When sampling all 72 chambers with a hold time of 100 microseconds per chamber to allow for a stable impedance signal to be recorded, an entire recording cycle of all 72 sites could be done within 7.43 milliseconds. This temporal resolution should be sufficient to resolve a spheroid rolling over the electrodes (~1s) or to resolve the cardiac beating rate of approximately 1 Hz. Assuming a recording time of 8 s per spheroid (as in chapter 4), the system could yield over 750’000 spheroid recording points per day, compared to 10’000 as presented in chapter 4. It is noteworthy that this is feasible without using a single-purpose ASIC and without

further scaling the platform beyond the current 96-well format (72 spheroids per plate). The short tissue holding times limit the impedance recording to frequencies above 100 kHz, which should be sufficient for monitoring both, cancer spheroid growth and cardiac beating.

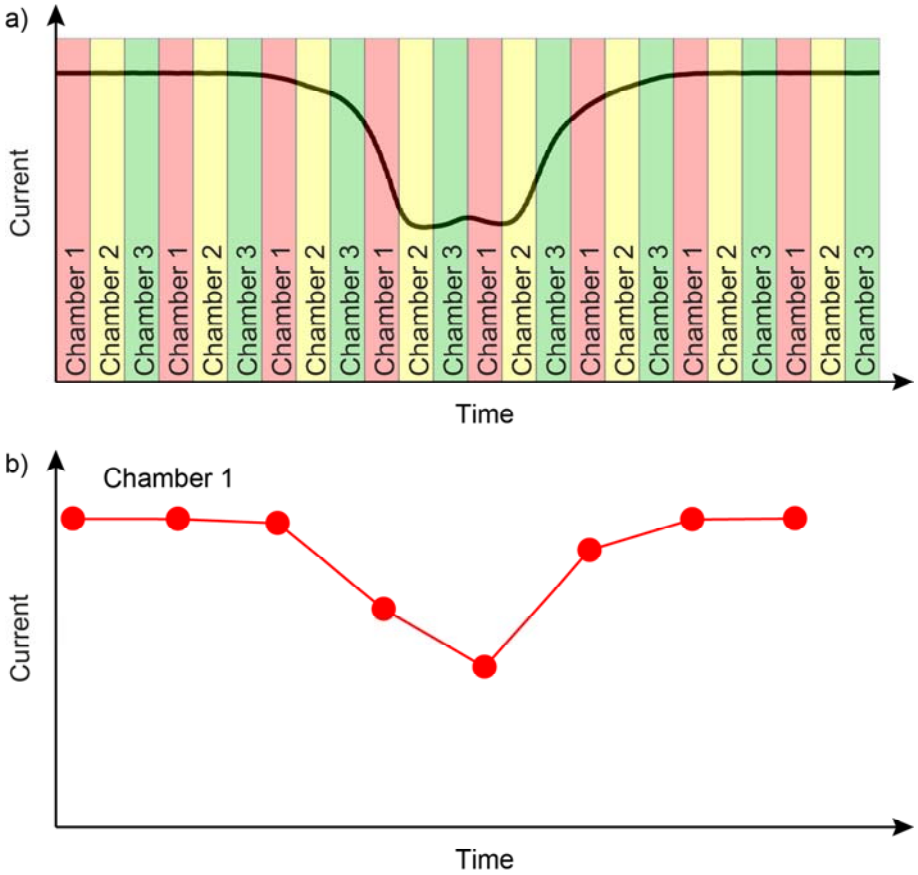

Figure 5.2. Schematic representation of quasi-parallel readout by fast switching of the readout current between 3 chambers (a) and the corresponding signal from chamber 1 (b).

Since the AMEIS hardware and software architecture is has not been specifically developed for spheroids, the platform can be used

as a general-purpose multi-site EIS tool. As such, it is currently being used for continuous EIS recordings of yeast growth.[12] Apart from spheroid studies, the platform can also be used for other organisms. One future target organism is the human parasite *Schistosoma mansoni*. In initial proof-of-concept experiments shown in Figure 5.3, EIS was identified a suitable tool to discriminate between live and dead (lysed) newly transformed *S. mansoni* larvae (NTS). Both, the magnitude and the phase spectra show significant differences between living and lysed NTS. The decreased differential magnitude spectrum of the dead NTS, shown in Figure 5.3b, can be interpreted – in analogy to the observations for electroporated mammalian cells in chapter 2 – as an inidication for a permeable membrane.

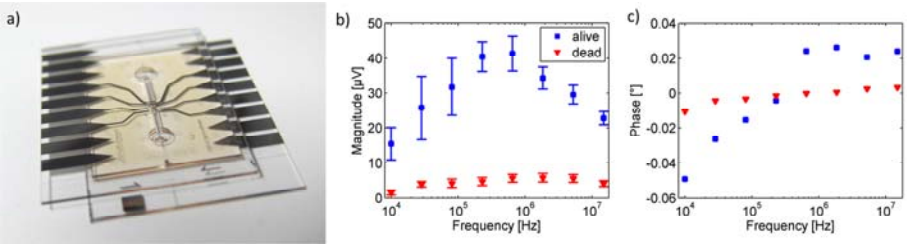

Figure 5.3. Proof-of-concept results of EIS for live/dead discrimination of S. mansoni larvae. The flow-through EIS device in (a) was used to record the impedance magnitude (b) and phase spectra (c). In both spectra, a significant difference was seen between viable and non-viable larvae.

An adaption of the parallelized spheroid EIS device to also accommodate NTS would allow for drug efficacy studies in the same fashion as for spheroids. The fluidic layer would, however, have to be adapted to retain the NTS within their chambers, since they are significantly smaller than then spheroids (20 x 20 x 100 µm^3). The combination of multi-organoid body-on-a-chip (BoC) devices with these parasites would enable toxicity and efficacy studies in an integrated infected-body-on-a-chip (iBoC) scenario as schematically shown in Figure 5.4. A co-culturing of NTS and liver spheroids will allow for the evaluation of (i) compound clearance (liver is

metabolizing the compound into an inactive form), (ii) existence of pro drugs (liver is metabolizing an inactive compound into an active form) and (iii) hepatotoxicity (compound is affecting the liver spheroid, potentially even leading to disintegration). The additional integration of a cardiac spheroid would allow for studying adverse effects, such as (i) carditoxicity (reduction of beating rate or entire stopping of the beating) and (ii) arrhythmia (compound induces irregular beating).

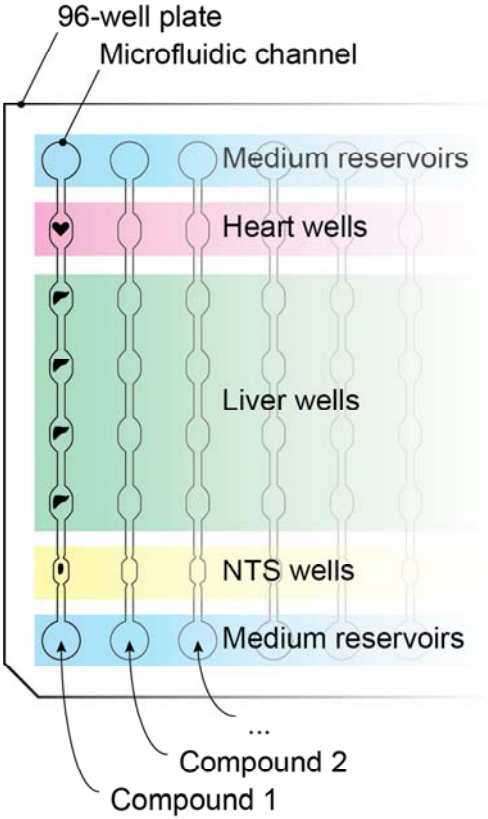

Figure 5.4. Schematic overview of a well-plate compatible iBoC with multiple organoids and NTS interconnected in the same microenvironment with EIS readout.

Spheroids are visible to the naked eye and can be loaded into the chambers by manual pipetting, although the process is labor-intensive and does not scale well. Loading NTS at a concentration of one NTS per well by manual pipetting is however challenging. NTS are too small to be seen by eye and – in contrast to spheroids – cannot be harvested from wells, containing the organisms. Therefore, an automated loading procedure is required, which will enable NTS studies at increased throughput by using 96-well plates and,at the same time, decrease the manual labor. Apart from simplifying and automating the experimental procedures, such a loading strategy could already include pre-screening stages, by means of, for example, EIS. Non-viable organisms or not sufficiently spherical tissue spheroids could be excluded from the batch before even loading them into the platform.

Summary of future improvements:

- Quasi-parallel readout of multiple chambers to increase temporal resolution,
- ASIC for low-parasitic-capacitance EIS readout close to the recording site,
- Analytical modeling of the spheroid impedance spectrum to elucidate the possibilities of extracting internal properties of the spheroid (such as necrosis),
- Automated loading procedure to facilitate EIS experiments with parasites and spheroids at higher throughput,
- Fluidically interconnected 96-well platform with EIS readout suitable for experiments with parasites and spheroids (iBoC) in parallel,
- Replacement of the prototype PDMS-on-glass chips with polystyrene devices to improve compound absorption issues and fabrication bottlenecks.

5.3 Bibliography

1 S. Gawad, L. Schild and P. H. Renaud, *Lab Chip*, 2001, **1**, 76–82.

2 D. Holmes, J. K. She, P. L. Roach and H. Morgan, *Lab Chip*, 2007, **7**, 1048–56.

3 N. Haandbæk, S. C. Bürgel, F. Heer and A. Hierlemann, *tm – Tech. Mess.*, 2013, **80**.

4 N. Haandbaek, K. Mathwig, R. Streichan, N. Goedecke, S. C. Bürgel, F. Heer and A. Hierlemann, *Procedia Eng.*, 2011, **25**, 1209–1212.

5 N. Haandbæk, S. C. Bürgel, F. Heer and A. Hierlemann, *Lab Chip*, 2014, **14**, 369–377.

6 N. Haandbæk, O. With, S. C. Bürgel, F. Heer and A. Hierlemann, *Lab Chip*, 2014, **14**, 3313.

7 D. Kloss, R. Kurz, H.-G. Jahnke, M. Fischer, A. Rothermel, U. Anderegg, J. C. Simon and A. A. Robitzki, *Biosens. Bioelectron.*, 2008, **23**, 1473–80.

8 H. Thielecke, A. Mack and A. Robitzki, *Biosens. Bioelectron.*, 2001, **16**, 261–269.

9 J.-Y. Kim, D. A. Fluri, J. M. Kelm, A. Hierlemann and O. Frey, *J. Lab. Autom.*, 2015, **20**, 274–282.

10 J.-Y. Kim, D. A. Fluri, R. Marchan, K. Boonen, S. Mohanty, P. Singh, S. Hammad, B. Landuyt, J. G. Hengstler, J. M. Kelm, A. Hierlemann and O. Frey, *J. Biotechnol.*, 2015, **205**, 24–35.

11 V. Viswam, J. Dragas, A. Shadmani, Y. Chen, J. Mueller, A. Stettler and A. Hierlemann, in *IEEE international Solid-State Circuits Conference (ISSCC)*, San Francisco, 2016.

12 K. Chawla, S. C. Bürgel, G. W. Schmidt, F. Rudolf, O. Frey and A. Hierlemann, *Procedia Eng.*, 2015, **120**, 154–157